Communauté d'Universités et d'Établissements Lille Nord de France

Université de Lille 1 Sciences et Technologies

Order Number: 42461

Université de Lille

Doctoral School **ED SMRE**

University Department **Laboratoire de Physique des Lasers, Atomes et Molécules (PhLAM)**

Thesis defended by **François Copie**

Defended on **26th October, 2017**

In order to become Doctor from Université de Lille

Academic Field **Physics**

Speciality **Optics and Lasers, Physical Chemistry, Atmosphere**

Thesis Title

Modulation instabilities in dispersion oscillating passive fiber-ring cavities

Thesis supervised by	Arnaud Mussot	Supervisor
	Matteo Conforti	Co-Monitor

Committee members

Referees	Stéphane Coen	University of Auckland
	Massimo Giudici	Université de Nice
Examiners	Julien Fatome	Université de Bourgogne
	François Leo	Université Libre de Bruxelles
	Stefano Trillo	Università degli studi di Ferrara
	Alexandre Kudlinski	Université de Lille
Supervisors	Arnaud Mussot	Université de Lille
	Matteo Conforti	Université de Lille

Université de Lille

Doctoral School **ED SMRE**

University Department **Laboratoire de Physique des Lasers, Atomes et Molécules (PhLAM)**

Thesis defended by **François Copie**

Defended on **26th October, 2017**

In order to become Doctor from Université de Lille

Academic Field **Physics**

Speciality **Optics and Lasers, Physical Chemistry, Atmosphere**

Thesis Title

Modulation instabilities in dispersion oscillating passive fiber-ring cavities

Thesis supervised by	Arnaud Mussot	Supervisor
	Matteo Conforti	Co-Monitor

Committee members

Referees	Stéphane Coen	University of Auckland
	Massimo Giudici	Université de Nice
Examiners	Julien Fatome	Université de Bourgogne
	François Leo	Université Libre de Bruxelles
	Stefano Trillo	Università degli studi di Ferrara
	Alexandre Kudlinski	Université de Lille
Supervisors	Arnaud Mussot	Université de Lille
	Matteo Conforti	Université de Lille

Université de Lille

École doctorale **ED SMRE**

Unité de recherche **Laboratoire de Physique des Lasers, Atomes et Molécules (PhLAM)**

Thèse présentée par **François Copie**

Soutenue le **26 octobre 2017**

En vue de l'obtention du grade de docteur de l'Université de Lille

Discipline **Physique**

Spécialité **Optique et Lasers, Physico-Chimie, Atmosphère**

Titre de la thèse

Instabilités modulationnelles dans les cavités fibrées passives à dispersion oscillante

Thèse dirigée par

	Arnaud Mussot	directeur
	Matteo Conforti	co-encadrant

Composition du jury

Rapporteurs	Stéphane Coen	University of Auckland
	Massimo Giudici	Université de Nice
Examinateurs	Julien Fatome	Université de Bourgogne
	François Leo	Université Libre de Bruxelles
	Stefano Trillo	Università degli studi di Ferrara
	Alexandre Kudlinski	Université de Lille
Directeurs de thèse	Arnaud Mussot	Université de Lille
	Matteo Conforti	Université de Lille

This thesis has been prepared at the following research units.

Laboratoire de Physique des Lasers, Atomes et Molécules (PhLAM)
Bât. P5
59655 Villeneuve d'Ascq Cedex
France

Institut de Recherche en Composants logiciels et matériels pour l'Information et la Communication Avancée (IRCICA)
50 Avenue du Halley
59650 Villeneuve d'Ascq
France

À mes parents,

"But still try, for who knows what is possible"

— Michael Faraday

"We can only see a short distance ahead, but we can see plenty there that needs to be done"

— Alan Turing

Modulation instabilities in dispersion oscillating passive fiber-ring cavities

Abstract

This thesis work deals with the parametric instability occurring in passive optical fiber-ring cavities, which is induced by a longitudinal modulation of the chromatic dispersion. In optical cavities, the modulation instability process is known to potentially destabilize the stationary state and turn it into a stable train of pulses. We describe in this work how a longitudinal variation of the dispersion inside the cavity enriches the dynamics of this type of device by entailing a regime of parametric instability. We detail the theoretical study of this new mechanism, which allows us to identify its spectral and temporal signatures, among which, the generation of multiple resonance peaks in the optical spectrum and the appearance of a period doubling dynamics in the time domain. We have realized such resonators in order to confirm experimentally our predictions. The model we have chosen simply consists in building a ring by splicing together uniform fibers characterized by different dispersions. In terms of results, we first observed the emergence of both modulational and parametric instabilities in the same system, before investigating their dynamics. The latter is accessible thanks to real-time spectral and temporal detection methods. We thus observed with remarkable precision the emergence of the instabilities, the period doubling associated to the parametric regime and the appearance of a record number of parametric resonances in our system.

Keywords: nonlinear optics; optical fibers; passive fiber cavities; modulation instability; parametric instability

Instabilités modulationnelles dans les cavités fibrées passives à dispersion oscillante

Résumé

Ces travaux de thèse portent sur l'instabilité paramétrique survenant dans les cavités optiques fibrées passives en anneau, induite par une modulation longitudinale de la dispersion chromatique. Dans les cavités optiques, le processus d'instabilité modulationnelle est connu pour être susceptible de déstabiliser l'état stationnaire et de le transformer en un train stable d'impulsions. Nous décrivons dans ce travail comment une variation longitudinale de la dispersion à l'intérieur de la cavité enrichit la dynamique de ce type de dispositif en engendrant un régime d'instabilité paramétrique. Nous détaillons l'étude théorique de ce nouveau mécanisme ce qui nous permet d'en identifier les signatures spectrales et temporelles, parmi lesquelles, la génération de multiples pics de résonances dans le spectre optique et l'apparition d'une dynamique de doublement de période dans le domaine temporel. Nous avons réalisé de tels résonateurs afin de confirmer expérimentalement nos prédictions. Le modèle que nous avons retenu consiste à réaliser un anneau en soudant entre elles des fibres uniformes présentant des dispersions différentes. En terme de résultats, nous avons tout d'abord observé pour la première fois l'apparition des instabilités modulationnelle et paramétrique dans un même système, pour ensuite s'intéresser à leur dynamique. Cette dernière est accessible grâce à des méthodes de détection en temps réel à la fois spectrale et temporelle. Nous avons ainsi pu observer avec une précision remarquable l'émergence des instabilités, le doublement de période associé au régime paramétrique ainsi que l'apparition d'un nombre record de résonances paramétriques dans notre système.

Mots clés : optique non-linéaire ; fibres optiques ; cavités fibrées passives ; instabilité modulationnelle ; instabilité paramétrique

Laboratoire de Physique des Lasers, Atomes et Molécules (PhLAM)
Bât. P5 – 59655 Villeneuve d'Ascq Cedex – France

Remerciements

Je tiens tout d'abord à remercier Georges Wlodarczak, ancien directeur, Marc Douay, directeur du laboratoire PhLAM de l'Université de Lille 1, ainsi que Majid Taki, directeur d'études doctorales, pour m'avoir permis d'effectuer cette thèse et pour avoir veillé à son bon déroulement. Je remercie aussi le département des actions internationnales du collège doctoral Lille Nord de France pour le soutien financier au titre de l'aide à la mobilité internationale des doctorants.

Je remercie les membres du jury qui ont accepté d'évaluer mon travail: M. Stéphane Coen, Professeur à l'université d'Auckland, M. Massimo Giudici, Professeur à l'université de Nice, M. François Leo, Docteur de l'université Libre de Bruxelles, M. Julien Fatome, Ingénieur de recherche au CNRS à l'université de Bourgogne, et M. Stefano Trillo, Professeur à l'université de Ferrare.

Mes plus chaleureux remerciements vont à mes encadrants, à commencer par Arnaud Mussot qui m'a accordé sa confiance il y a maintenant plus de 3 ans. Merci pour ton accompagnement quotidien et pour toute l'expérience que tu m'as transmis sur le monde de la recherche. Je n'oublirai pas les encouragements, la motivation et l'envie d'aller toujours plus loin que tu m'as insufflés. Merci à Matteo Conforti pour n'avoir jamais rechigné à m'expliquer un point de théorie obscure, même plusieurs fois consécutives, et pour ses nombreux conseils qui se sont toujours révélés pertinents. Merci enfin à Alexandre Kudlinski qui en l'espace de quelques mois m'a surclassé en course à pied, toutes distances confondues. Je tiens là ma motivation pour les années à venir! Votre complicité, tant professionnelle qu'humaine, ne s'est jamais démentie, même en pleine nuit, à 10 000 m d'altitude quelque part au-dessus de l'Asie, lorsqu'il s'agissait de se moquer de mon imprudence à parler français! Si j'ai décidé de poursuivre sur cette voie c'est en grande partie grâce à vous (ou à cause de vous, le temps le dira!).

Je tiens particulièrement à remercier Stefano Trillo pour l'intérêt qu'il a porté à mes travaux et pour avoir permis de les intégrer dans un contexte bien plus large que les "simples" cavités fibrées.

Je ne pourrais oublier de remercier Gilbert Martinelli pour m'avoir donné la possibilité d'enseigner mais aussi de l'intérêt pour mon travail qu'il n'a pas manqué de témoigner lors de ses visites "impromptues"!

Je remercie aussi Stéphane Coen, Stuart Murdoch, Miro Erkintalo, Frédérique Vanholsbeeck, et François Leo, pour leur formidable accueil à Auckland que je ne saurais oublier. Un grand merci à Stéphane et Frédérique pour le Tongariro, un rêve de gosse qui s'est réalisé!

Viens maintenant le moment de saluer tout mes collègues qui m'ont (sup)porté ces dernières années à commencer bien evidemment par les membres non permanents du *Zobicon Group*: ceux présents à sa fondation, Karim et Flavie, les membres du revival d'Alliage: Carlos le Catalan (mais pas trop), Tomy "Marestovsky", Florent "Quechua" Bessin, Corentin "l'épinard" Naveau, et leur manager Gangino. C'est avec plaisir que j'ai vu ce groupe s'agrandir et j'espère bien le voir rayonner dans les années qui viennent. Je pense aussi à ceux que je me permettrai d'appeller *les anciens*: le Baz, Benoit qui a toujours fait preuve de beaucoup d'intuidence, Guillaume "PCMCLCL" Le Cocq, le chercheur d'or Jean-Paul Yehouessi, la pleine de vie Carina, Pierre "No diggity" Gouriou, sans oublier Jean-Baptiste, mon camarade de galère: ça a été long, dur parfois ... mais à la fin on est quand même content!

Je remercie l'ensemble de l'équipe Photonique: Remi (pour m'avoir si souvent rappelé que je ne fais qu'étudier les faisceaux qui divergent!), Antoine, Stéphane, Karen, Géraud (pour ses remarques au quotidien...), Constance, Andy, Laurent, Esben, Olivier, Yves, Quentin, Remy, Odile, Damien, Laure, Julie, Monika, Mathilde, Aurélie, Patrick, Benjamin, Sébastien, Eric, Jean, Arsène, et ceux que j'oublie. Il est toujours plus motivant de travailler dans une ambiance agréable et détendue, et vous en êtes les principaux acteurs. Plus généralement, je remercie l'ensemble des personnes qui ont favorisé le bon déroulement de cette thèse et notamment Rédha Kassi et Pascal Szriftgiser pour les prêts de materiel qui ont été décisifs.

Je remercie mes plus fidèles copains de la fac pour leur accompagnement extra-scientifique tout à fait primordial, Maxime Thiégo ("On est quand même bien desservis!"), François Tric' ("Ah le gaaars!"), Marie ("Cette histoire, on s'en rappelera longtemps!"), Marine&Will (Belles aventures à vous deux!).

Je remercie ma famille et tout particulièrement mes parents pour leur infinie bienveillance.

Enfin, je me dois de mentionner les services en ligne *Linguee* et *Google Traduction* sans lesquels ce manuscrit n'aurait que bien peu de sens!

"And now for something completely different..."
— John Cleese in *The Monty Python's Flying Circus*

Table of Contents

Acronyms and abreviations

ASE amplified spontaneous emission

BPF band-pass filter

BS Brillouin scattering

CW continuous wave

DCF dispersion compensating fiber

DFB distributed feedback laser

DFT dispersive Fourier transformation

DOF dispersion oscillating fiber

DSF dispersion shifted fiber

EDFA erbium-doped fiber amplifier

EOM electro-optic modulator

FBG fiber Bragg grating

FOD fourth order dispersion

FR Faraday regime

FSR free spectral range

FWHM full width at half-maximum

FWM four-wave mixing

GNLSE generalized nonlinear Schrödinger equation

GVD group velocity dispersion

HOD higher order dispersion

LL Lugiato-Lefever

LLE Lugiato-Lefever equation

MI modulation instability

NLSE nonlinear Schrödinger equation

OI optical isolator

OPL optical path length

OSA optical spectrum analyser

OSC oscilloscope

PC polarization controller

PD photodetector

PG pattern generator

PID proportial-integral-derivative controller

PM polarization maintaining

POW power-meter

QPM quasi-phase-matching

SBS stimulated Brillouin scattering

SMF-28 single-mode fiber - 28

SPM self-phase modulation

SRS stimulated Raman scattering

STR fiber stretcher

SVEA slowly varying envelope approximation

TIR total internal reflection

TOD third order dispersion

TS-DFT time stretch - dispersive Fourier transformation

UTM ultrafast temporal magnifier

ZDW zero dispersion wavelength

Introduction

In less than half a century, lasers have become essential for an incredible amount of applications ranging from everyday life to industrial machining, surgery, metrology, as well as fundamental and applied physics. The extremely high intensity they can provide paved the way to the observation of new phenomena, which opened the field of nonlinear optics. Nonlinear phenomena arise when a light beam propagates inside a medium with an intensity such that its optical properties are modified. As a consequence, part of the incident light can be converted to other wavelengths. Lasers are not fundamentally required to observe nonlinear effects (as proved, for instance, by the observation of inelastic scattering of a tightly focussed sunlight beam in some liquids by Raman and Krishnan in 1927 [1]), yet their development has undeniably allowed huge and fast progresses in the field. Following the first demonstration of maser operation by Gordon *et al.* [2], Maiman made the first observation of laser radiation in 1960 [3], and most of its properties were demonstrated later that same year [4]. Since then, the optical nonlinear processes have been extensively investigated in various media such as quartz crystals like in the noteworthy observation of second harmonic generation by Franken *et al.* in 1961 [5].

In the 70's, the emergence of "low-loss" silica fibers appeared as a technological breakthrough as regards optical telecommunications but also as a new promising way to investigate nonlinear optics [6]. Indeed, in such waveguides, a high optical intensity can be maintained over a very long distance in a core of small radius, such that the effective length of nonlinear interaction between the light and the medium is strongly increased. Quite rapidly, nonlinear effects have attracted attention in these fibers and by 1978, the fundamental phenomena that constitute the basics of nonlinear optics such as stimulated Raman [7, 8] and Brillouin [9] scattering, optical Kerr effect [10], four-wave mixing [11, 12], and self-phase-modulation [13] were already observed. Another fundamental phenomenon has been predicted [14] and experimentally confirmed [15] in the 80's: The modulation instability. This latter is particularly noteworthy because it

appears in many different fields of physics such as hydrodynamics [16], plasmas [17], or Bose-Einstein condensates [18]. In the context of nonlinear optics, it occurs when an intense monochromatic pump wave propagates inside a fiber and manifests itself by the exponential growth of a weak perturbation of the optical field as a result of an interplay between the linear process of chromatic dispersion and the Kerr nonlinearity of silica. This results in the deepening of the modulation of the continuous wave field which eventually evolves towards a train of separate pulses [19]. In the spectral domain, the modulation instability process underpins the generation of sidebands symmetrically located around the pump wave. Extensive investigations of the modulation instability have been undertaken, partly motivated by potential applications such as fiber optical parametric amplifiers, based on the idea that a signal propagating along with the intense pump can be amplified through this nonlinear process over a large gain band [20, 21]. Modulation instability is also recognized as a key mechanism for the formation of the so-called "optical rogue waves" [22–24] and supercontinuum [25, 26] and is, even nowadays, the subject of intense theoretical and experimental studies.

In uniform nonlinear media, only a few parameters can be adjusted to improve the potentiality of nonlinear processes. Adding new degrees of freedom to those systems thus appears as a solution to enrich their dynamics. For instance, media with longitudinally varying parameters opened up new prospects in nonlinear optics. First, fibers with decreasing dispersion were studied [27] and found applications in terms of soliton compression [28] and supercontinuum broadening [29, 30]. Using the same degree of freedom, periodic variations of parameters have been considered and were expected to give rise to resonant phenomena. This is actually the case, for example, in the context of telecommunications where the periodic variation of the power along a transmission line, due to the recurrent amplification of the signal, has been found to be at the origin of new modulation instability sidebands at resonant frequencies which depend on the periodicity of the system [31]. Similar phenomena have been predicted in the case of a periodic variation of nonlinearity [32] and experimentally observed in a fiber with periodic birefringence [33]. This work revealed that several pairs of bands could be generated due to the periodicity of the system, each one fulfilling a quasi-phase matching relation. Nevertheless, only one pair of sidebands was successfully observed in these systems [33, 34]. More convincing observations were performed in systems with periodic management of the dispersion. This configuration has undoubtedly created the most interest both theoretically [35–40] and experimentally [41–51] because of the fact that large relative variations of the dispersion are more easily accessible than for other parameters. Additionally, the system can even experience negative and/or positive dispersion depending on the pump wavelength, which drastically impacts its behaviour. The experimental result that best highlights the impact of periodic dispersion manage-

ment in the single-pass configuration was obtained by Droques *et al.* in 2012 using a 120−m-long photonic crystal fiber presenting a sinusoidal variation of dispersion over a period of 10 m [41]. This kind of fiber is commonly referred to as *"dispersion oscillating fiber"* or DOF [52]. In this work, the authors observed the record number of 10 pairs of spectral sidebands solely induced by the periodic variation of dispersion.

On a different note, the efficiency of light-matter interaction underlying nonlinear effects can be greatly increased by allowing light to perform multiple passes in the same fiber. This is the fundamental concept of nonlinear optical cavities. The coherent interaction between light entering the cavity and light already circulating inside does much more than just enhancing the nonlinear effects. Indeed, the feedback mechanism induces a complex dynamics featuring optical bistability, self-oscillations, and chaotic behaviours [53–61]. In the late 80's, modulation instability oscillations were observed for the first time in a fiber-ring cavity, but without any control over the interferometric nature of the device [62]. The system was thus not operated under stable conditions. In the early 90's, theoretical studies of Haelterman *et al.* predicted that when operating under stable conditions, the modulation instability process was likely to occur in fiber-ring cavities but strongly modified owing to the boundary conditions imposed by the cavity configuration [63–66]. In their work, the authors predicted, among other things, the quite noteworthy formation of stable temporally modulated waveforms regardless of the regime of dispersion. Corresponding experimental studies have been reported, thanks to the essential implementation of a phase locking apparatus, and the occurrence of cavity induced modulation instability has been confirmed experimentally by Coen *et al.* [67]. Remarkable features of the intracavity modulation instability have been evidenced afterwards such as the induced bistable switching [68, 69] or the stable generation of pulse trains [70]. In the recent years, passive fiber-ring cavities have created a renewed interest for being the first device in which temporal cavity solitons were successfully excited (i.e. pulses circulating indefinitely inside the cavity without changing their shape) [71]. Since then, the study of temporal cavity solitons has attracted considerable attention for their potential use as bits in all-optical buffers, and especially in microresonators [72–74] because of the fact that, in these devices, they underpin the formation of broad Kerr frequency combs with promising capabilities for various application fields such as frequency metrology, precision spectroscopy or sensing [75–77]. Even if fiber cavities are less likely to find direct applications, their ease of implementation and their macroscopic scale make them ideal test beds for fundamental studies of the dynamics of nonlinear optical cavities. Indeed, the typical microsecond scale of a fiber cavity allows in depth investigations of the dynamics of the system round-trip after round-trip, thanks to the use of ultrafast acquisition apparatus (the round-trip time of a 100−m-long cavity is roughly 0.5 µs). Such studies are not

conceivable in microresonators because of their much shorter round-trip time which is not compatible with current electronic devices [76].

The present work finds its origin in a theoretical study performed by Conforti *et al.* prior to the beginning of this thesis in which a new type of fiber device was introduced, mixing the concepts of dispersion oscillating fiber and passive cavity [78]. We call it "*longitudinally modulated fiber cavity*". More specifically, the authors investigated how the dispersion management inside the resonator impacts the modulation instability process and predicted the emergence of a new regime related to parametric resonances. The main goal of this thesis was to implement such longitudinally modulated cavities to study their peculiar features. We used the previously mentioned theoretical study as a basis to design and realize our experimental investigations. Most notably, we observed for the first time the different modulation instabilities arising in our system and characterized their real-time dynamics both in the spectral and temporal domains. Beyond the fundamental nature of this work, the results presented are relevant in several applicative domains and may impact future studies on dispersion managed fiber lasers, widely tunable parametric oscillators, and frequency comb generation in microresonators to name a few.

The manuscript is organised as follows.

In **Chapter 1** we describe the concept of optical fiber-ring cavity and we introduce the different fundamental phenomena that rule the propagation of light inside such system. The mathematical models reproducing the behaviour of ring cavities are derived and compared. **Chapter 2** provides a reminder of the theoretical analysis of the modulation instability process as it occurs in dispersive, nonlinear and dissipative systems such as fiber cavities with Kerr nonlinearity. We then extend this analysis to longitudinally modulated fiber cavities which introduce the notion of parametric modulation instability. The different features of this regime are highlighted in the spectral and temporal domains. **Chapter 3** is devoted to the experimental implementation of such resonators with a strong emphasis on the techniques used to operate them in a stable fashion. The main benefits of studying fiber-cavities compared to microresonators are discussed in the preamble. We also describe the different recording methods that we employed. In the rest of the dissertation, we report on the results of our experimental investigations of longitudinally modulated fiber-ring cavities. In **Chapter 4**, the interplay between the modulation instability and the parametric instability is studied in details, confirming among other things their occurrence in the same physical system for the first time [79]. We also reveal the round-trip-to-round-trip dynamics of our system both spectrally and temporally [80]. Then, we study in **Chapter 5** the impact of a weak dispersion on the parametric instability and found that, under such conditions, this latter is strikingly

exacerbated. We provide corresponding experimental evidences with a record number of parametric resonances observed in the optical spectrum [81]. Finally, we describe in the **Appendix A** our experimental investigation regarding the impact of a cavity synchronization mismatch on the modulation instability process. We show that it induces a linear drift of the modulation in the temporal domain and, less intuitively, a shift of the instability sidebands in the optical spectrum.

The reader's attention is drawn to the fact that all along this dissertation we refer to "modulation instability" and "parametric modulation instability" as two different processes, but that the "parametric modulation instability" is actually also a "modulation instability" but of different physical origin. Thus, when we refer to the "modulation instability" (or "Turing instability"), we mean the one induced by the boundary conditions of the cavity, whereas "parametric modulation instability" (or "Faraday instability") refers to the one induced by the longitudinal modulation of the dispersion inside the cavity.

"First master the fundamentals"

— Larry Bird

CHAPTER 1

Basics of the passive cavity configuration

The purpose of this introductory chapter is twofold. In the first section, we list the main phenomena involved in the propagation of light in optical fibers as well as the assumptions used throughout this dissertation. We end up with the propagation equation that includes these phenomena (the nonlinear Schrödinger equation). In the second section, the mathematical description of the cavity configuration is introduced: an additional equation describing the recirculation of light inside the resonator allows us to determine its steady state behaviour, including the influence of losses and nonlinearity. To go further, we perform additional hypothesis to derive a simpler model of the cavity (the Lugiato-Lefever equation), which allows more analytical insight. This model will be the cornerstone of all the theoretical work presented in this dissertation. We use it to determine the conditions of stable continuous operation of such ring cavities. We

conclude by a brief discussion about bistability, a fundamental feature of nonlinear optical cavities.

1.1 Propagation of light in optical fibers

Optical fibers are waveguides usually made of fused silica mixed with some dopants whose role is to modify the refractive index of the medium. Nowadays, a tremendous amount of fibers are available commercially, each one designed for a specific application ranging from optical telecommunications to biosensing or spectroscopy, to name a few. In the course of this dissertation, we will mostly consider fibers currently used in the telecommunication domain. Such fibers consist of a high index core surrounded by a lower index cladding embedded in a polymer buffer, which provides mechanical strength. This kind of fiber observes a circular symmetry with respect to the longitudinal axis passing through the center of the core. The optical field is confined inside the core as a consequence of the total internal reflection (TIR) principle [82]. All the parameters introduced in the following subsections arise as a combination of the medium's mechanical properties and the fiber's geometry. At this point it is important to note that in all the work presented in this dissertation, we exclusively consider *single mode* optical fibers. This latter property means that the optical field can propagate inside the fiber according to a single transverse distribution of intensity, called *mode*. In our case, a non-diverging gaussian beam gives a good approximation of this distribution. Mathematically speaking, the single mode propagation hypothesis drastically simplifies the analytical treatment of pulse propagation in waveguides. Indeed, the system can be reduced to a 1-D model, the only variable being the longitudinal coordinate z that gives the propagation distance.

1.1.1 Losses

During propagation in the fiber, an optical signal undergoes losses mainly resulting from a combination of the absorption of silica and Rayleigh scattering. These losses depend on the light wavelength and, for standard silica fibers, are minimum around 1.55 µm. This is, by the way, the spectral region used in optical telecommunications. The linear attenuation α_f (in m^{-1}) quantifies these losses by linking the power at the input of a fiber P_0, its length L and the transmitted power P_T through the relation $P_T = P_0 \exp(-\alpha_f L)$. To date, the lowest losses recorded in a single mode silica fiber used around 1.55 µm correspond to $\alpha_f \approx 3.3 \times 10^{-5}\,\mathrm{m}^{-1}$ (0.1419 dB/km) [83].

1.1.2 Chromatic dispersion

The response of a dielectric medium, such as silica, to the interaction between an electromagnetic wave and the electronic cloud usually depends on the angular frequency ω. This implies a frequency dependence of the refractive index of the medium $n(\omega)$ which is referred to as *chromatic dispersion*. This latter is an important characteristic of an optical fiber. Indeed, it implies that different spectral components of an optical pulse do not travel at the same velocity, resulting in a distortion of the signal during its propagation. To allow a simple description of the effect of chromatic dispersion, we introduce here a major assumption of this work, which is the slowly varying envelope approximation (SVEA). This assumption amounts to consider that the spectral width $\Delta\omega$ of the optical signal is very small compared to the carrier frequency ω_0. This is always verified in the work presented here, where the spectral width of the signals does not exceed 20 THz with a carrier frequency $\omega_0 \approx 193$ THz. In this context, it is legitimate and customary to account for the effects of chromatic dispersion by expanding the propagation constant $\beta(\omega)$ in a Taylor series around the carrier frequency ω_0 as follows:

$$\beta(\omega) = n(\omega)\frac{\omega}{c} = \beta_0 + \beta_1(\omega-\omega_0) + \frac{\beta_2}{2}(\omega-\omega_0)^2 + \frac{\beta_3}{6}(\omega-\omega_0)^3 + \dots \tag{1.1}$$

where

$$\beta_m = \left(\frac{d^m\beta}{d\omega^m}\right)_{\omega=\omega_0} \qquad (m = 0,1,2,3,\dots) \tag{1.2}$$

In Eq. (1.1), β_1 is the inverse of the group velocity of light in the fiber (velocity of the pulse envelope), β_2 is the *group velocity dispersion* (abbreviated GVD) which is responsible for pulse broadening. In most silica fibers it vanishes for a particular wavelength called *zero dispersion wavelength* (abbreviated ZDW) and labelled λ_D. In standard single mode fibers (SMF-28) $\lambda_D \approx 1.3\,\mu$m, but the dispersion can be tailored during the fabrication such that fibers with ZDWs ranging from 1.3 to 1.7 µm are widely available and usually referred to as dispersion shifted fiber (DSFs). The spectral domain where $\beta_2 > 0$ is usually called the *normal dispersion regime* as opposed to the *anomalous dispersion regime* which is characterized by $\beta_2 < 0$. Higher order dispersion terms (β_3, β_4, ...) may also be significant especially when considering pulse propagation in the vicinity of the ZDW and/or when the pulse duration is very short (the optical spectrum is broad).

1.1.3 The Kerr nonlinearity

The interaction of an electromagnetic field with a dielectric medium generates a polarization. This polarization is related to the electromagnetic field through the susceptibility

tensor χ which is specific of the medium. At first order, When the field becomes sufficiently intense, a nonlinear polarisation appears that has to be taken into account. In most cases involving standard optical fibers, the second-order susceptibility $\chi^{(2)}$ vanishes due to the centro-symetric nature of silica and thus the first nonlinear effects observed are of order 3. The polarisation then reads:

$$\mathbf{P} = \mathbf{P}_L + \mathbf{P}_{NL} = \epsilon_0 \left(\chi^{(1)} \cdot \mathbf{E} + \chi^{(3)} \vdots \mathbf{EEE} \right) \tag{1.3}$$

where ϵ_0 is the vacuum permittivity, $\chi^{(j)}$ is the susceptibility of order j and E is the electromagnetic field. Note that the chromatic dispersion introduced earlier is linked to the real part of the first order susceptibility through $n(\omega) = \sqrt{1 + \mathfrak{Re}(\chi^{(1)}(\omega))}$. For optical fibers, it is reasonable to stop this development to $\chi^{(3)}$ since higher order terms are generally negligible. One of the nonlinear effects originating from the third order nonlinearity is the optical Kerr effect. It results in the intensity dependence of the refractive index of the medium. We will consider a pure instantaneous Kerr nonlinearity such that the refractive index takes the form $n = n_0 + n_2 I$ where n_2 is the nonlinear refractive index which is proportional to the real part of $\chi^{(3)}$, and I is the optical intensity. For standard silica fibers, n_2 takes a value of $\approx 2.6\,\mathrm{m}^2/\mathrm{W}$ [84]. The nonlinearity of a fiber is generally defined by the nonlinear coefficient $\gamma = n_2\omega_0/cA_{eff}$ where A_{eff} is the effective area of the transverse mode (A more confined field leads to a greater nonlinear coefficient). In standard optical fibers, γ ranges from 1 to 10 /W/km, but it can be more than two orders of magnitude higher in micro-structured or non-silica fibers [84]. The optical Kerr effect is responsible for several phenomena including the self-phase modulation (SPM), which strongly modifies the behaviour of an optical cavity as we will see later in this chapter.

1.1.4 The nonlinear Schrödinger equation

Under these assumptions it can be demonstrated that the evolution of the field is described by the nonlinear Schrödinger equation (NLSE) [84]:

$$\frac{\partial E(z,\tau)}{\partial z} = -i\frac{\beta_2}{2}\frac{\partial^2 E(z,\tau)}{\partial \tau^2} + i\gamma |E(z,\tau)|^2 E(z,\tau) \tag{1.4}$$

where τ is the time defined in the reference frame travelling at the group velocity of the carrier frequency (ω_0). This way, E describes the profile of the field envelope at the distance z in this "*fast time*" reference frame. The right hand side of the equation features two terms related to the chromatic dispersion and Kerr nonlinearity respectively. It should be pointed out that the contribution of the dispersion is reduced here to a single term proportional to the GVD. When a pulse propagates in the vicinity of a ZDW

($\beta_2 \approx 0$) one has to take into account higher order dispersion terms from the Taylor series expansion of $\beta(\omega)$ (β_3, β_4, ...). In practice, the dispersion never vanishes completely and higher order dispersion terms might impact the propagation of optical pulses. To account for the linear losses, we can add the term $-\frac{\alpha_f}{2}E(z,\tau)$ to the right hand side of the equation:

$$\boxed{\frac{\partial E(z,\tau)}{\partial z} = -\frac{\alpha_f}{2}E(z,\tau) - i\frac{\beta_2}{2}\frac{\partial^2 E(z,\tau)}{\partial \tau^2} + i\gamma|E(z,\tau)|^2 E(z,\tau)} \tag{1.5}$$

This equation allows to accurately simulate the propagation of light in optical fibers in various situations. However it does not take into account higher-order effects. Note that an extended version of Eq. (1.5) has been developed under the name of generalized nonlinear Schrödinger equation (GNLSE) and includes the effects of higher order dispersion terms and co-propagating nonlinear phenomena such as stimulated Raman scattering (SRS) or self steepening [85–87]. In our case, we don't need to account for these higher order nonlinear effects.

1.2 Passive optical resonators

The previous equation describes the evolution of a pulse envelope as it propagates along an optical fiber. We will refer to this case as the *single-pass configuration*. The topic of this work is to study the *multi-pass configuration* or *cavity configuration* which is schematically described in Fig. 1.1. A passive fiber-ring cavity is basically composed of a fiber coupler characterized by reflection and transmission coefficients, ρ and θ respectively, defined such that $\rho^2 + \theta^2 = 1$. Light launched through the input port on the left is partially directed to the output port on the right and inside the resonator. The resonator itself is composed of a ring of optical fiber of length L with both ends connected to the coupler. A fraction of the intracavity field exits the cavity through the coupler whereas the intracavity field is continuously fed by the input field. The intracavity field thus consists in a coherent superposition of the input and recirculating fields. This interaction is the fundamental mechanism of the *multi-pass configuration*.

Inside the resonator, light propagates along the ring and undergoes the combined effects of losses, dispersion and nonlinearity. Mathematically, this intracavity propagation is ruled by the nonlinear Schrödinger equation (1.5). The impact of the coupler is described by the additional *cavity boundary condition equation*:

$$\boxed{E^{(m+1)}(0,\tau) = \theta E_{in} + \rho E^{(m)}(L,\tau)\, e^{i\Phi_0}} \tag{1.6}$$

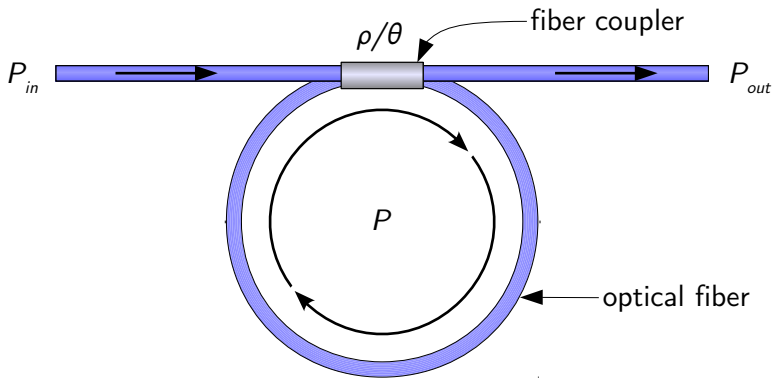

Figure 1.1 – Schematic representation of a passive fiber-ring cavity.

which relates the intracavity field at the beginning of round-trip $(m+1)$ to the one at the end of round-trip (m).

The first term on the right hand side of Eq. (1.6) accounts for the driving field of the cavity, E_{in} being the field at the input port of the coupler. This field can, in principle, take any form but in practice it is either a continuous wave (cw) or a train of pulses. In this latter case (which is the configuration used in all the experiments described in this work) the duration between two consecutive pulses has to be set to a multiple or sub-multiple of the round-trip time of the cavity ($t_R = \beta_1 L$) so that the coherent interaction between the fields actually occurs. In practice, a perfect synchronisation is tricky to achieve and a mismatch can alter the behaviour of the resonator [88] (see also Appendix. A).

The last term of Eq. (1.6) reflects both the dissipative and interferometric nature of the system. Indeed, the reflection coefficient ρ describes how the intracavity field is partially coupled out of the cavity at each round-trip. Also fundamental is the linear phase accumulated over one round-trip $\Phi_0 = \Phi_L$ which determines how the input and intracavity fields interfere. Note that this phase term is not considered in the NLSE (1.5). We will see later in this chapter that it can be accounted for through an appropriate substitution. This term simply reads $\Phi_0 = \beta_0 L$ with $\beta_0 = \omega_0 n/c = 2\pi n/\lambda_0$. One should thus notice that it can be tuned by changing either the refractive index of the fiber n, the cavity length L or the pump wavelength λ_0. We will see in the next developments that this term is fundamental in the operation of a cavity since it governs the transmission of the system. The phase accumulated by the optical signal inside the resonator is also crucial for the description of nonlinear effects such as the intracavity modulation instability which is addressed in details in the next chapter.

The full dynamics of such a passive fiber-ring cavity can be described by the system

composed of the NLSE including linear losses (1.5) and the *cavity boundary condition equation* (1.6) repeated here for convenience:

$$\begin{cases} \dfrac{\partial E(z,\tau)}{\partial z} = -\dfrac{\alpha_f}{2}E(z,\tau) - i\dfrac{\beta_2}{2}\dfrac{\partial^2 E(z,\tau)}{\partial \tau^2} + i\gamma|E(z,\tau)|^2 E(z,\tau) \\ E^{(m+1)}(0,\tau) = \theta E_{in} + \rho E^{(m)}(L,\tau)\, \mathrm{e}^{i\Phi_0} \end{cases} \tag{1.7}$$

This infinite-dimensional system is often referred to as the Ikeda map, developed in the general context of optical ring cavities [53]. Note that this model is the most general one that describes the cavity, i.e. the one obtained with the least number of assumptions. Note that a simplified equation, called the Lugiato Lefever equation (LLE), derived by lumping together the equations of this system is presented in Sec. 1.2.3.

1.2.1 The linear cavity resonances

The first step in describing the operation of a ring cavity is to determine the steady state of the system. The expression of the stationary field inside the cavity is easily obtained by noting that it corresponds to the field E that evolves neither during a round-trip, nor over consecutive ones. Mathematically, this is reflected by the conditions $E^{(m)}(L) = E^{(m)}(0)$ and $E^{(m+1)} = E^{(m)} = E$. Injecting this relation into Eq. (1.6) gives the following expression for the stationary intracavity field:

$$E = \frac{\theta E_{in}}{1 - \rho\, e^{i\Phi_0}} \tag{1.8}$$

The corresponding cavity response in terms of optical power can then be written:

$$\frac{P}{P_{in}} = \frac{\theta^2/(1-\rho)^2}{1 + F\sin^2\left(\frac{\Phi_0}{2}\right)} \tag{1.9}$$

with $F = 4\rho/(1-\rho)^2$. This expression is similar to the well-known transmittance of a Fabry-Perot interferometer. It should be noted that in this form, this function does not include the losses that are absolutely critical in the operation of the cavity. Linear losses and excess losses of the coupler can be embedded in the reflection and transmission coefficients as follows: $\rho \to a\alpha_0\rho$ and $\theta \to \alpha_0\theta$. In these expressions $a = \exp(-\alpha_f L/2)$ represents the linear losses and $\alpha_0 = \sqrt{1-\kappa_0}$, κ_0 being the percentage of excess losses of the coupler [89]. The cavity response is a 2π-periodic function of the variable Φ_0, maximum for $\Phi_0 = 2k\pi$ ($k \in \mathbb{Z}$), when the waves are in phase inside the cavity. These define the resonances of the system since they correspond to values of Φ_0 for which the intracavity power is maximum and equal to $\theta^2/(1-\rho)^2$. From the definition of the linear phase we can see that it is directly proportional to the carrier frequency ($\Phi_0 = 2\pi f_0 nL/c$).

We can thus introduce the frequency spacing between two consecutive resonances called the *free spectral range* (FSR) which equals $c/(nL)$. Note that it also corresponds to the inverse of the round-trip time of the cavity. Three consecutive resonances are plotted in Fig. 1.2(a) for three values of linear losses. As the losses increase, the resonances widen and become less intense. A practical way of measuring the losses is by means of the finesse $\mathcal{F}$ of the cavity which is defined as the ratio between the FSR and the full width at half-maximum (FWHM) of a resonance. It scales as the quality factor $Q = \mathcal{F} \times f_0/\text{FSR}$. Provided that the losses are small, it can be shown that $\mathcal{F} \approx \pi/\alpha$, where α stands for the overall losses of the system ($\alpha \approx \alpha_f L/2 + \theta^2/2$). A large finesse thus corresponds to low losses. The finesse is related to the cavity photon lifetime in such a way that $\mathcal{F}$ can be seen as the number of round-trips a pulse can circulate inside the cavity before it is almost completely dissipated. Typically, the finesse of a fiber-ring cavity using standard fiber couplers varies from around 10 to 50 [61, 69, 71, 90, 91]. To our knowledge, a record finesse of 1260 has been achieved using a custom-made coupler by carefully reducing the insertion losses [92].

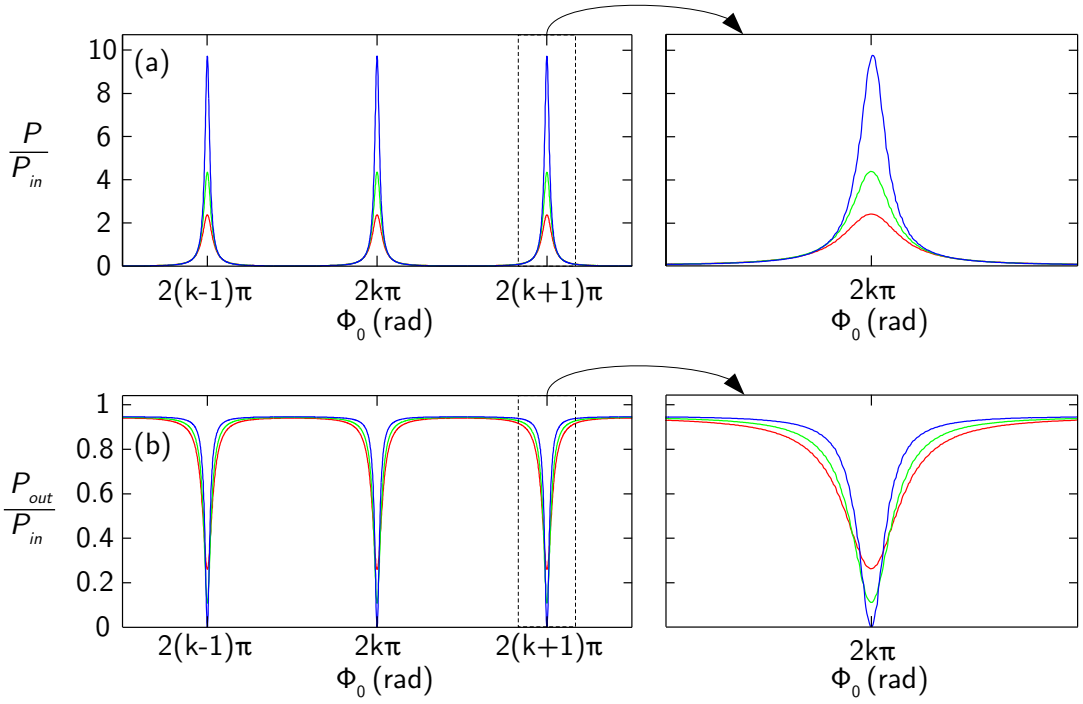

Figure 1.2 – Linear resonances of a passive cavity for three values of internal losses. (a) intracavity response (b) transfer function. Blue, green and red curves are calculated with 5%, 15% and 25% of linear losses respectively or equivalently $a = 0.97$, 0.92 and 0.87 and $\mathcal{F} \approx 30$, 20 and 15. In every cases, $\theta = \sqrt{0.1}$ and $\kappa_0 = 5\%$.

In practice, we cannot directly access the intracavity response of resonators with

a single coupler as described in Fig. 1.1 (this necessitates the inclusion of a second "tap" coupler inside the loop as in Refs. [90, 93–95] for instance). However, at the output port of the coupler, the transfer function appears as a set of inverted peaks corresponding to the energy taken from the pump field to maintain the intracavity power. The mathematical expression of this transfer function is related to the cavity response by [89]:

$$\frac{P_{out}}{P_{in}} = \alpha_0^2 - \left(1 - (a\alpha_0)^2\right)\frac{P}{P_{in}} \tag{1.10}$$

Again, higher losses tend to broaden the resonances and to reduce their amplitude as it appears in Fig. 1.2(b). Generally speaking, it is advantageous to work with the lowest possible losses because it gives the highest intracavity power. This is especially true when investigating nonlinear effects that necessitate rather high powers which is the case in this dissertation.

1.2.2 Impact of the Kerr nonlinearity

In this paragraph we discuss the impact of the Kerr nonlinearity on the cavity response. Taking account of the optical Kerr effect is easily achieved by pointing out that the optical wave which propagates inside the cavity acquires through SPM an additional intensity dependent phase shift $\Phi_{NL} = \gamma LP$ where $P = |E|^2$. The overall phase accumulated over one round-trip is thus $\Phi = \Phi_0 + \Phi_{NL}$ and the cavity response function becomes:

$$\frac{P}{P_{in}} = \frac{\theta^2/(1-\rho)^2}{1 + F\sin^2\left(\frac{\Phi_0+\gamma LP}{2}\right)} \tag{1.11}$$

which is a transcendental equation with respect to the intracavity power P. This nonlinear phase term does not significantly impact the wings of the resonances where P is rather small. However, the tips of the resonances accumulate a comparatively larger nonlinear phase. As a consequence, the position of each resonance's tip is shifted by a value $-\gamma LP_{max}$ where $P_{max} = P_{in} \times \theta^2/(1-\rho)^2$ in our case. It appears thus that the nonlinear shift of the resonance's tips is proportional to the nonlinear coefficient, the cavity length and the input power.

Nonlinear resonances computed from Eq. (1.11) are plotted in Fig. 1.3 for three values of input power. When the cavity response is normalised to the input power (P/P_{in}) (Fig. 1.3(a)), resonances appear more and more tilted as the input power is increased. For sufficiently large tilts (green and blue curves), the cavity response becomes multi-valued. Up to three intracavity powers satisfy Eq. (1.11) for a single value of Φ_0. We will see further that the intermediate branch of the resonance (dashed line) is unstable regarding cw solutions. The cavity can thus operate in a bistable regime owing to the

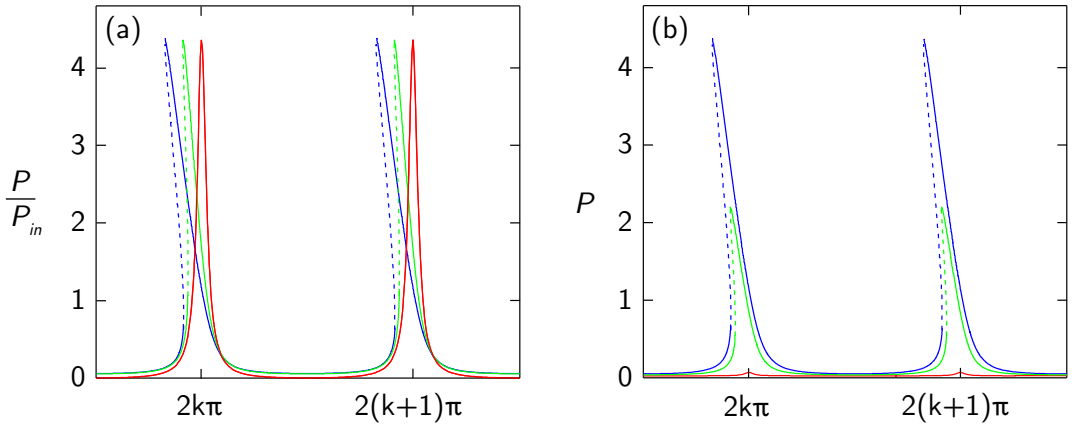

Figure 1.3 – Tilted resonance as a consequence of the Kerr nonlinearity. (a) Nonlinear cavity response for three values of input power. (b) Corresponding intracavity power (not normalised to the input power). Red, green and blue curves correspond to $P_{in} = 0.01,\ 0.5$ and 1 W respectively. $a = 0.92$ $(\mathcal{F} \approx 20)$, $\theta = \sqrt{0.1}$, $\kappa_0 = 5\%$, $\gamma = 5$ /W/km and $L = 50$ m.

Kerr nonlinearity. Fig. 1.3(b) showcases the same resonances as Fig. 1.3(a) but not normalised to the input power. It then appears that the resonances actually "grow" with a tilt angle which is fully determined by γ, L, θ and ρ, as the input power is increased (the maximum intracavity power being directly proportional to the input power).

1.2.3 The Lugiato-Lefever model

The transcendental nature of Eq. (1.11) prevents us from describing analytically the optical bistability of the cavity. Further description thus only relies on numerical simulations of the cavity map system of Eqs. (1.5 - 1.6). However under the condition that only one longitudinal mode of the cavity is excited, we can obtain a very convenient model that opens the way to all the analytical investigations presented in this dissertation. We point out that this model has been originally derived in the so-called mean-field approximation [63, 96], i.e. assuming that the intracavity field does not evolve significantly over a round-trip. This entails several constraints: the cavity is short with respect to nonlinear and dispersion lengths, and both the intensity loss at the coupler and the cavity linear phase shift relative to the closest resonance are small. However this model has proved to hold valid even when these assumptions are violated [64]. For instance, we will describe in Chap. 2 the typical example of parametric modulation instability in dispersion oscillating cavity where the dispersion and the field rapidly change over the scale of a single round-trip. The purpose of this subsection is to detail the derivation and the limits of this model as originally done by Conforti *et al.* [97] .

We start by performing the following phase rotation:

$$A^{(m)}(z,\tau) = E^{(m)}(z,\tau)\, \mathrm{e}^{i\beta_0 z} \tag{1.12}$$

in order to incorporate the rapid phase variation into the NLSE and remove it from the boundary conditions. The equations for the fast variable A are:

$$\begin{cases} A^{(m+1)}(z=0,\tau) = \theta E_{in}(\tau) + \rho A^{(m)}(z=L,\tau) \\ i\dfrac{\partial A^{(m)}}{\partial z} + \beta_0 A^{(m)} - \dfrac{\beta_2(z)}{2}\dfrac{\partial^2 A^{(m)}}{\partial \tau^2} + \gamma |A^{(m)}|^2 A^{(m)} = 0 \end{cases} \tag{1.13}$$

where we neglect the linear losses that will be reintroduce at the end for completeness. Note that we introduced here the fact that the GVD can be a function of the longitudinal coordinate z. This will be the case when we will develop the concept of longitudinally modulated cavity in the next chapter. Now we let the spatial variable to assume all values from 0 to infinity, i.e. we *unfold* the cavity. Even if z is a continuous variable, the field is physically accessible only at the coupler, i.e. at distances $z = mL$. We incorporate the boundary conditions in the propagation equation with the aid of the delta function, so that we can write Eqs. (1.13) in the following equivalent compact form:

$$i\frac{\partial A}{\partial z} + \beta_0 A - \frac{\beta_2(z)}{2}\frac{\partial^2 A}{\partial \tau^2} + \gamma |A|^2 A = i[\theta E_{in}(\tau) + (\rho - 1)A] \sum_m \delta(z - mL) \tag{1.14}$$

By expanding the delta comb in Fourier series:

$$\sum_m \delta(z - mL) = \frac{1}{L}\sum_m \mathrm{e}^{im\frac{2\pi}{L}z} = \frac{1}{L}\sum_m \mathrm{e}^{imkz} \tag{1.15}$$

we get

$$i\frac{\partial A}{\partial z} + \beta_0 A - \frac{\beta_2(z)}{2}\frac{\partial^2 A}{\partial \tau^2} + \gamma |A|^2 A = i\frac{\theta}{L}E_{in}\sum_m \mathrm{e}^{imkz} i\frac{\rho - 1}{L} A \sum_m \mathrm{e}^{imkz} \tag{1.16}$$

In order to recognize exponential terms oscillating at the same rate, we come back to the slow variable $E = A\exp(-i\beta_0 z)$:

$$i\frac{\partial E}{\partial z} - \frac{\beta_2(z)}{2}\frac{\partial^2 E}{\partial \tau^2} + \gamma |E|^2 E = i\frac{\theta}{L}E_{in}\sum_m \mathrm{e}^{i(mk-\beta_0)z} + i\frac{\rho - 1}{L} E \sum_m \mathrm{e}^{imkz} \tag{1.17}$$

Equation (1.17) is a NLSE forced by two combs with equal wavenumber spacing $k = 2\pi/L$ and a relative shift β_0. The solution of Eq. (1.17) can be written as a sum of slowly-varying envelopes, which modulates the longitudinal modes of the cavity, as

$E(z,\tau) = \sum_m E_m(z,\tau)\ \exp(imkz)$.

It is of fundamental importance to choose the correct forcing terms for each mode, in order to neglect the fast-rotating exponential in favour of the slowly evolving ones. When the intracavity power is reasonably small, we can assume that we have only one mode present in the cavity, which we label, without loss of generality, $m = 0$, i.e.

$$E(z,\tau) = E_0(z,\tau) \tag{1.18}$$

This assumption permits to describe all the phenomena we will observe in our experiments and in most of the situations. Only when several longitudinal modes are present in the cavity, as recently predicted [98] and observed [91] in tristable resonators, the model ceases to be valid and a more complex one has to be used [99, 100]. *It is worth noting that the single longitudinal mode operation is the only hypothesis that we made so far* to describe the work presented in this dissertation.

We retain only the quasi-phase-matched forcing terms is Eq. (1.17), i.e. the terms that are multiplied by the exponential with the smallest argument. We find:

$$i\frac{\partial E_0}{\partial z} - \frac{\beta_2(z)}{2}\frac{\partial^2 E_0}{\partial \tau^2} + \gamma|E_0|^2 E_0 = \frac{i\theta}{L}E_{in}\mathrm{e}^{i\delta_0 z/L} + i\frac{\rho-1}{L}E_0 \tag{1.19}$$

where the cavity detuning δ_0 is defined as follows

$$\frac{\delta_0}{L} = mk - \beta_0, \qquad m = \arg(\min_m(|mk-\beta_0|)) \tag{1.20}$$

which implies $\delta_0 \in [-\pi, \pi]$. This fixes the detuning validity range of the equation. Any choice $|\delta_0| > \pi$ means that we have neglected the slowest oscillating term in favour of a rapid one, which means that we have chosen the wrong m in the first summation in Eq. (1.17). *Note that we do not need to assume that the detuning is small*, at variance with previous approaches [63, 96].

We can remove the exponential from the pump by the phase rotation $E_0(z,\tau) = E(z,\tau)\exp(i\delta_0 z/L)$ to find the equation:

$$\boxed{i\frac{\partial E}{\partial z} - \frac{\beta_2(z)}{2}\frac{\partial^2 E}{\partial \tau^2} + \gamma|E|^2 E = i\frac{\theta}{L}E_{in} + \left(\frac{\delta_0}{L} - i\frac{\alpha}{L}\right)E} \tag{1.21}$$

where α accounts for the losses. The linear losses can be reintegrated here, by considering that $\alpha = \alpha_f L/2 + (1-\rho)$ represents the total round-trip losses. Equation (1.21) is often referred to as the Lugiato-Lefever equation (LLE) in reference to the model first derived in 1987 [96]. In their work the authors considered a passive diffractive cavity. In our case, we find that the diffraction is replaced by the chromatic dispersion (single

mode optical fibers are, by definition, not susceptible to transverse diffraction). This equivalence has been first identified in the seminal paper of Haelterman *et al.* in 1992 on modulation instability in dispersive ring cavities [63]. To summarize, under the only hypothesis of single longitudinal mode operation, the full cavity map equations can be approximated by a single differential equation that allows a direct analytical treatment. Now the validity of the single longitudinal mode approximation can be questionned. Indeed, it can be violated in several ways:

• As pointed out earlier, when the input power is important, the Kerr nonlinearity can induce a very large tilt of the resonances such that for one value of the detuning, more than one resonance can be simultaneously excited [91, 98–100]. This never occurs in the work presented in this dissertation;

• When the cavity is pumped by a train of pulses (which is the case in the experimental results presented afterwards), the spectrum of the input field contains multiple components spaced by the repetition rate of the pulses. Under the condition of synchronous pumping, this repetition rate equals the FSR of the cavity such that each spectral component excites a different longitudinal mode. However, since each component is detuned by the same amount with respect to its closest resonance, they are conceptually "brought back" toward the central mode described by the LLE [101]. Mathematically speaking, this is inplicitly taken into account in the LL Eq. (1.21) which describes the evolution of the field in the reference frame travelling at group velocity $1/\beta_1$. The LLE thus remains valid under the condition of synchronous pumping;

• The actual limit of validity of the single longitudinal mode approximation comes from the fact that each spectral component of the input field acquires a different phase shift due to chromatic dispersion. In order for our approximation to stay valid, the phase variation due to chromatic dispersion over the width of the pump spectrum must be very small compared to the linewidth of the cavity resonances, that is:

$$\frac{\beta_2 L \Delta\omega^2}{2} \ll \frac{2\pi}{\mathcal{F}} \tag{1.22}$$

where $\Delta\omega$ is the bandwidth of the pump spectrum. We verified that this condition is always fulfilled in our studies. In the end, the condition of single longitudinal mode operation, while seemingly restrictive, holds valid for a large range of configurations, including ours.

We can find that the steady state ($\partial E/\partial z = 0$) continuous wave ($\partial^2 E/\partial \tau^2 = 0$) solutions of Eq. (1.21) correspond to the following expression:

$$\boxed{\frac{P}{P_{in}} = \frac{\theta^2}{(\delta_0 - \gamma L P)^2 + \alpha^2}} \tag{1.23}$$

This equation can be used to plot the cavity response corresponding to the LL model. An example is depicted in Fig. 1.4(a) as a black line superimposed on the corresponding cavity response calculated with the map model (Eq. (1.11)) in grey for the resonance around $\delta_0 = 0$. We can see that the LL model accurately reproduces this resonance, however, Fig. 1.4(b) shows that it fails to describe the neighbouring ones as a consequence of the single longitudinal mode hypothesis. This becomes a limitation when considering large detunings and/or highly nonlinear regimes. That latter case corresponds to the situation where the nonlinear phase shift is large enough to shift the tip of a resonance close to another resonance [91, 98–100]. In our work, we do not address these cases and the LLE will always give satisfying results. Note that Eq. (1.23) takes the form of a single Lorentzian function with a FWHM of 2α. We thus retrieve the fact that the finesse is $\mathcal{F} \approx 2\pi/2\alpha = \pi/\alpha$.

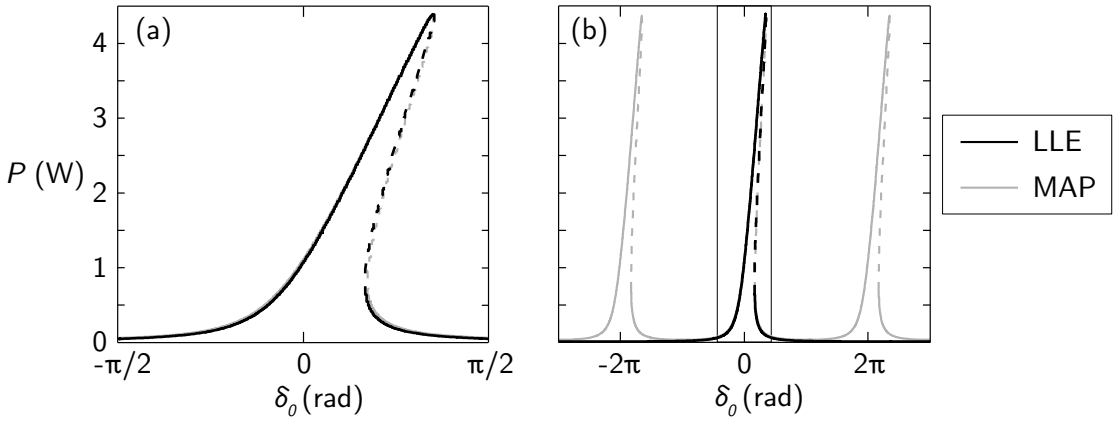

Figure 1.4 – Comparison of the cavity response $P = f(\delta_0)$ calculated from the Lugiato-Lefever model (black curve, Eq. (1.23)) and the cavity map (grey curve, Eq. (1.11)). $P_{in} = 1\,\mathrm{W}$, $a = 0.92$ ($\mathcal{F} \approx 20$), $\theta = \sqrt{0.1}$, $\kappa_0 = 5\%$, $\gamma = 5\,/\mathrm{W/km}$ and $L = 50\,\mathrm{m}$. For the LL model $\alpha = 0.151$.

Another representation of the cavity response which is extensively used in this dissertation is the function $P = f(P_{in})$. We first demonstrate that this cavity response is multi-valued for a range of input power whenever δ_0 exceeds a threshold. In that latter case, the function $P = f(P_{in})$ takes the form of a S-shaped curve which consists in two positive slope branches connected via a negative slope branch. Mathematically, the cavity response is multi valued when the intermediate branch exists which is the case for $P_- < P < P_+$ with [101]:

$$P_{\pm} = \frac{2\delta_0 \pm \sqrt{\delta_0^2 - 3\alpha^2}}{3\gamma L} \tag{1.24}$$

$P_{\pm}$ are the roots of $\partial P_{in}/\partial P = 0$. The cavity response is then multi-stable whenever the square root in Eq. (1.24) is real which is the case when $\delta_0 > \sqrt{3}\alpha$. We next demonstrate that in our case, the negative slope branch of $P = f(P_{in})$ is unstable. It consists in performing the linear stability analysis of the LLE (1.21) relative to the ansatz $E = E_s + b\exp(\lambda t)$. After straightforward calculations we find that the system is unstable whenever the following expression of λ is positive [63, 64, 101]:

$$\lambda = -\frac{\alpha}{L} \pm \sqrt{4\gamma P \frac{\delta_0}{L} - \left(\frac{\delta_0}{L}\right)^2 - 3(\gamma P)^2} \tag{1.25}$$

A trivial analysis of Eq. (1.25) shows that it is the case for the exact same domain $P_- < P < P_+$ that corresponds to the negative slope branch. We thus demonstrate that the intermediate branch of $P = f(P_{in})$ or $P = f(\delta_0)$ is unstable regarding continuous wave perturbations. The regime of operation of the cavity where $\Delta = \delta_0/\alpha > \sqrt{3}$ is usually called the *bistable regime* (note that we introduce here the normalized detuning Δ which will be useful after). To illustrate this, Fig. 1.5(a) shows the cavity response calculated with the LL model (Eq. (1.23)) as a black curve and with the full cavity map in grey (Eq. (1.11)) in the bistable regime (i.e. a maximum of two stable steady state solutions exist for a limited range of input power). For rather low powers, the results are pretty similar except around the up-switching knee $(P_{in}^{\uparrow}; P_-)$ which means that the description of the system close to that point by the LL model might slightly differ from the one by the cavity map (this is the case in terms of instability thresholds for instance). However, for significantly larger powers the steady-state cavity response curves strongly differ as illustrated in Fig. 1.5(b). Indeed, the periodic structure of the resonances is responsible for additional, large amplitude, zig-zags in the curve calculated with the cavity map equation (1.11). For the same reasons as described previously, this discrepancy will not impact our work. From now on, the LL model will be used for every numerical results presented unless otherwise stated.

To conclude this section, we note that the two representations of the cavity response are linked but the S-shaped curve ($P = f(P_{in})$) is more pertinent in our case. Indeed, most of our experiments are realized by fixing the detuning and changing the input power P_{in} as it will be described in the following chapters.

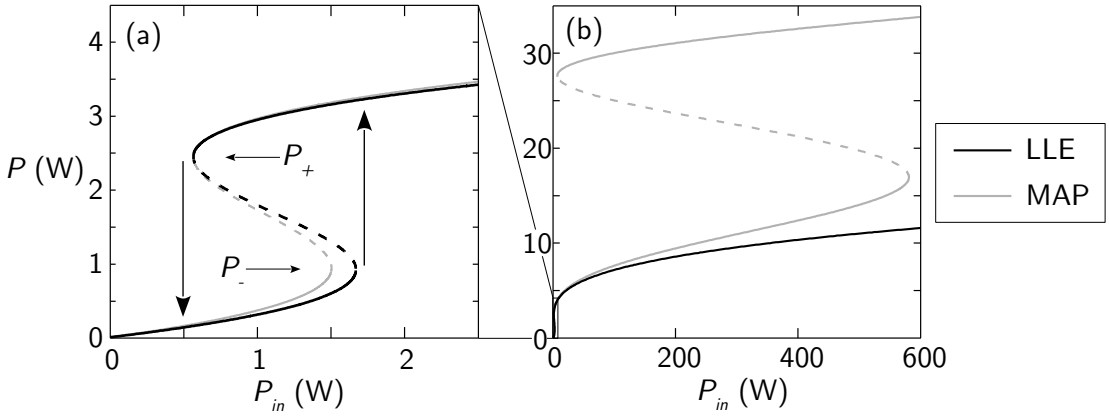

Figure 1.5 – Comparison of the cavity response $P = f(P_{in})$ calculated from the Lugiato-Lefever model (black curves) and the cavity map (grey curves). (a) is a close-up version of (b) in the low power region. $\delta_0 = \pi/5\,\text{rad}$, $a = 0.92$ ($\mathcal{F} \approx 20$), $\theta = \sqrt{0.1}$, $\kappa_0 = 5\%$, $\gamma = 5\,/\text{W/km}$ and $L = 50\,\text{m}$. For the LL model $\alpha = 0.151$.

Figure 1.6 is thus intended to clarify how to switch from one representation to the other. On the first hand, let's consider Fig. 1.6(a) which represents a resonance at fixed input power $P_{in} = 1\,\text{W}$ with a finesse of ≈ 20. Due to the Kerr nonlinearity, the resonance is tilted toward positive detunings. Starting from $\delta_0 = 0$ and increasing the detuning, the intracavity power P goes from single valued, to bi-valued for a critical detuning (pointed out by a green star), to tri-valued as can be seen by the red, green and blue markers and lines respectively. For even higher detunings, P becomes single valued again. Note that, for $\Delta < \sqrt{3}$ or equivalently $\delta_0 < \pi/12$ in this case, the system is monostable regardless of the input power. This region is highlighted by the light yellow background. In terms of bistable response (see Fig. 1.6(b)) we can see that, as the detuning increases, the S-shape becomes more and more pronounced and for the input power considered we retrieve the same intracavity powers (the critical detuning mentioned earlier corresponding to the up-switching knee of the bistable curve in green, see the green star). On the other hand, let's now consider Fig. 1.6(c) which showcases a bistable response at fixed detuning $\delta_0 = \pi/5\,\text{rad}$. Starting from 0 and increasing the input power, the intracavity power can at first only take one value on the lower branch, then three on the lower, intermediate and upper branches respectively and then a single one on the upper branch. The corresponding tilted resonances are represented in Fig. 1.6(d). As in Fig. 1.3(b), the amplitude of the resonance grows with the input power. For the value of detuning considered here, the system is bistable ($\delta_0 = \pi/5 > \pi/12$). If initially, the intracavity field lies on the lower branch of the bistable curve, when the input power exceeds the up-switching knee ($P_{in}^{\uparrow}$) we say that the system has switched from the lower branch to the upper branch of the bistable response. Conversely, if

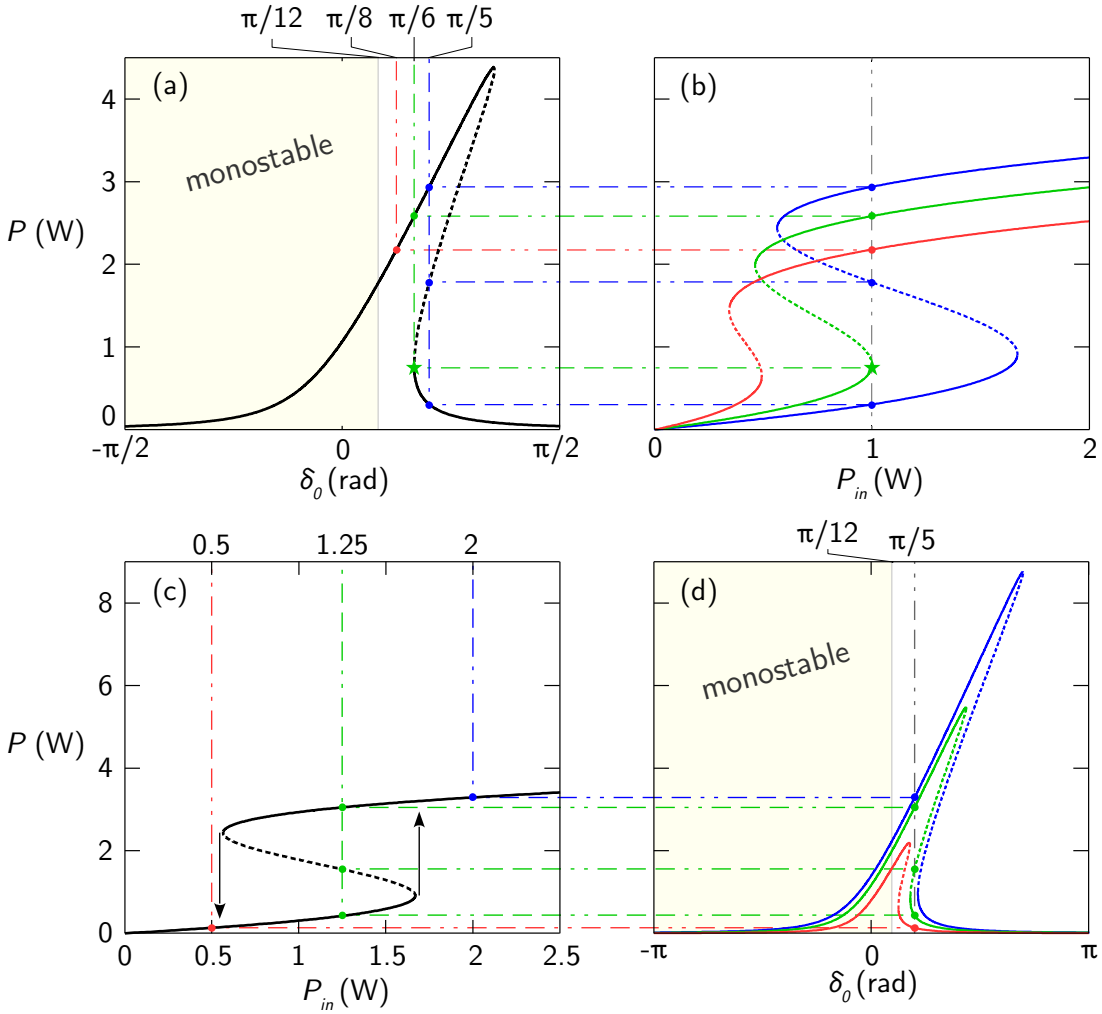

Figure 1.6 – Correspondence between the cavity resonance and the S-shape curve representation for (a-b) three different detunings ($\delta_0 = \pi/8, \pi/6$ and $\pi/5$ rad) at fixed input power ($P_{in} = 1$ W) and (c-d) three different input powers $P_{in} = 0.5, 1.25$ and 2 W at fixed detuning ($\delta_0 = \pi/5$). Calculated with the LL model through Eq. (1.23). $\gamma = 5$ /W/km, $L = 50$ m, $\alpha = 0.151$.

initially, the intracavity field lies on the upper branch of the bistable curve, the system switches from the upper branch to the lower branch of the bistable response when the input power is decreased below the down-switching knee ($P_{in}^{\downarrow}$). This behaviour defines an hysteresis cycle characteristic of the bistable regime (materialized by the arrows in Fig. 1.6(c)). In the rest of this dissertation, we will thus indifferently refer to the S-shape curve as the bistable curve/response/cycle.

1.3 Summary

- We introduced the fundamental parameters involved in the propagation of light in optical fibers, namely, linear losses, chromatic dispersion and Kerr nonlinearity. These parameters appear in the nonlinear Schrödinger equation which describes the propagation of light along optical fibers.
- By means of *cavity boundary conditions*, we described the basic operation of optical ring resonators and the influence of losses and nonlinearity on the cavity resonances.
- The Lugiato-Lefever model has been derived and its steady-state, continuous wave solutions have been compared to those of the Ikeda map model.
- We described how the Kerr nonlinearity introduces a bistable regime and, subsequently, hysteresis. The complementarity between the nonlinear resonance and the bistable response of the cavity has been described.

CHAPTER 2

Theory of intracavity modulation instability

In this chapter we describe the process of modulation instability (MI) that occurs in optical Kerr cavities. More generally, MI is unarguably the most ubiquitous nonlinear phenomenon [102], whether it is in hydrodynamics [16], plasma physics [17], Bose -Einstein condensates [18, 103] or optics [15]. In its best known form, it can be seen as a long-wave instability at the origin of the exponential growth of a weak periodic modulation in the time or the spatial domain. In the spectral domain, MI finds expression in the generation of primary sidebands on both sides of the carrier field. In optical fibers, the appearance of MI is often interpreted as the result of an interplay between dispersion and nonlinearity. Since its first observation back in 1986 [15], a tremendous amount of work has been focussed on this process leading to some salient applications such as optical parametric amplification [20, 21] or the generation of very broad, rather flat spectra called supercontinua [25, 26].

On a different note, MI has also been investigated in the cavity configuration as it is evidenced by the first experimental observation of "*intracavity MI*" in 1988 [62]. Contrary to the single-pass configuration, intracavity MI results from a double balance between dispersion and nonlinearity on one side, and losses and driving on the other side. Also called "additive MI" [64] or "dissipative MI" [63], it has been widely studied both theoretically and experimentally, in particular because it is responsible for the formation of stationary temporal structures.

In the first section, we recall the key aspects of the MI process in uniform ring cavities also called *Turing instability*. In the second section, we detail our original theoretical study of the MI process in "dispersion oscillating" cavities. By means of a Floquet analysis, we identify a new type of parametric modulation instability that is closely linked to the *Faraday instability*.

2.1 The case of uniform dispersion - Turing instability

2.1.1 Linear stability analysis

The results presented in this section have already been reported in the literature and are at the origin of most studies of the MI process in passive ring cavities [63, 64]. We recall the method and the results obtained since they constitute the prerequisites to understand the original study of MI in dispersion oscillating cavities that follows.

The starting point of this study is the LLE previously derived that we repeat here for convenience:

$$i\frac{\partial E}{\partial z} - \frac{\beta_2}{2}\frac{\partial^2 E}{\partial \tau^2} + \gamma|E|^2 E = i\frac{\theta}{L}E_{in} + \left(\frac{\delta_0}{L} - i\frac{\alpha}{L}\right)E \tag{2.1}$$

The cavity steady-states can destabilize through the exponential growth of modulations, this is the MI process. In uniform ring cavities it is often said that the system is destabilized by a *Turing mechanism* or *Turing instability* by analogy with the mechanism of pattern formation in the context of chemical systems ruled by reaction-diffusion equations [104, 105]. To describe this mechanism, we perform a linear stability analysis of the LLE by looking at the evolution of a perturbed solution $E(z,t) = \sqrt{P_s} + [u(z,\tau) + iv(z,\tau)]$, where P_s is the intracavity steady-state power and u, v are real functions. u and v denote the perturbation applied to the steady-state so $u, v \ll \sqrt{P_s}$. By linearising the LLE (2.1) relative to this ansatz, we obtain the following set of two coupled partial differential equations:

$$\begin{cases} \dfrac{\partial u}{\partial z} = \dfrac{\beta_2}{2}\dfrac{\partial^2 v}{\partial \tau^2} - \dfrac{\alpha}{L}u - \left(\gamma P_s - \dfrac{\delta_0}{L}\right)v \\ \dfrac{\partial v}{\partial z} = -\dfrac{\beta_2}{2}\dfrac{\partial^2 u}{\partial \tau^2} - \dfrac{\alpha}{L}v + \left(3\gamma P_s - \dfrac{\delta_0}{L}\right)u \end{cases} \tag{2.2}$$

We then introduce the Fourier transforms in time $[\hat{u}(z,\omega) = \int u(z,\tau)e^{i\omega\tau}d\tau]$ and $[\hat{v}(z,\omega) = \int v(z,\tau)e^{i\omega\tau}d\tau]$ where ω now refers to the angular frequency shift relative to the pump angular frequency. This allows to rewrite (2.2) as a system of first order ordinary differential equations:

$$\frac{d}{dz}\begin{pmatrix} \hat{u} \\ \hat{v} \end{pmatrix} = \begin{pmatrix} -\dfrac{\alpha}{L} & -g(\omega) \\ h(\omega) & -\dfrac{\alpha}{L} \end{pmatrix}\begin{pmatrix} \hat{u} \\ \hat{v} \end{pmatrix} \tag{2.3}$$

where

$$\begin{cases} g(\omega) = \dfrac{\beta_2\omega^2}{2} + \gamma P_s - \dfrac{\delta_0}{L} \\ h(\omega) = \dfrac{\beta_2\omega^2}{2} + 3\gamma P_s - \dfrac{\delta_0}{L} \end{cases} \tag{2.4}$$

We note that the system (2.3) is similar to a damped harmonic oscillator whose undamped angular frequency is:

$$k = \sqrt{gh} = \sqrt{\left(\frac{\beta_2\omega^2}{2} + 2\gamma P_s - \frac{\delta_0}{L}\right)^2 - (\gamma P_s)^2} \tag{2.5}$$

The eigenvalues of the matrix in (2.3) read $-\alpha/L \pm ik$. For sufficiently large values of the detuning δ_0, k can be imaginary for a certain range of frequency ω, and the two eigenvalues become real. The solution of Eqs. (2.3) then involves two exponentials with real argument. In this range, if $|k| > \alpha/L$ one of the eigenvalue is positive and the perturbations $\hat{u}$ and $\hat{v}$ grow exponentially as $\exp[G(\omega)z]$ with the growth rate:

$$G(\omega) = -\frac{\alpha}{L} + \sqrt{-gh} = -\frac{\alpha}{L} + \sqrt{(\gamma P)^2 - \left(\frac{\beta_2\omega^2}{2} + 2\gamma P - \frac{\delta_0}{L}\right)^2} \tag{2.6}$$

This entails the modulation instability of the steady-state solution through the Turing mechanism. The most unstable Turing frequency ω_T and its corresponding growth rate, or gain $G(\omega_T)$ are easily calculated to be:

$$\omega_T = \sqrt{\frac{2}{\beta_2}\left(\frac{\delta_0}{L} - 2\gamma P_s\right)}\ , \qquad G(\omega_T) = -\frac{\alpha}{L} + \gamma P_s \tag{2.7}$$

2.1.2 Conditions of instability

The latter expressions fix under which conditions MI can arise in the cavity. Indeed, for MI to occur, the two conditions $\omega_T > 0$ and $G(\omega_T) > 0$ must be fulfilled. Two distinct cases appear depending on the sign of β_2 and are summarized below:

$$\begin{aligned} &\bullet \ \text{If} \ \ \beta_2 < 0 \quad \rightarrow \quad P > P_{th} \ \text{ and } \ P > P_\omega \\ &\bullet \ \text{If} \ \ \beta_2 > 0 \quad \rightarrow \quad P > P_{th} \ \text{ and } \ P < P_\omega \end{aligned} \tag{2.8}$$

where $P_{th} = \alpha/(\gamma L)$ and $P_\omega = \delta_0/(2\gamma L) = \Delta\alpha/(2\gamma L)$.

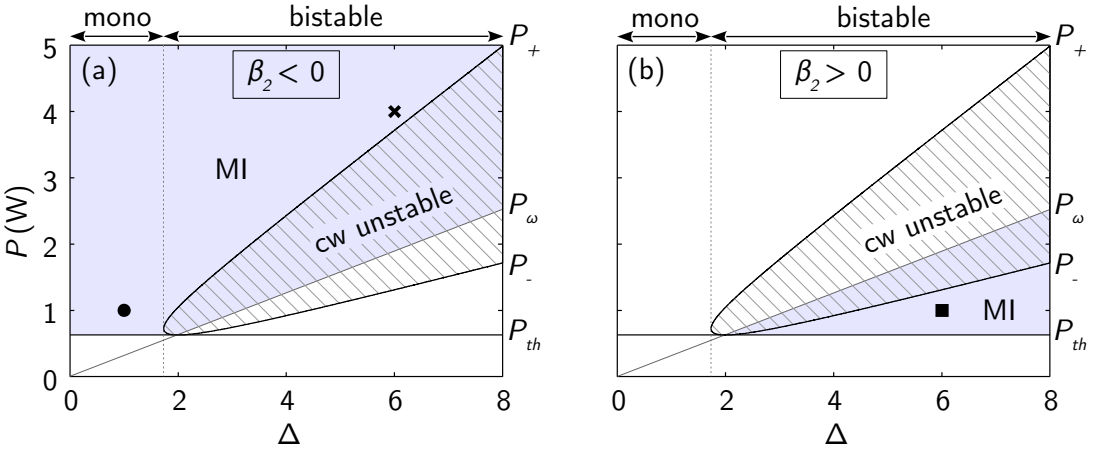

Figure 2.1 – Domains of Turing instability in the (Δ, P) plane for the (a) anomalous and (b) normal dispersion regimes. Modulationally unstable domains are shaded and continuous wave unstable domains (labelled *"cw unstable"*) are hatched. The black bullet, cross, and square symbols mark the examples illustrated in Figs. 2.2(c), 2.2(f) and 2.3(c) respectively. $\gamma = 5$ /W/km, $L = 50$ m, $\alpha = 0.157$.

Quite noteworthy is the fact that, contrary to the single-pass configuration where MI only occurs in the anomalous GVD regime, the contribution of the linear detuning δ_0 extends the range of existence of MI to the normal GVD regime [63, 64]. Another difference lies in the fact that the Turing instability only occurs over a power threshold P_{th} obtained by imposing $G(\omega_T) > 0$ in Eq. (2.7) whatever the sign of β_2. These results are summed up graphically in Fig. 2.1 as a function of the normalized detuning Δ.

Hatched areas, labelled "*cw unstable*", correspond to the regions that are unstable with respect to homogeneous perturbations (negative slope branch of the bistable curve between P_- and P_+), shaded areas to the modulationally (Turing) unstable regions and blank areas to stable domains. If $\beta_2 < 0$ (Fig. 2.1(a)), MI might arise in the monostable regime whenever $P > P_{th}$ and on the upper branch of the bistable response when it exists ($P > P_+$). Conversely, if $\beta_2 > 0$ (Fig. 2.1(b)), MI can only appear in the bistable regime when $\Delta > 2$ ($\Delta = 2$ corresponds to the intersection of P_{th} and P_ω) and is confined to a relatively smaller domain of intracavity power corresponding to the end of the lower branch of the bistable response ($P_{th} > P > P_-$).

At each point of the (Δ, P) plane is associated a Turing frequency, defined by Eq. (2.7), at which a perturbation is likely to grow exponentially. More generally, Eq. (2.6) gives the gain spectrum associated to the propagation of a monochromatic wave inside the cavity. This gain spectrum only features two sidebands symmetrically located around the pump. To gain further insight into the Turing instability process we describe the characteristic shape of the gain spectrum in the different regions revealed in Fig. 2.1.

In the anomalous GVD region (see Fig. 2.1(a)), two distinct cases exist, namely the monostable regime and bistable regime. These two cases are illustrated in Fig. 2.2. In the monostable regime (Fig. 2.2(a-c)), the system becomes modulationally unstable as soon as P exceeds P_{th}. We highlight this on the cavity response curve (Fig. 2.2(a)) by a transition from a black (stable) to a thicker green line (Turing). The gain spectrum calculated from Eq. (2.6) as a function of P is represented in Fig. 2.2(b) as a 2D color plot and displays two sidebands of increasing amplitude shifting away from the central frequency as P increases. Accordingly, the sidebands appear just above the threshold P_{th}. The position of the most unstable frequency calculated from Eq. (2.7) is superimposed as a dashed black line and corresponds to the maximum of the gain band: we should mention that this equation predicts a position of maximum gain even below the MI threshold but is obviously not associated to MI gain. An example of gain spectrum in this region is displayed in Fig. 2.2(c). For higher detunings ($\Delta = 6$ for instance), the system is bistable and MI appears on the upper branch. Fig. 2.2(d-f) shows an example of gain mapping in this case. The main difference with the monostable case is the cw unstable region separating the lower from the upper branch of the bistable response in Fig. 2.2(e) (gray shaded region) which corresponds to the intermediate branch of Fig. 2.2(d). We note that the inaccessibility of this region is visible through the fact that the gain at the pump frequency ($\omega = 0$) is non-zero which entails instability of the steady-state regarding cw perturbations (see Sec. 1.2.3 p. 18). Two broad Turing sidebands are visible on the upper portion of Fig. 2.2(e) with a gain quite similar to the monostable case. The peak gain of the sidebands is roughly 10 times larger in the bistable case compared to what is highlighted in the monostable case as it appears by

comparing Fig. 2.2(f) and 2.2(c) respectively.

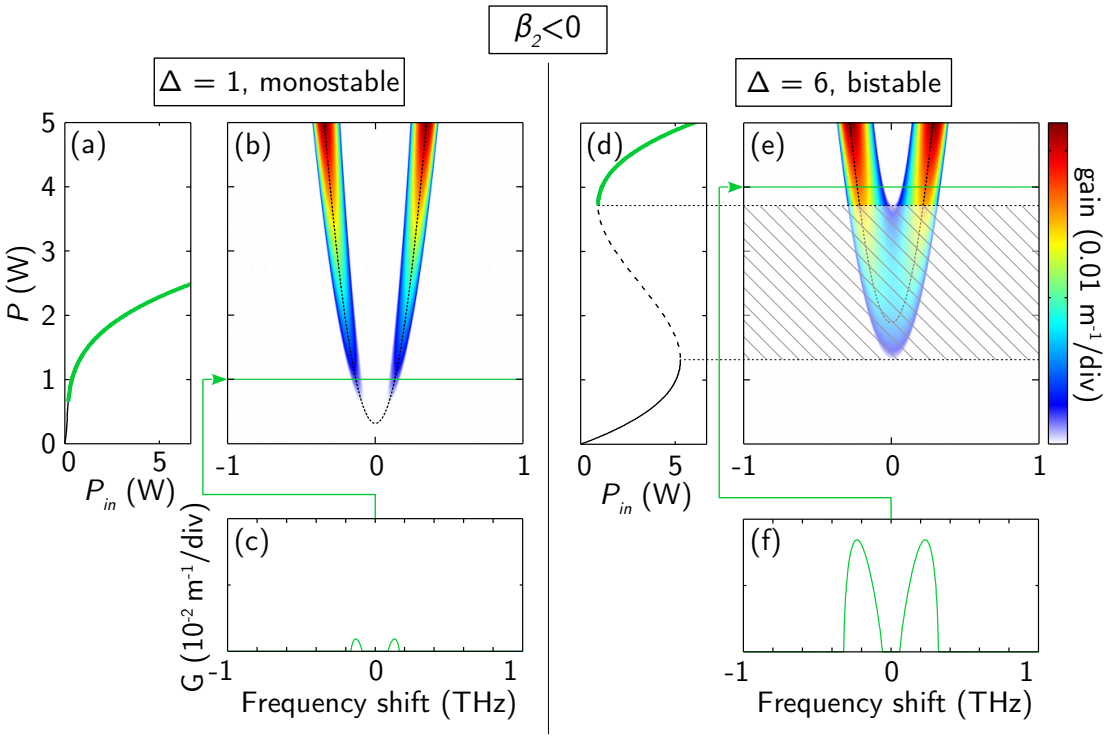

Figure 2.2 – Gain mapping for a uniform cavity with anomalous GVD in the monostable regime (a-c) and the bistable regime (d-f). (a, d) Cavity response curves for $\Delta = 1$ and 6 respectively, the portions experiencing Turing instability are in green. (b, e) 2D color plots of the gain spectrum (Eq. (2.6)), with the position of the maximum gain calculated from Eq. (2.7) superimposed as dashed black lines. (c, f) Gain spectra corresponding to two specific powers in the two regimes respectively. $\gamma = 5\,/\mathrm{W/km}$, $L = 50\,\mathrm{m}$, $\alpha = 0.157$, $\beta_2 = -20\,\mathrm{ps}^2/\mathrm{km}$.

In the normal GVD region, intracavity MI only arises on a portion of the lower branch of the bistable curve lying between the threshold P_{th} and the up-switching knee P_{-}. This is represented in Fig. 2.3(a) for $\Delta = 6$. The corresponding gain mapping of Fig. 2.3(b) shows that two weak sidebands exist just under the cw unstable domain. These bands shift toward the central frequency as P increases until they merge together at the end of the lower branch.

It is very important to emphasize that these last figures result from a linear stability analysis of the LLE (2.1). It allows to determine the conditions of instability and the shape of the gain spectrum with respect to weak perturbations but does not provide any information on the dynamics of large amplitude modulated states. In other words, MI is the generating mechanism of the Turing pattern but only in a subset of the unstable region, the growth of the sideband can generate a stable longitudinal pattern. The

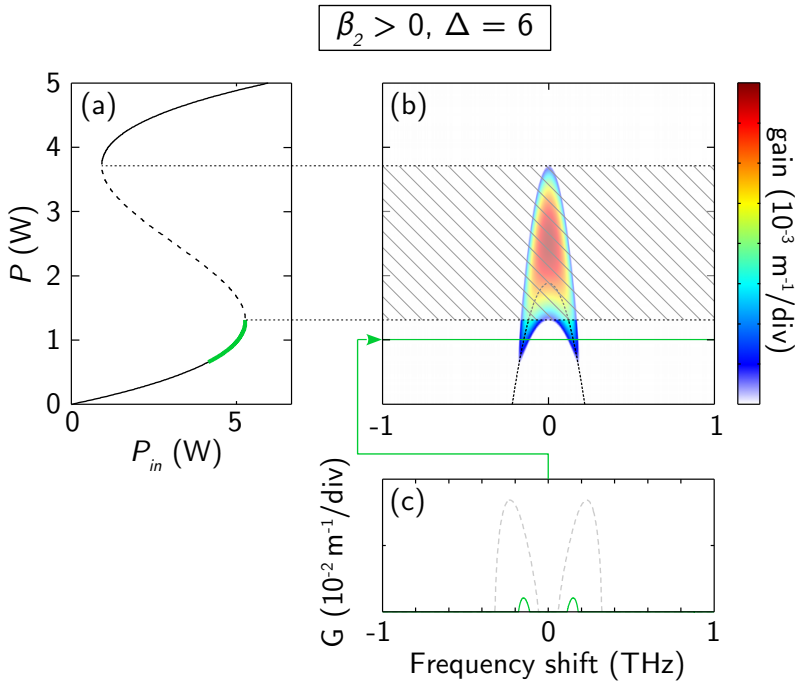

Figure 2.3 – Gain mapping for a uniform cavity with normal GVD in the bistable regime. (a) Cavity response curve for $\Delta = 6$, the portion experiencing Turing instability is in green. (b) 2D color plot of the gain spectrum (Eq. (2.6)), with the position of the maximum gain calculated from Eq. (2.7) superimposed as a dashed black line. (c) Gain spectrum corresponding to $P = 1\,\mathrm{W}$. The gain spectrum obtained in the anomalous regime (Fig. 2.2(f)) is displayed as a dashed gray line for comparison. $\gamma = 5\,/\mathrm{W/km}$, $L = 50\,\mathrm{m}$, $\alpha = 0.157$, $\beta_2 = 20\,\mathrm{ps}^2/\mathrm{km}$.

intracavity field can even evolve toward spatio-temporal chaos but the linear stability analysis does not allow to characterize these regimes.

We focus here on the normal GVD regime and we recall results obtained by S. Coen *et al.* regarding the stability of the Turing pattern in that case [68]: By analogy with the results of Lugiato and Lefever obtained for instabilities in the transverse plane [96], one can deduce that in the bistable regime, the system bifurcates *subcritically* from the steady-state lower branch to a MI (Turing) branch as P exceeds the threshold P_{th}. That implies that the amplitude of the Turing pattern is "large" even close to threshold which prevent one from obtaining an accurate description of these patterns out of a weakly nonlinear analysis. To circumvent this, the method proposed by S. Coen *et al.* involves a three mode truncation ($\omega = 0, \pm\omega_T$) which allows to calculate the Turing branch and to determine its stability. The important result of this analysis, to which we will refer to on several occasions in the course of this dissertation, is that the system can exhibit stable Turing patterns only if $\Delta > 4.25$. This is illustrated in Fig. 2.4 which displays the

Turing bifurcation diagrams for three values of the normalized detuning Δ, all other parameters being fixed to the same values as those used in Fig. 2.3.

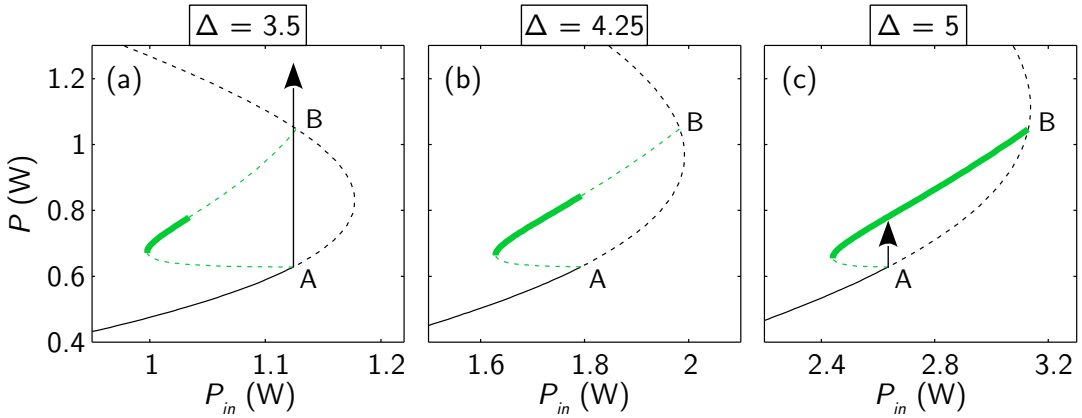

Figure 2.4 – Turing bifurcation diagrams for three values of the nomalized detuning Δ. The cw steady-state branch is represented as solid black lines and the stable portion of the Turing branch is in green. Dashed lines denote unstable states. This figure is largely inspired by Fig. 3 of Ref. [68].

The Turing branch starts from the MI threshold labelled A and is connected at the other end to the steady-state curve at the point labelled B. For $\Delta < 4.25$, a portion of the Turing branch is stable but not for input power P_{in} exceeding the MI threshold. In that case, when the input power is increased above the MI threshold the system is forced to switch to the only existing stable state which is the upper branch of the bistable curve. The range of stability of the Turing branch increases with the detuning and for $\Delta \geq 4.25$ (Fig. 2.4(b, c)) the stable portion of this branch becomes accessible above MI threshold. This analysis shows that the conditions for the excitation of a stable Turing pattern in the normal GVD regime are more constraining than the one found through the linear stability analysis alone. Note that when $\Delta < 4.25$ the MI process still exists above threshold but it competes with the up-switching process. In that case, the Turing instability can be seen as the triggering mechanism behind the up-switching process. This competition has been clearly observed experimentally by Coen et Haelterman [68]. We deliberately do not extend here this calculation to the other regimes under which MI might occur, but we point out that we will see in Chap. 5 that the LLE can be completed by including higher order dispersion terms. Note that we will make use of numerical simulations to delimit the domain of stable operation of the cavity in another context in Chap. 4.

2.1.3 The Turing pattern

We showed that a Turing mechanism is responsible for the exponential growth of weak harmonic perturbations of the steady-state of the cavity. In that sense, the Turing instability is similar to the well known modulation instability that occurs in the single-pass configuration. In addition to the fact that the Turing instability features a power threshold and that it can arise in the normal GVD regime, the two processes showcase another fundamental difference regarding the dynamics in the temporal domain.

On the one hand, the single-pass configuration corresponds to a conservative system (provided that the linear losses can be neglected). In such system, the optical field can develop a periodic behaviour during its propagation known as the Fermi-Pasta-Ulam (FPU) recurrence, where photons are periodically exchanged from the pump field to the MI sidebands and vice-versa [106, 107].

On the other hand, the cavity configuration is intrisically dissipative due to the fact that a fraction of the intracavity power exits the cavity at each round-trip. This results in the fact that the growth of the initially weak modulation eventually saturates giving rise to a *temporal pattern* stable from one round-trip of the cavity to the next one. The period of the pattern is given by the Turing frequency which acts as an attractor of the dynamics [64]. Note that we have seen in the previous paragraph that stable modulated states are reached only for a limited range of parameters (especially in the normal dispersion regime, see Fig. 2.4).

To illustrate the generation of a stable Turing pattern, we performed a numerical simulation of the propagation of a cw field by integrating the LLE (2.1). At this point we emphasize that all the numerical simulations of wave propagation presented in this dissertation were performed using a *Runge-Kutta – Split-step Fourier* method. This method basically consists in solving the linear and nonlinear effects independently using Fourier transform in the spectral domain and a 4^{th} order Runge-Kutta scheme in the time domain. For this example we consider the monostable regime of a uniform cavity pumped in the anomalous region of GVD. The parameters correspond to those of Fig. 2.2(a-c). The initial cw intracavity field is set to the steady-state of the system ($P(z = 0) = 1\,\mathrm{W}$) and is perturbed by a weak harmonic seed at the Turing frequency $\omega_T/2\pi$. The intracavity field is saved after each round-trip and we display the evolution of the intracavity power for the first 200 round-trips in Fig. 2.5 as a surface plot. The initially weak modulation of the intracavity field progressively deepens as a consequence of the Turing (modulation) instability until a stationary modulated state is reached. This periodic structure then persists as long as the input field is sustained. Figure 2.5(b) shows the intracavity power initially (dashed blue line) and after 200 round-trips (solid red line). In the spectral domain (Fig. 2.5(c)), the initial field only contains two peaks at

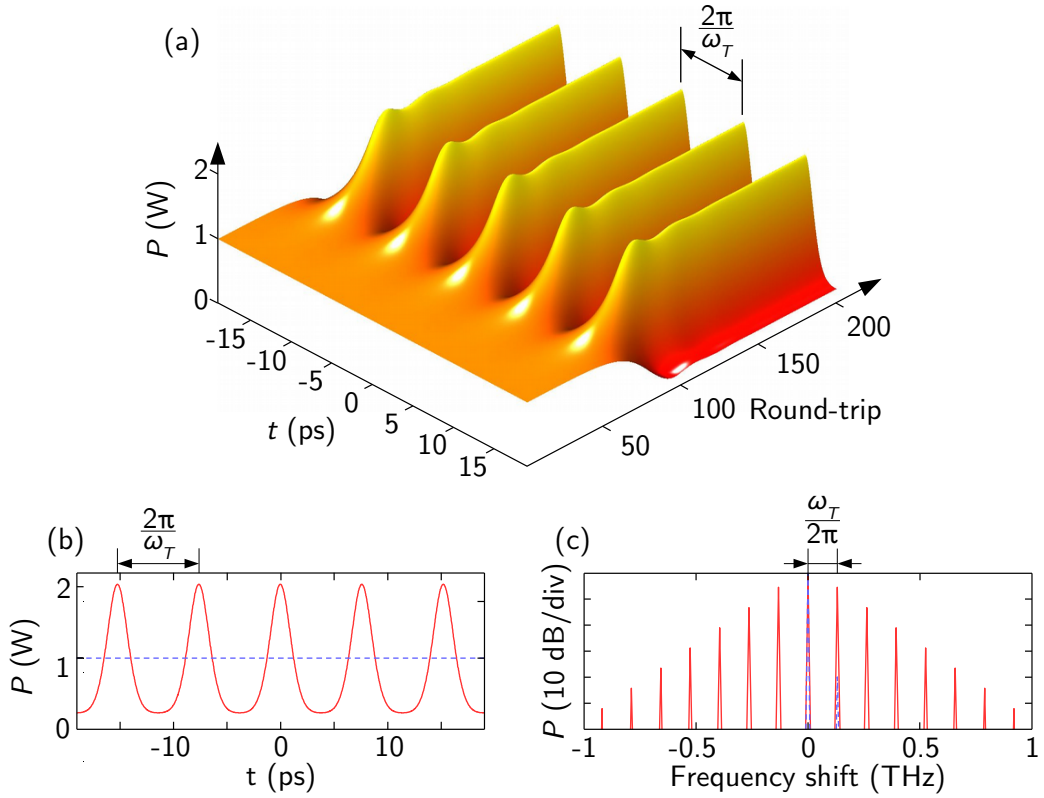

Figure 2.5 – (a) Evolution of the intracavity power in the time domain from the weakly perturbed steady-state to a stable Turing pattern. Optical intensity in both the (b) time domain and (c) spectral domain initially (dashed blue lines) and after 200 round-trips (solid red lines). $\gamma = 5\,/\mathrm{W/km}$, $L = 50\,\mathrm{m}$, $\alpha = 0.157$, $\theta = \sqrt{0.1}$, $\Delta = 1$ $\beta_2 = -20\,\mathrm{ps}^2/\mathrm{km}$, $P_{in} = 0.33\,\mathrm{W}$.

the pump frequency (null frequency shift) and the Turing frequency (positive frequency side) respectively. After 200 round-trips, the spectrum corresponding to the stable modulated state exhibits a large number of sidebands equally spaced at the fundamental frequency and its harmonics forming a triangular shape [108]. After the stable Turing state is reached, the intracavity field doesn't evolve anymore. It can be said that the system has reached a *P1* attractor in the sense that the field is reproduced identical to itself from one round-trip to the next one. This designation will be fully meaningful in Sec. 2.2.3. In this simulation, the Turing process is seeded by an harmonic perturbation. Corresponding experiments have been reported showing that the seeding of intracavity MI allows an extended control over the dynamics of the system [95]. In principle, the seeding wave does not even need to have the same polarisation state than the pump wave [66]. This process can also be triggered by random noise conditions in which case the periodic structures are often said to spontaneously emerge from a self-organization

process. In this configuration, each sideband develops as a consequence of the Turing instability. This is the configuration of the first experimental observation of "*periodic-intensity self-oscillation*" induced by MI in a fiber-ring cavity [62] and of most subsequent studies.

The similarity between the LL model and reaction-diffusion systems allowed to identify the Turing process as a universal mechanism of self-organization involved in numerous domains such as nonlinear optics, chemical reactions or biological systems [105, 109].

2.2 Longitudinally modulated dispersion - Turing and Faraday instabilities

In this section we extend the previous results to the case of *non-uniform* cavities. The study of these kinds of devices represents the most original part of the work reported in this dissertation. By *non-uniform* we mean that the parameters of the fiber-ring are not necessarily constant along the z coordinate. In our case we will focus our attention on cavities presenting a modulated dispersion profile but we point out that similar behaviours to those we will report can occur when considering variations of the nonlinearity [110] or the losses [111, 112]. Dispersion is a particularly interesting parameter to study because of the ease with which it can be tailored in optical fibers contrary to other parameters. We will see that a convenient way to tailor the dispersion profile of the cavity is to splice together pieces of uniform fibers with different dispersion values. This allowed us to confirm experimentally every peculiar feature of such modulated resonators described in this section. Chaps. 4 and 5 are by the way dedicated to the experimental investigations of these cavities.

2.2.1 Floquet analysis

We start by introducing a general mathematical form for the modulated dispersion profile [78, 79]:

$$\beta_2(z) = \beta_2^{av} + \beta_2^m f(z) \tag{2.9}$$

where β_2^{av} is the average dispersion, β_2^m the amplitude of the modulation and $f(z)$ is a periodic function of period Λ (and natural spatial frequency $k_g = 2\pi/\Lambda$) with zero average value and a minimum value of -1 for normalization (for example, $f(z) = \cos(k_g z)$). For consistency reasons, Λ can only take discrete values corresponding to fractions of the cavity length L: if $\Lambda = L$ the period of the dispersion corresponds to the length of the cavity, if $\Lambda = L/2$ the dispersion pattern equals half the length of the cavity and is thus

repeated twice over one round-trip... From there, we get back to the previous stability analysis to the point where the evolution of the perturbation in the Fourier domain is written as a system of two coupled ordinary differential equations recalled here for convenience:

$$\frac{d}{dz}\begin{pmatrix} \hat{u} \\ \\ \hat{v} \end{pmatrix} = \begin{pmatrix} -\dfrac{\alpha}{L} & -g(\omega,z) \\ \\ h(\omega,z) & -\dfrac{\alpha}{L} \end{pmatrix}\begin{pmatrix} \hat{u} \\ \\ \hat{v} \end{pmatrix} \tag{2.10}$$

where g and h are now z-periodic with period Λ due to the modulated GVD. To go further, it is useful to factorize the effect of the losses through the transformation $[\hat{u},\hat{v}] = [\tilde{u},\tilde{v}]\exp(-\alpha z/L)$. This done, the system of Eqs. (2.10) takes the form of a one degree of freedom Hamiltonian system regarding the $[\tilde{u},\tilde{v}]$ coordinates:

$$\frac{d}{dz}\begin{pmatrix} \tilde{u} \\ \\ \tilde{v} \end{pmatrix} = \begin{pmatrix} 0 & -g(\omega,z) \\ \\ h(\omega,z) & 0 \end{pmatrix}\begin{pmatrix} \tilde{u} \\ \\ \tilde{v} \end{pmatrix} \tag{2.11}$$

We can thus apply *Floquet theory* [37]. This amounts to study the evolution of the system over one period Λ to obtain the Floquet matrix Φ which is, in our case, a 2×2 real matrix defined by the conditions:

$$\begin{pmatrix} \tilde{u}(\Lambda) \\ \\ \tilde{v}(\Lambda) \end{pmatrix} = \Phi\begin{pmatrix} \tilde{u}(0) \\ \\ \tilde{v}(0) \end{pmatrix} \tag{2.12}$$

As a result, we can also write $[\tilde{u}(n\Lambda),\tilde{v}(n\Lambda)]^T = \Phi^n[\tilde{u}(0),\tilde{v}(0)]^T$. Note that the determinant of Φ is necessarily one, since it is obtained by integrating a Hamiltonian dynamics, which preserves phase space volume. Consequently, the two eigenvalues λ of Φ are constrained to lie either both on the unit circle, or both on the real axis. Only in that latter case can the system be unstable, the instability being associated with $|\lambda| > 1$ according to *Floquet theory*. Since the system (2.11) is not autonomous (due to the z-dependence of g and h), it cannot be solved analytically in general. However the Floquet analysis can provide informations on the stability of the system provided that the dispersion modulation β_2^m is "relatively" small. Importantly, this stability analysis holds valid regardless of the specific shape of the periodic function $f(z)$.

Let's start from the limit of uniform dispersion (i.e. $\beta_2^m = 0,\ \beta_2(z) = \beta_2^{av} \rightarrow g = g_{av},\ h = h_{av}$). The system (2.11) then reduces to a simple second-order equation that is straightforwardly integrated. The Floquet matrix is then given by:

$$\Phi_{av} = \begin{pmatrix} \cos(k_{av}\Lambda) & -\frac{g_{av}}{k_{av}}\sin(k_{av}\Lambda) \\ \frac{k_{av}}{g_{av}}\sin(k_{av}\Lambda) & \cos(k_{av}\Lambda) \end{pmatrix} \tag{2.13}$$

where we recall that $k_{av} = \sqrt{g_{av}h_{av}}$. The eigenvalues of Φ_{av} can be easily computed as:

$$\lambda_{av}^{\pm} = \mathrm{e}^{\pm ik_{av}\Lambda} \tag{2.14}$$

This result is consistent with the previous analysis, i.e. if k_{av} is imaginary for a range of frequency, Turing instability can arise. Now we can ask ourselves what happens when the dispersion is modulated. The system (2.11) becomes non-autonomous and it is hence no longer possible, in general, to give a simple closed form expression of the eigenvalues. However, we can assume that, for a sufficiently small value of β_2^m, the eigenvalues $\lambda^{\pm}$ of the Floquet matrix Φ remain close to the eigenvalues $\lambda_{av}^{\pm}$ of the uniform case. Two distinct cases appear:

• **Off-resonance** $k_{av} \neq \frac{m\pi}{\Lambda}$. Since $k_{av}\Lambda \neq m\pi$, it follows from Eq. (2.14) that the two eigenvalues are distinct and complex conjugate ($\lambda_{av}^{+} = (\lambda_{av}^{-})^*$). They both lie on the unit circle, away from the real axis. Under the perturbation induced by switching on the dispersion modulation they are slightly modified but are forced to stay on the unit circle because the system is still Hamiltonian (consequence of Liouville's phase space theorem [113]). This case is schematically described in the left panel of Fig. 2.6. In this situation, $|\lambda^{\pm}|$ cannot exceed 1 and the system stays linearly stable. Note that this conclusion still does not depend on the exact form of $f(z)$.

• **On-resonance** $k_{av} = \frac{m\pi}{\Lambda}$. It follows from Eq. (2.14) that Φ_{av} has a doubly degenerate eigenvalue $\lambda_{av}^{+} = \lambda_{av}^{-} = \pm 1$ (The upper or lower sign holds for m even or odd respectively). Under a small perturbation (dispersion modulation) the degeneracy can be lifted and two real eigenvalues can be created, one smaller than 1 and the other bigger than 1 in absolute value. This latter entails the instability of the stationary state through the exponential growth of the perturbation. This situation is schematically described in the right panel of Fig. 2.6. In principle, under very peculiar perturbations, the eigenvalues might also move along the unit circle implying that the system remains stable. However, for all the forms of perturbation tested (sinusoidal, square function, triangle, comb, see Fig. 2.8 on p. 45), it is not the case and the system destabilizes under an arbitrarily small perturbation.

To summarize, when the modulation of the dispersion is switched on, the system can become unstable under the resonant condition $k_{av} = \frac{m\pi}{\Lambda}$. By recalling the expression

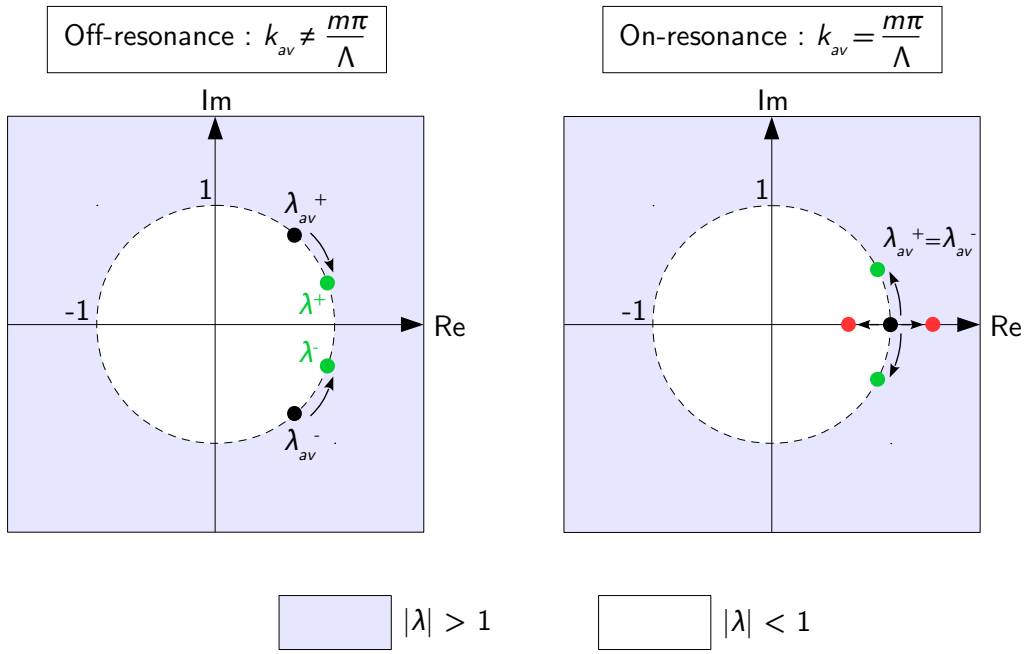

Figure 2.6 – Schematic illustration of the effect of dispersion modulation on the eigenvalues of the Floquet matrix (2.13). Black dots correspond to the unperturbed eigenvalues lying on the unit circle (dashed line). Coloured dots show the new positions of the eigenvalues when the perturbation is switched on. The left panel depicts the *off-resonant case* and the right one the *on-resonant case* which features an unstable eigenvalue in red outside the unit circle.

of $k_{av}(\omega)$ from Eq. (2.5), it is straightforward to show that the m^{th}-order resonance corresponds to the angular frequency $\omega = \omega_{F,m}$, with

$$\omega_{F,m} = \sqrt{\left\{\frac{2}{\beta_2^{av}}\left(\frac{\delta_0}{L} - 2\gamma P_s\right)\right\} \pm \left[\frac{2}{\beta_2^{av}}\sqrt{\left(\frac{m\pi}{\Lambda}\right)^2 + (\gamma P_s)^2}\right]} \tag{2.15}$$

In this expression, it is possible to recognize the contribution of the periodic modulation of the dispersion between square brackets. It should be emphasized that the resonance condition is linked to the natural spatial frequency of the dispersion profile through:

$$k_{av}(\omega_{F,m}) = m\frac{\pi}{\Lambda} = m\frac{k_g}{2} \tag{2.16}$$

This corresponds to the *parametric resonance condition*, that is to say that *the natural spatial frequency of the unperturbed harmonic oscillator (k_{av}) is equal to a multiple of half the forcing spatial frequency (π/Λ)*. This observation implies that the regime under which

the system destabilizes is a regime of *parametric modulation instability* or *parametric MI*. This kind of *parametric instability* has been reported first by Michael Faraday in his seminal work of 1831 [114]. Accordingly, we will call *Faraday instability* the process that entails modulation instability of the steady-state of the cavity by means of the periodic forcing induced by the modulation of the dispersion. Analogues of the hydrodynamical Faraday instability have been investigated in various domains such as Bose-Einstein condensates [115, 116], multimode lasers [117], and more recently, fiber resonators with periodically varying nonlinearity [110]. Importantly in our case, the Faraday process is not incompatible with the Turing process described in the previous section that occurs in uniform ring cavities as we will see later. Note that in the case of extended systems exhibiting spatial pattern formation, the role of ω and k are interchanged, and one can say that, under a forcing of the system at frequency ω_d, the system develops a parametric modulation instability characterized by wavenumbers k_m selected through the dispersion relation $\omega = \omega(k)$ in such way that the resonance conditions $\omega(k_m) = m\omega_d/2$ are fulfilled.

Now that we identified the conditions under which the modulation of the dispersion might induce parametric MI, we return to the original (damped) system described by the perturbations $[\hat{u}, \hat{v}]$. The overall Floquet matrix now reads $\Psi_{av} = \exp(-\alpha\Lambda/L)\,\Phi_{av}$ whose eigenvalues are given by:

$$\sigma_{av}^{\pm} = \mathrm{e}^{-\alpha\Lambda/L}\lambda_{av}^{\pm} = \mathrm{e}^{(-\alpha/L \pm i k_{av})\Lambda} \tag{2.17}$$

That means that the unperturbed eigenvalues now lie in the complex plane either on a circle of radius $\exp(-\alpha\Lambda/L) < 1$ (*Off-resonance*) or are degenerate and $\sigma_{av}^{+} = \sigma_{av}^{-} = \pm\exp(-\alpha\Lambda/L)$ (*On-resonance*). The instability still sets in under *on-resonant* conditions, but now, the perturbation can only grow if the amplitude of the modulation of the dispersion β_2^m is sufficiently large to push one of the eigenvalues outside the unit circle. In other words, there is a threshold on β_2^m for the onset of the parametric instability. Of course, the lower the losses, the closer the unperturbed eigenvalues are from the unit circle. Accordingly, the threshold increases with the losses. On the same note, for a fixed β_2^m (fixed dispersion profile), there is power threshold for the parametric MI to arise. The value of the threshold is, a priori, different for each resonance condition and depends on the losses but also on the specific profile of the dispersion. It is thus not possible to give a general analytical formula for this threshold. Each unstable frequency can lead to parametric MI with growth rate, or gain $G(\omega)$ which reads

$$G(\omega) = \frac{\ln(\max|\sigma^{\pm}|)}{\Lambda} \tag{2.18}$$

With all these elements, it is possible to compute the gain spectrum for any intracavity dispersion profile. To do so, the system of Eqs. (2.10) is integrated over the

length Λ for two independent sets of initial conditions. Then the values of $\sigma^{\pm}$ can be computed as the eigenvalues of the result matrix. In order to give a first insight into the role of dispersion modulation on the emergence of Faraday instabilities in passive fiber-ring cavities, we consider in Fig. 2.7 a cavity with a cosinusoidal profile of dispersion ($\beta_2(z) = \beta_2^{av} - \beta_2^m \cos(2\pi z/\Lambda)$) with an average normal GVD. All parameters are the same as in Fig. 2.3 except that the dispersion now varies longitudinally inside the resonator with a period Λ that equals the cavity length. β_2^{av} is identical to the uniform dispersion β_2 used in Fig. 2.3. The dispersion map of the resonator is given in Fig. 2.7(a) as a color plot along with its longitudinal evolution over one round-trip. Note that the choice we make to fix the beginning and the end of the round-trip at the coupler is purely arbitrary. Indeed, the Floquet analysis will give the same results for different dispersion profiles if they only differ by the initial phase of the perturbation function $f(z)$. For instance, sinusoidal and cosinusoidal profiles are equivalent regarding Floquet analysis. The gain spectrum has been computed for the same range of perturbation frequency and intracavity power as in Fig. 2.3 and the result is plotted in Fig. 2.7(c). The Turing branch around null frequency is still present and identical to the case of uniform dispersion. This means that the *Turing instability* is preserved despite the modulation of the dispersion and, importantly, that it is *solely driven by the average parameters of the cavity*. The non-uniform longitudinal dispersion profile induces the generation of new branches of parametric MI on the intermediate and upper branches of the bistable response of the cavity. Each of these branches (also called *Arnold tongues* [118]) corresponds to a resonance condition and its position is determined by Eq. (2.15) with the integer m associated to the successive sidebands (see the dashed lines on one side and the labels in Fig. 2.7(c)). Note that, in this particular configuration, the threshold for the Faraday sidebands (tips of the tongues) lies in the intermediate (cw unstable) domain. Higher losses would raise these thresholds while with lower losses, the sidebands would eventually arise on the lower branch of the bistable curve.

The situation described here is particularly interesting because Turing and Faraday instabilities arise in two distinct operating regimes that we could call *low power* and *high power* respectively. It is not the case, for instance, in the average anomalous GVD regime where the Turing instability appears on the upper branch too. This situation is illustrated in Fig. 2.7(d) where we can see that the pair of Turing sidebands has a much higher gain than any of the Faraday sidebands. In that case, the dynamics of the system is ruled by the Turing instability and the Faraday sidebands are not likely to be observed. For this reason, we focussed on the case of normal average dispersion where the two instabilities can be independently excited.

We previously noted the fact that, due to non-zero losses, each Faraday sideband appears beyond a threshold in power and amplitude of the modulation of the dispersion

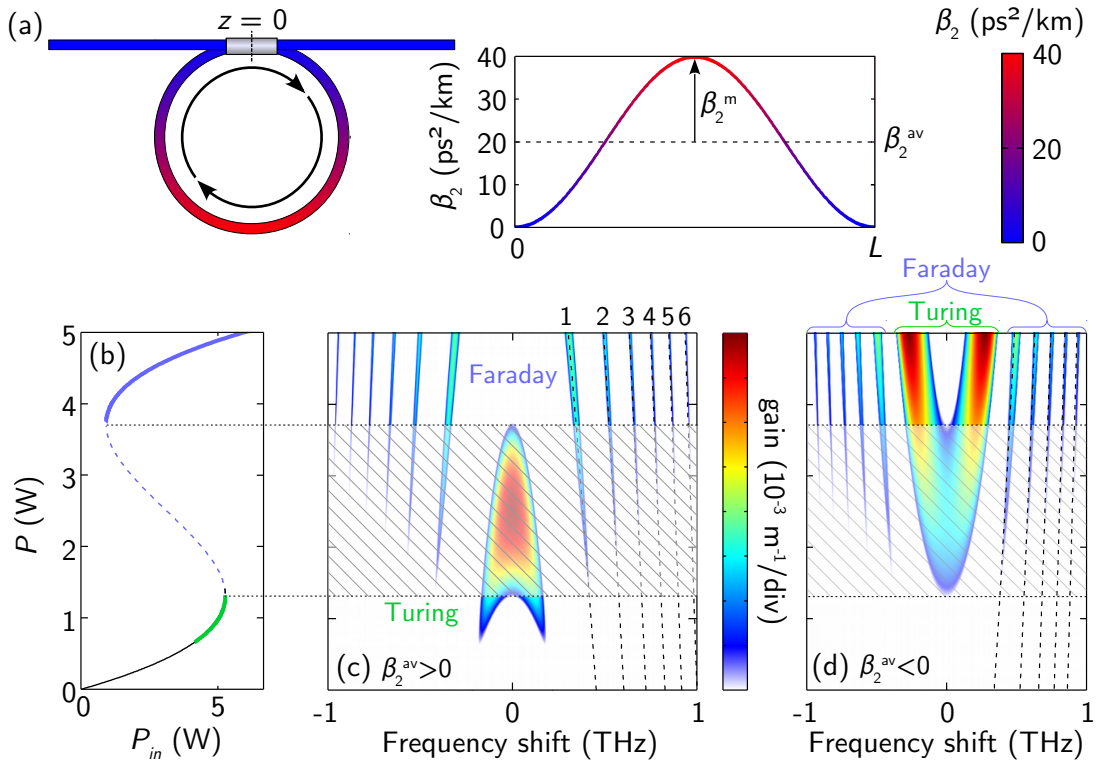

Figure 2.7 – Gain spectrum mapping for a cavity with sinusoidally varying dispersion in the bistable regime. The longitudinal dispersion profile is depicted in (a). (b) Cavity response curve for $\Delta = 6$. (c) ((d) respectively) shows a 2D color plot of the gain spectrum in the average normal (anomalous) GVD regime with the maximum gain positions calculated with Eq. (2.15) for $m = 1, 2, ..., 6$. $\gamma = 5\,/\text{W/km}$, $\Lambda = L = 50\,\text{m}$, $\alpha = 0.157$, $\beta_2^{av} = +(-)20\,\text{ps}^2/\text{km}$, $\beta_2^m = 20\,\text{ps}^2/\text{km}$.

(β_2^m). We also emphasized that a closed analytical formulation of these thresholds cannot be derived in general since they depend on the exact expression of the perturbation function $f(z)$. To illustrate this, we present in Fig. 2.8 numerical simulations of the parametric gain spectrum as a function of β_2^m, for four different modulation formats. We keep the condition $\Lambda = L$ and look at the system operating on the upper branch in the bistable regime with average normal GVD. This way, we ensure that only Faraday instabilities might occur as we previously determined. The results are plotted in Fig. 2.8 with the corresponding modulation format sketched in the bottom right corner of each of the four panels. We verify that the position of the instability sidebands is the same for all the formats tested and does not depend on modulation depth. Indeed, neither the exact shape of $f(z)$ nor β_2^m appear in the expression of the Faraday frequencies, only the period Λ and the average value of the dispersion β_2^{av} intervene. It is interesting to point out that the same remarks apply in the case where MI takes place in the single-pass

configuration in the average normal dispersion regime of DOFs, except for the presence of a power threshold for each sideband which is specific of the cavity configuration. For instance, several shapes of dispersion modulation have been tested in DOFs and led to similar instability spectra [41, 46] and dependence on β_2^m and β_2^{av} [42, 52]. We note, however, that significant differences in the threshold and maximum gain of each tongue are observed from one panel to the other. On the left side, the sinusoidal and triangle modulations give nearly similar gain mapping as it could be expected from the similarity between these two formats. On the right side, we compare two square modulations with different duty cycles.

Several interesting conclusions can be drawn here. First, we verify that each sideband for each modulation format is characterized by a specific threshold in β_2^m. Second, the evolution of the gain of each sideband is not monotonous with β_2^m. Indeed, the instability tongues can close-up and open-up again as β_2^m increases as it clearly appears in the case of sinusoidal modulation in the upper left panel. The above remarks also apply in terms of intracavity power P instead of β_2^m. It is necessary to recall here that the gain calculations do not take into account wave-mixing between the different instability sidebands which is likely to occur when the powers involved are important. Accordingly, the results from the Floquet analysis are exact only in the vicinity of the tips of the instability tongues. In Chap. 5, we specifically address numerically and experimentally the dynamical behaviour of the system in the case where multiple Faraday sidebands are generated and interact with each others.

2.2.2 Piecewise constant dispersion

A peculiar format of dispersion modulation where the Floquet analysis can be performed analytically without any additional approximation is the *piecewise constant* (or *step-like*) profile. This case is of particular interest because it can easily be implemented experimentally by splicing different pieces of uniform fibers together to form the ring cavity. We limit our study to the case where the resonator contains only two different fibers labelled a and b, characterized by their GVD coefficients β_2^a and β_2^b respectively (considering more pieces would essentially leads to heavier calculations without providing more insight). We assume here that all other parameters are identical for the two fibers, in particular their nonlinear coefficient ($\gamma^a = \gamma^b$). This is a reasonable and realistic assumption as we will see later. The dispersion pattern is composed of a length Λ_a of fiber a and Λ_b of fiber b such that $\Lambda = \Lambda_a + \Lambda_b$ (note that Λ_a and Λ_b are not necessarily equal). The total length of the ring is still L so that the dispersion pattern is concatenated L/Λ times over one round-trip. As we previously demonstrated, the behaviour of the cavity depends crucially on the average dispersion which, in this case reads $\beta_2^{av} = (\beta_2^a\Lambda_a + \beta_2^b\Lambda_b)/\Lambda$. The

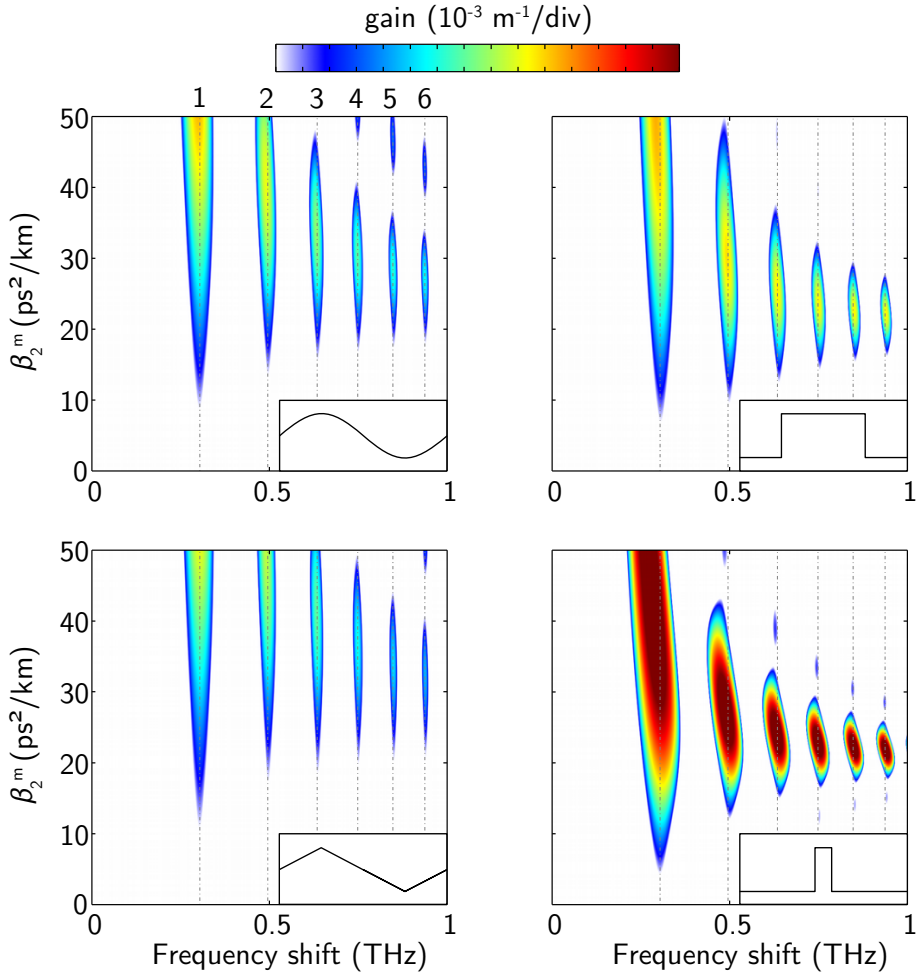

Figure 2.8 – Gain spectrum mapping as a function of the modulation depth of the dispersion for different modulation formats (sine, triangle, square functions). The position of each sideband calculated from Eq. (2.15) is superimposed in dashed-dot lines. $\beta_2^{av} = 20\,\mathrm{ps}^2/\mathrm{km}$, $L = 50\,\mathrm{m}$, $\mathcal{F} = 20$, $\Delta = 6$, $\gamma = 5\,/\mathrm{W/km}$, $P = 5\,\mathrm{W}$ (upper branch of the bistable curve).

Floquet map describing the evolution of the pertubations $[\hat{u}, \hat{v}]$ over one period Λ is, in this case, given by:

$$\Psi = \mathrm{e}^{-\alpha\Lambda/L}\,\Phi_a\Phi_b \tag{2.19}$$

where $\Phi_{a,b}$ are the Floquet matrix associated to the two uniform sections. Their expression has been derived previously (Eq. (2.13)). Ψ can be calculated analytically and its eigenvalues read:

$$\sigma^{\pm} = \frac{D}{2} \pm \sqrt{\frac{D^2}{4} - \mathrm{e}^{-2\alpha\Lambda/L}} \tag{2.20}$$

where

$$D = \mathrm{e}^{-\alpha\Lambda/L}\left[2\cos(k_a L_a)\cos(k_b L_b) - \frac{g_a h_b + g_b h_a}{k_a k_b}\sin(k_a L_a)\sin(k_b L_b)\right] \tag{2.21}$$

Parametric MI sets in if $|\sigma^{\pm}| > 1$ with gain $G(\omega) = \ln(\max|\sigma^{\pm}|)/\Lambda$ (Eq. (2.18)). From this, the gain spectrum can be analytically calculated.

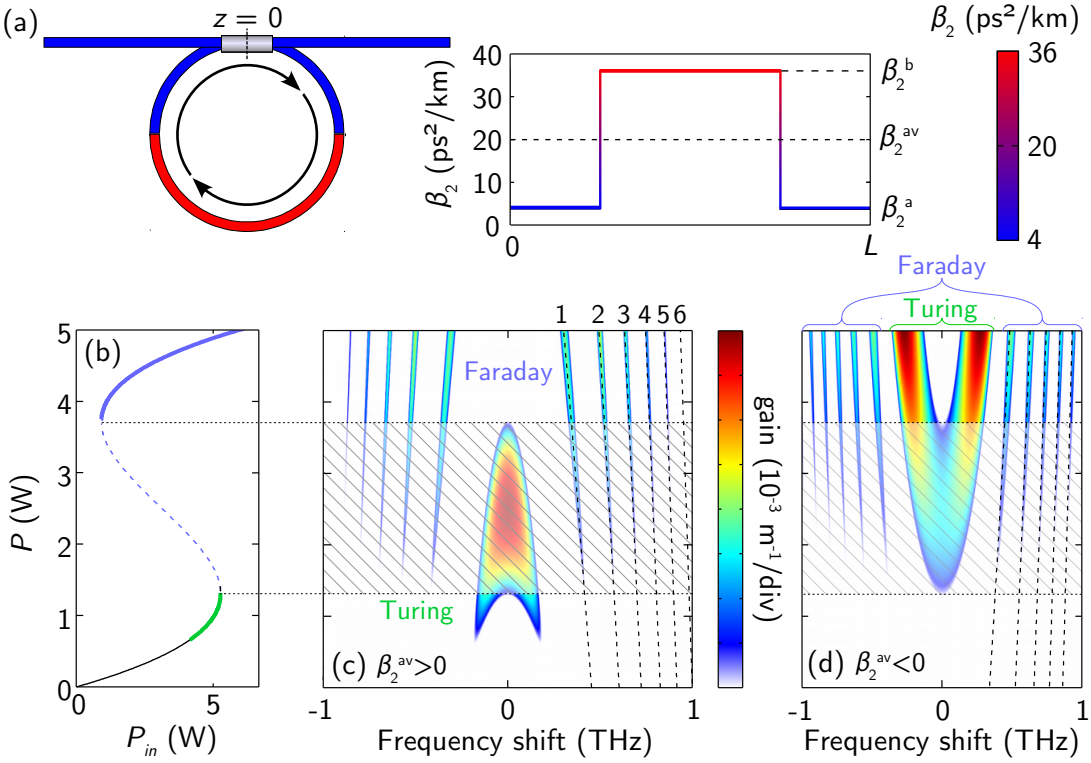

Figure 2.9 – Gain spectrum mapping for a cavity with piecewise constant dispersion in the bistable regime. The longitudinal dispersion profile is depicted in (a). (b) Cavity response curve for $\Delta = 6$. (c) ((d) respectively) shows a 2D color plot of the gain in the average normal (anomalous) GVD regime with the maximum gain positions calculated with Eq. (2.15) for $m = 1, 2, ..., 6$. $\gamma = 5\,\mathrm{/W/km}$, $\Lambda = L = 50\,\mathrm{m}$, $\alpha = 0.157$, $\beta_2^{av} = +(-)20\,\mathrm{ps^2/km}$, $\beta_2^a = +(-)4\,\mathrm{ps^2/km}$, , $\beta_2^b = +(-)36\,\mathrm{ps^2/km}$

As an illustration, we consider in Fig. 2.9 a piecewise constant cavity in the same operating conditions as in Fig. 2.7. The dispersion profile described in Fig. 2.9(a) shows that the cavity is composed of two sections of equal length $\Lambda_a = \Lambda_b$ and exhibits a normal GVD. The gain spectrum as a function of the intracavity power is plotted in Fig. 2.9(c) when the cavity operates in the bistable regime (see Fig. 2.9(b)). In a fashion very similar to Fig. 2.7(c), multiple instability tongues appear on the intermediate and upper branch due to the modulation of the dispersion. These two figures differ from each other

only by the threshold and gain of the instability sidebands as we previously discussed in Fig. 2.8. For informative purpose, we display in Fig. 2.9(d) the same gain mapping but in the average anomalous GVD regime. The conclusion is, in all aspects, similar to the case of Fig. 2.7(d).

The experimental part of this dissertation exclusively deals with such piecewise constant cavities because of their ease of implementation. However, we have seen that the behaviour of non-uniform cavities with respect to Turing and Faraday instabilities is essentially the same regardless of the precise shape of the dispersion profile. We can thus focus on the case of piecewise constant cavities without loss of generality.

2.2.3 The period-one and period-doubling regimes

Similarly to the Turing mechanism, the Faraday mechanism can entail the destabilization of a homogeneous steady-state of the cavity by the growth of sidebands at the Faraday frequencies. Accordingly in the time domain, the homogeneous steady-state becomes modulated. After the stage of exponential growth, the Faraday instability can generate a stable train of pulses with a large and fixed contrast ratio. One of the peculiar aspect of the Faraday mechanism is that the cavity can stabilize over either a period-1 (*P1*) or period-2 (*P2*) attractor depending on the parameters. Different types of period-doubling instabilities were proved to occur in devices subject to a delayed feedback: In a seminal paper, Ikeda predicted that the cw solution associated to the *cavity boundary condition equation* might trigger a period-doubling cascade leading to chaos [54, 55]. This phenomenon, now referred to as "*Ikeda instability*" has led to a tremendous amount of theoretical and experimental studies. Coen *et al.* have demonstrated that MI could appear under antiresonant conditions (not to be confused with *off-resonant conditions*) and that it is also associated with a *P2* dynamical behaviour [67, 93]. In this subsection we put the light on this phenomenon associated to the Faraday instability.

We propose an explanation for the emergence of these two regimes by considering that the dynamics of the system is solely driven by a single parametric instability tongue. It is important to recall that the parametric MI sets in under *on-resonant* conditions which implies that the eigenvalue of the unperturbed Floquet matrix is doubly degenerated and lies on the real axis (see p. 39).

• For m even, the eigenvalue is positive and when the instability arises, the amplitude of the Faraday sideband grows until it reaches a steady-state. The wave is shifted by a multiple of 2π at each period of the dispersion such that no particular feature is observed. Instability arising within this condition corresponds to the *P1* regime.

• For m odd, the eigenvalue is negative. Again, when the instability arises the amplitude of the Faraday sideband grows but, contrary to the previous case, the wave

undergoes a π phase shift at each period of the dispersion Λ. Accordingly, when the stable modulated state is reached, the pulse train is actually out-of-phase from one period to the next one such that it is reproduced identically after two periods. Now the outcome is different whether the ring cavity consists in an even or odd number of dispersion patterns: If the cavity contains an even number of patterns, then the phase shift over one round-trip is always a multiple of 2π and the output of the cavity exhibits a *P1* dynamics. If the cavity contains an odd number of patterns, the overall phase shift during a round-trip is π and the output of the cavity exhibits a period doubling dynamics (*P2* regime).

The above discussion is summarized in Table 2.1.

		L/Λ	
		even	odd
m	even	P1	
	odd	**P1**	**P2**

Table 2.1 – Summary of the conditions under which the Faraday instability exhibits a *P1* or *P2* dynamics.

We verified the above scenarios by numerical simulations of the LLE in the noise-driven configuration and we present in Figs. 2.10 and 2.11 some significant results illustrating the *P2* and *P1* regimes.

Let's first consider the case where the fiber-ring cavity contains a single dispersion pattern ($L/\Lambda = 1$) as illustrated in Fig. 2.10(a). We determined a set of parameters for which the threshold for the first Faraday sideband ($m = 1$) lies on the upper branch of the bistable curve and is lower than the one of higher order sidebands. This way, we can set the system in a state where the dynamics is dictated by this single sideband. The corresponding gain mapping is displayed in Fig. 2.10(b) and the parameters are given in the caption. This 2D color plot shows two Faraday sidebands corresponding to $m = 1$ and 2 on the upper branch. Just above the threshold for the first sideband the system is thus expected to manifest a period-doubling dynamics according to Table 2.1. Results from the numerical simulations are plotted in Fig. 2.10(c-e) for 10 round-trips when the system reached a stable state. We associate the color red (blue) to even (odd) round-trips. The temporal profiles plotted in Fig. 2.10(c) indeed shows that the stable state consists in a pulse train that is out-of-phase from one round-trip to the other which is symptomatic of the *P2* regime. Accordingly, the power recorded at the time $t = 0$ in the frame travelling at group velocity varies periodically with period $2L$ (see Fig. 2.10(d)). In the complex plane (Fig. 2.10(e)), the field at $t = 0$ describes a periodic orbit with the

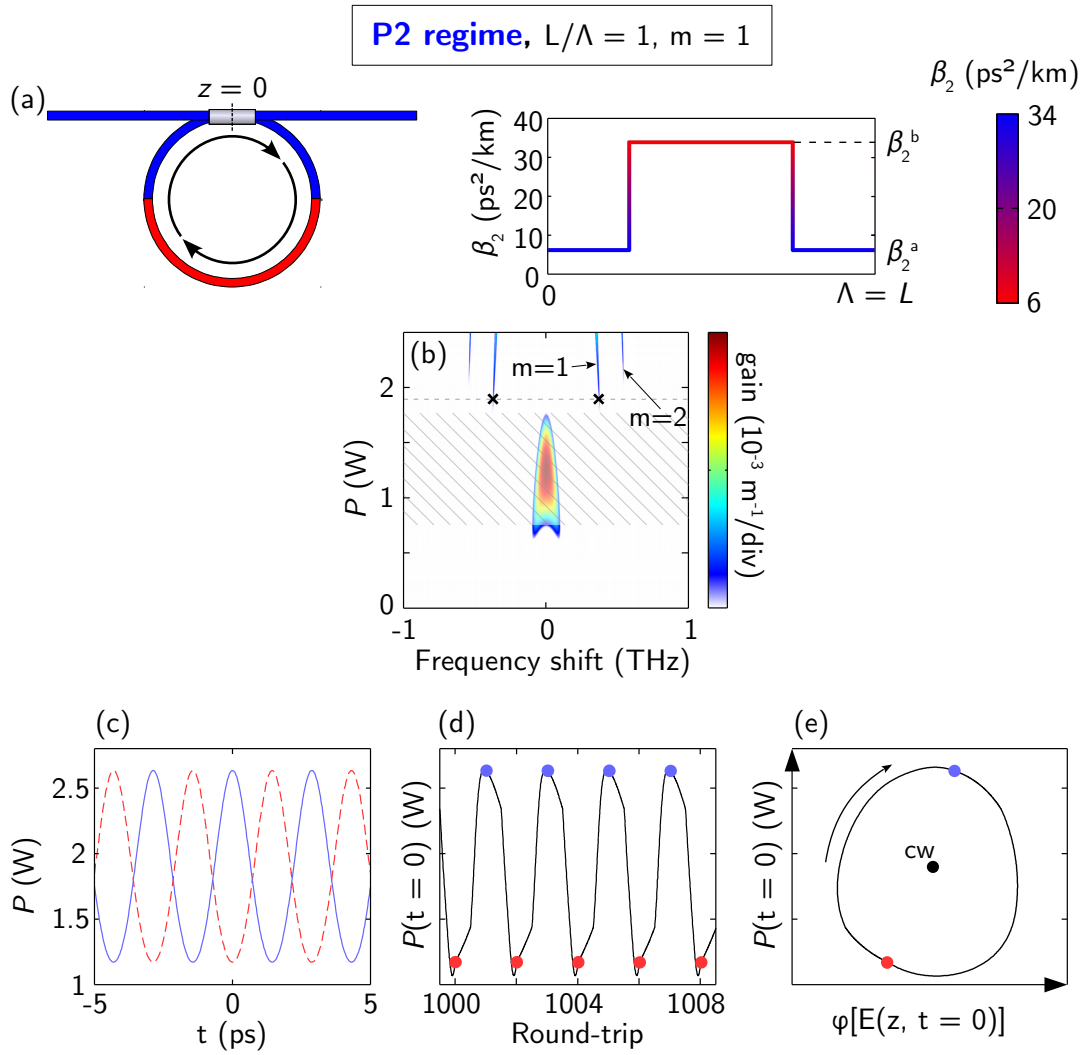

Figure 2.10 – Faraday instability in the P2 regime. (a) Dispersion profile of the cavity. (b) Gain spectrum mapping as a function of the intracavity power. Evolution for 10 consecutive round-trips of (c) the temporal periodic pattern, (d) the power at $t = 0$, (e) the field at $t = 0$ in the complex plane. Even (odd) round-trips are associated to red (blue) dots and lines. $\gamma = 5$ /W/km, $\Lambda = L = 50$ m, $\alpha = 0.157$, $\Delta = 3$, $P_{in} = 0.47$ W.

same period. The initial cw field is represented by a black dot and is labelled "cw". Note that the transient evolution of the field from cw to periodic pattern is reflected in the complex plane by a spiraling trajectory that is not shown here for clarity.

We performed the same simulation by dividing the length of the dispersion pattern by two while keeping the length of the cavity fixed. In other words, the cavity is now composed of the dispersion pattern concatenated twice ($L/\Lambda = 2$) as illustrated in Fig. 2.11(a). The gain mapping calculation shows again two sidebands on the upper branch but for higher frequency shifts. For the same power, the dynamics of the cavity is still

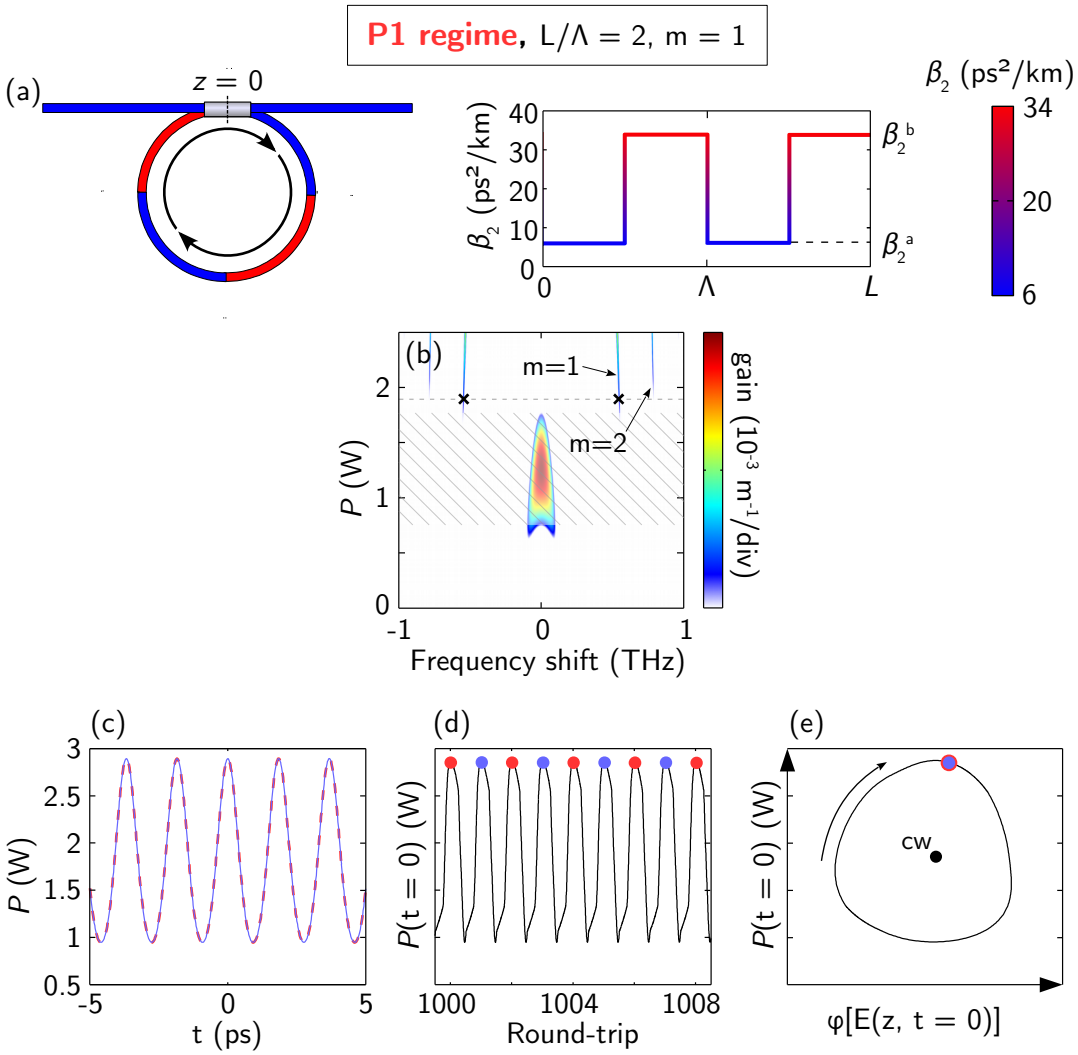

Figure 2.11 – Same as Fig. 2.10 in the P1 regime. $\Lambda = L/2 = 25\,\mathrm{m}$.

driven by the sideband $m = 1$ (Fig. 2.11(b)). Now according to our previous discussion summed up in Table 2.1, the Faraday instability should manifest itself as a *P1* instability. This is what appears from the results plotted in Fig. 2.11(c-e). Contrary to the previous case, the resulting pulse train is repeated identically every round-trips (Fig. 2.11(c)). The power recorded at the time $t = 0$ in the frame travelling at group velocity takes a form similar to the previous case both in the time domain and the complex plane (Fig. 2.11(d) and (e) respectively) but now with period L.

Note that if, by changing the dispersion profile of the cavity, the threshold for the first sideband ($m = 1$) is superior to the one of the second sideband ($m = 2$) then the dynamics of the system would be ruled by this latter. In that case, owing to the fact that the system is governed by a resonance of even order, the Faraday instability would yield

a P1 dynamics regardless of the number of dispersion pattern composing the cavity (see the first line of Table 2.1).

At this point, the question as to what happens if the ratio L/Λ is large (i.e. if the cavity contains a large number of modulation periods) is legitimate. By comparing Figs. 2.10(b) and 2.11(b) one can notice that reducing the period of modulation with respect to the length of the cavity shifts the Faraday sidebands to higher frequencies. This is in agreement with the analytical predictions of Eq. (2.15). We verified by means of extensive calculations of the analytical gain spectrum that increasing the value of the ratio L/Λ essentially translates into this frequency up-shifting of the sidebands without strongly affecting their gain. This conclusion holds valid regardless of the shape of the dispersion modulation. As a consequence, we focussed all of our experimental investigations on the case of piecewise constant cavities with a single period of modulation, which encompass all the peculiar behaviour of dispersion oscillating cavities. Note that implementing a cavity with a large number of modulation periods can be achieved rather simply by using the same kind of dispersion oscillating fibers as the one used by Droques *et al.* in the single-pass configuration [41, 42].

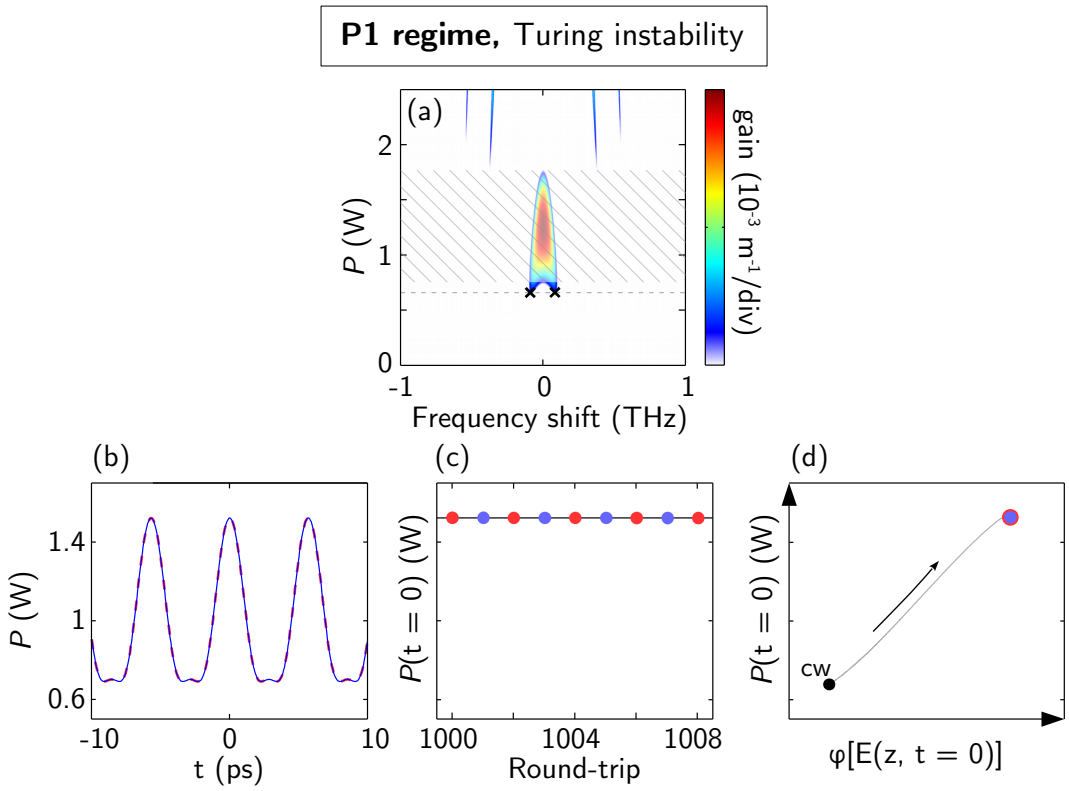

Figure 2.12 – Same presentation as Fig. 2.10 and 2.11 in the case of the Turing instability with the LL model (Eq. (1.21)). (d) The transient evolution of the field at $t = 0$ from cw to periodic pattern is given by the gray line.

For the sake of completeness, we address in Fig. 2.12 the case of the Turing instability that is preserved even when the dispersion inside the resonator is not uniform. As we mentioned earlier, this branch is governed by the average parameters of the cavity (β_2^{av} in our case) (p. 42), and triggers the formation of a pulse train stable from round-trip to round-trip (p. 36). The latter property allows us to state that the temporal dynamics associated with the Turing pattern is *P1*. However, it is different from the *P1* regime of the Faraday instability by the fact that once the stable modulated state is reached, the intracavity field remains stationary as it appears in Fig. 2.12(c). Hence, the trajectory of the system in its stable state in the complex plane doesn't describe an orbit any more but reduces to a single point (see Fig. 2.12(d)). Note however that this is only true in the context of the LL model. In practice, the field inside the cavity evolves periodically (with period L) when the stable state is reached because of the boundary conditions. This can be seen when integrating the full cavity map Eqs. (1.7) instead of the LL Eq. (1.21).

In Chap. 4, we will present experimental recordings of the pulse trains generated in a piecewise constant cavity by both the Turing (*P1*) and Faraday (*P2*) mechanisms confirming the results obtained in this subsection.

2.3 Summary

- We detailed the appearance of intracavity modulation instability in both anomalous and normal dispersion regimes thanks to the boundary conditions imposed by the cavity configuration. This has been associated to the well-known and ubiquitous *Turing instability*. We have seen that this instability triggers the generation of a stable train of pulses.

- We introduced the concept of modulated resonators and showed that these devices exhibit a new kind of instability. This phenomenon is identified as a parametric modulation instability similar to the also ubiquitous *Faraday instability*.

- We developed an analytical model to calculate the parametric gain associated to the Faraday instability for cavities with a piecewise constant dispersion profile. This configuration is used throughout the rest of the dissertation.

- The temporal dynamics of the stationary Faraday and Turing regimes has been investigated and compared emphasizing the existence of a period doubling regime.

“Have you tried turning it off and on again?”

— Roy Trenneman in *The IT Crowd*

CHAPTER 3

Implementation of a passive fiber-ring cavity

In this chapter, we focus on the experimental implementation of a passive fiber-ring cavity. First, we briefly discuss the main advantages of fiber-ring optical resonators, especially compared to microresonators. In the second section, we give a general overview of the device and its operation, focusing on two critical points: the input field, i.e. how the cavity is pumped and, in greater detail, how to control, fix and measure the linear phase accumulation, a parameter specific to the cavity configuration introduced in Chap. 1. The last section is devoted to the different detection and recording methods that we implemented in the experiments reported in this dissertation. These methods allowed us to access the spectral and temporal dynamics associated to the Turing and Faraday instabilities.

3.1 Why to study passive fiber-ring optical resonators?

The use of optical fiber as the propagation medium for the cavity offers several advantages when it comes to the implementation. In this brief section we make a non-exhaustive list of these points.

First it should be noted that the cavity itself actually accounts for a rather small fraction of the full setup which is all-fiber. Indeed, most of it is dedicated to the temporal shaping of the input field, the active stabilization of the cavity and the detection/recording stage, all of this being described in details in the following sections. Since all our experiments used a pump wavelength lying in the conventional telecommunication window (C-band, 1530 – 1565 nm), we mostly use telecom-compatible components (amplifiers, filters, couplers, ...) which are widely accessible and reasonably priced. These components also benefit from fairly low insertion losses.

Another aspect of fiber-ring cavities is the fact that their FSR is very low compared to microresonators'. Optical fiber cavities typically measure between 1 m [92] and a few hundred meters [71] which corresponds to FSRs roughly ranging from 200 MHz to 0.5 MHz. This should be compared to the FSR of microresonators which is typically of the order of a few tens of GHz up to a few hundred GHz [72]. For this reason, optical fiber cavities can be referred to as *macroresonators*. The key advantage of the low FSR of optical fiber cavities is that it makes them compliant with electronic devices (detectors, oscilloscopes), allowing real-time round-trip-to-round-trip monitoring and acquisitions of the output of the cavity. In the next chapters, we make use of this property to unveil the dynamics of the instabilities occurring in our system.

The typical scale of optical fiber cavities of the order of the meter also allows us a greater control over the longitudinal evolution of the parameters of the resonator. In our case, where we are interested in dispersion modulation, we can easily tailor the longitudinal profile of the dispersion along the ring's length by splicing together different pieces of fiber by means of a standard fusion splicer. The length of each fiber section can be increased/reduced afterwards without significantly increasing the intracavity losses thanks to the great efficiency of fusion splicers.

On the theoretical level, we reemphasize here that we exclusively use *single-mode fibers* which avoids having to consider any effect on the transverse plane. This way, the propagation of light inside the resonator reduces to a 1-D model which considerably facilitates the mathematical description of the system.

3.2 Driving and stabilizing the cavity

In this section we describe the functioning of our fiber cavity device, pointing out the constraints and limitations of the system. We focus here on the main part of the setup which is common to all the experiments presented in the following chapters, and we leave the description of the detection/recording methods to the next section. The main setup is based upon the scheme introduced by S. Coen *et al.* [67–69, 93] and is depicted in Fig. 3.1.

The laser source is a 40 mW cw distributed feedback (DFB) module operating at 1550 nm, thermally tunable over a range of nearly 1 nm around this value. It also offers piezo tuning capabilities over a range of several picometers at frequencies up to 10 kHz. Importantly, the linewidth of the laser is specified to be less than 100 Hz which is at least 3 orders of magnitude narrower than the linewidth of the cavity resonances (which is no less than 100 kHz in our case). This is indeed fundamental because it implies that the coherence length of the laser is greater than $\mathcal{F}$ times the length of the cavity ($\mathcal{F}$ being the finesse the cavity) which is mandatory to ensure the coherent interaction between the input field and the recirculating field [101].

The laser is used to generate two separate beams both fulfilling a specific purpose:

- **The *pump beam*** is the one that will undergo nonlinear effects inside the resonator and is described in Sec. 3.2.1,
- **The *control beam*** is used to actively stabilize the optical path length (OPL) of the cavity in order to operate at fixed detuning. Its power is low compared to the pump beam and it thus does not experience nonlinear effects. It is detailed in Sec. 3.2.2.

Both beams are injected inside the cavity through the fiber coupler and circulate in opposite directions inside the resonator. One of the originality of our setup is the use of optical circulators in front of each of the two inputs of the coupler which allows us to use each port both as an input and output. Another way to allow this is to include a tap coupler inside the cavity which however increases the intracavity losses. Let's now detail the operation of each beam.

3.2.1 Generation of the driving field - The pump beam

In principle the input field can take two forms. It can be either continuous (cw) or consist in a periodic train of pulses. This choice of the pumping scheme actually deserves attention. Indeed, cw pumping is, in theory, the most pertinent choice as it is the hypothesis made in all analytical investigations of passive fiber-ring cavities, thus allowing

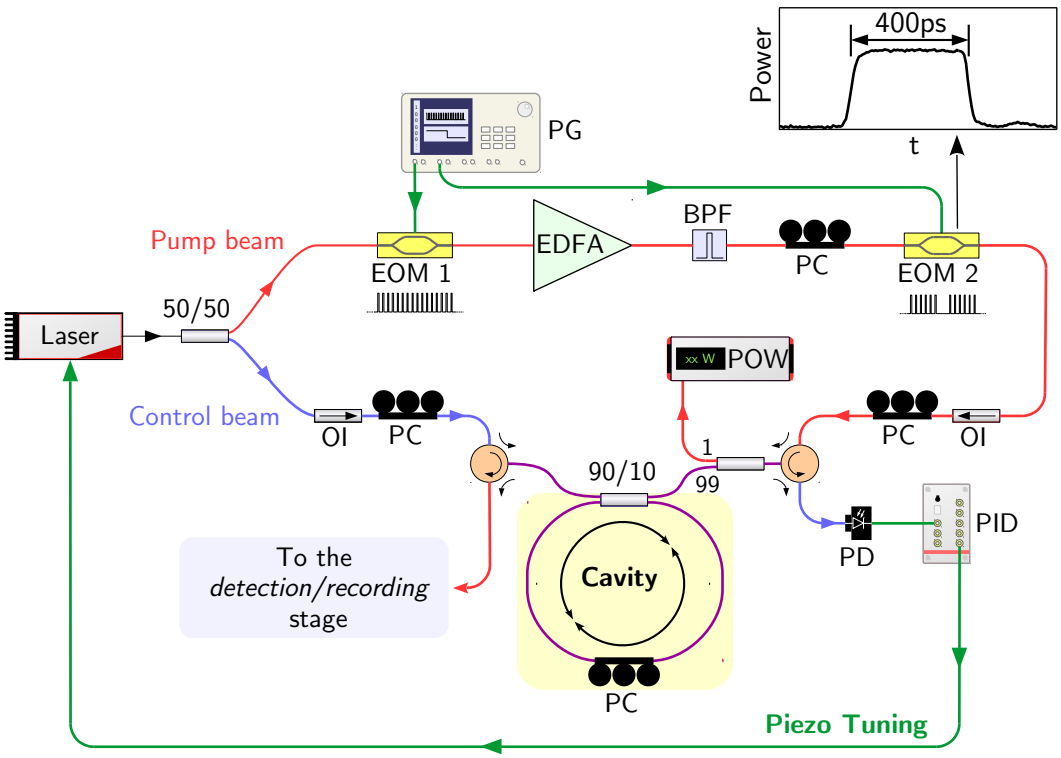

Figure 3.1 – Main setup for the experimental implementation of a fiber-ring cavity. Red, blue, and green lines are associated to the pump beam, the control beam, and electric connections respectively. Purple lines denote paths common to both beams. The temporal profile of an input pulse is given in the top right corner. EOM: electro-optic modulator, PG: pattern generator, EDFA: Erbium doped fiber amplifier, BPF: band-pass filter, PC: polarisation controller, OI: optical isolator, POW: powermeter, PD: photodetector, PID: proportional-integral-derivative controller.

direct comparison between experiments and predictions. But, as it has been thoroughly explained by S. Coen [93, 101], cw pumping suffers from two main technical limitations. The first one is that the power needed to observe the nonlinear processes we want to investigate is difficult to reach in the cw regime. Conversely, the use of a pulsed pump beam allows to reach large peak powers easily. The second drawback of cw pumping is the Brillouin scattering (BS). This nonlinear process (inelastic scattering) is responsible for a depletion of the pump through the generation of an acoustic wave and a backscattered optical wave. Above a particular pump power (often called Brillouin threshold), the process becomes stimulated (SBS) which causes a more efficient conversion of the pump wave to the backscattered wave. These two waves interfere resulting in a strong alteration of the pump wave which saturates [119]. For this reason, SBS is a detrimental effect in our system. The real issue of SBS is actually that its threshold is in general lower than the power involved in the instabilities we want to investigate, preventing us from

observing these latter. It is therefore fundamental for us to avoid SBS. To do so, several approaches have been proposed including phase modulating the pump field to reduce the Brillouin gain [119] or incorporating an optical isolator inside the cavity to hinder the buildup of the Stokes wave [60, 120]. This latter is not conceivable in our case since we want to keep the possibility of using the two propagation directions in the resonator (see Sec. 3.2.2). Another method to increase the SBS threshold in the cavity configuration has been demonstrated, involving a careful control of the cavity's length (with a sub-cm precision) but its efficiency drops for a cavity length exceeding a few meters [121]. In the end, the choice of a pulsed pump remains the most attractive. Indeed, threshold for SBS is raised to high power for pulse durations shorter than the lifetime of the acoustic phonon ($\approx 10\,\mathrm{ns}$) [119]. This duration still covers thousands of MI periods such that we can consider quasi-cw pumping operation. We have thus opted for a pulsed input beam which, nonetheless, induces the problem of the *cavity synchronization*. In fact, we will have to make sure that the pump repetition rate matches a multiple of the FSR such that each input pulse coherently interacts with the recirculating pulse. In fact, we show in Appendix A that a mismatch between these two quantities alters the behaviour of the cavity [88]. It is also of primary importance to minimize the background over which the input pulses sit as it could itself exceed the SBS intracavity power threshold. This latter reads [122]:

$$P_{SBS}^{th} = \frac{2A_{eff}\alpha}{Kg_B L} \tag{3.1}$$

with the effective area of the transverse mode $A_{eff} = 80\,\mu\mathrm{m}^2$, the round-trip losses $\alpha \approx 0.15$ in our case, $K = 2/3$ for standard (non-PM) fibers [123], and the Brillouin gain $g_B \approx 5 \times 10^{-11}\,\mathrm{m/W}$ [84]. It appears that this threshold is inversely proportional to the length of the fiber loop so that one should preferably implement the shortest cavity possible. In the end, to obviate the occurence of SBS between the pump pulses, it is necessary to generate these latter with the highest possible extinction ratio.

In our setup depicted in Fig. 3.1, the pump beam is highlighted by the red path. The pulses are generated by means of an electro-optic modulator (EOM 1), which provides an extiction ratio in excess of 30 dB, driven by an electric pattern generator (PG). We used pulse durations ranging from 400 ps to 2 ns. An example of temporal profile is given as an inset in Fig. 3.1: we point out the remarkable flatness of the power over almost the entire duration of the pulse. The repetition rate of the pulse train is finely tunable via the PG with a precision of a few femtoseconds so that we can minimize the synchronization mismatch mentioned above. Note that in the original setup developed by S. Coen *et al.* this operation was realized thanks to a mechanical fiber stretcher embedded in the cavity. For specific purposes, we require a second modulator EOM 2 (which is polarization

maintaining (PM) hence the presence of the polarization controller (PC) upstream) to further control the shape of the input field. It has been used to generate bursts of pulses, two-levels patterns or ramps. Input pulses are amplified by one or two Erbium doped fiber amplifier(s) (EDFA) and filtered to remove the amplified spontaneous emission (ASE) in excess. Finally we added an optical isolator to avoid any reflection of light in the amplifying stage. The role of the PC at the end of this arm will appear in the next subsection. A 99/1 tap coupler is included in order to measure the power of the input pulses. The pump beam is partially coupled inside the cavity where it experiences the nonlinear effects we want to investigate. Then, light exiting the cavity by the left port is directed toward the detection/recording stage which is detailed in Sec. 3.3.

3.2.2 Stabilization and control of the detuning - The control beam

In Chap. 1, we have introduced the linear phase accumulation Φ_0 which is specific of the cavity configuration. We have seen in Chaps. 1 and 2 that its value drastically impacts both the linear and nonlinear behaviour of the resonator. It is therefore essential to control this parameter in order to get interpretable and reproducible results out of experimental investigations of the cavity. Fundamentally speaking, the phase accumulation accounts for the interferometric nature of the system. As a consequence of their relatively large size, the OPL of fiber resonators is naturally sensitive to external perturbations be they thermal or mechanical. For instance, thermal effects can cause an expansion of the silica that composes the fiber, whereas variations in the refractive index of the fiber can induce a phase sensitivity of nearly 30π /°C/m [124]. For most of our investigations, we want the phase accumulation, and consequently the detuning, to remain constant during the course of an experiment. This is done thanks to the control beam highlighted in blue in Fig. 3.1. It consists in a fraction of the output of the cw laser source directly injected into the cavity through the left port and circulating clockwise. The output is then directed toward a photodetector and a proportional-integral-derivative (PID) controller, which generates an error signal by comparing the output level of the control beam to a setpoint fixed by the experimenter. The error signal drives the piezo tuning of the pump wavelength with a refresh rate of 10 kHz. For a correct set of parameters addressed to the PID controller, the output level of the control beam is locked to the setpoint. Consequently, the linear phase is locked and we say that the cavity is *stabilized*. Equivalently, the linear phase can also be locked by adjusting the length of the cavity thanks to a piezo-electric fiber stretcher instead of the pump wavelength. This is the method originally implemented by S. Coen *et al.* [93].

Efficiency of the locking device

In order to quantify the efficiency of the locking system, we recorded during 30 s both the error signal and the output of the control beam when the locking device is on. From this latter we can retrieve the relative fluctuations of the OPL which is plotted in Fig. 3.2(a). By fitting this recording with a normal distribution (see Fig. 3.2(b)) we find a standard deviation of 2.7 nm which means that when the active stabilization is on, the OPL fluctuations don't exceed $\lambda_0/250$, which is satisfying. The evolution of the piezo voltage during those same 30 s shows how the PID system succeeds in compensating for environmental fluctuations and mechanical perturbations: the two arrows around 18 s and 25 s point out slight taps on the fiber spool, which do not interrupt the locking (Fig. 3.2(c)). From this recording and taking into account the length of the cavity (51.6 m) and the piezo tuning coefficient of the laser (0.125 pm/V), we can determine that when the locking is on, the pump frequency is actively tuned over a range that does not exceed 4 times the FSR. The maximum duration of the locking is strongly linked to the environment fluctuations, which eventually lead to a failure of the PID system. In this latter situation, the operating point is automatically recovered. Typically, the system can remain stable over 10 min which is confortable when it comes to performing recordings. To achieve such stability, efforts were made to isolate the cavity from thermal, mechanical and acoustical perturbations.

Determination of the detuning

The active stabilization device allows us to operate the cavity with a linear phase accumulation (and thus, detuning) that is fixed. It is important to note that since the pump and control beams originate from the same laser, there is no relative drift between the two beams. Accordingly, the linear phase accumulation seen by the pump beam is also locked. In this paragraph, we describe how the detuning δ_0 seen by the pump beam can be determined and tuned.

First, we point out that the transfer function of the cavity ($P_{out} = f(\delta_0)$) is obtained experimentally by recording the evolution of the output power while sweeping the pump wavelength. We verified that, in our case, a linear variation of the piezo voltage driving the laser induces a linear variation of the detuning. When linearly sweeping the detuning, we can observe at the control output of the cavity a set of equally spaced resonances. Naturally, the residual birefringence of the non PM fibers we use to build our cavities induces two orthogonal polarization eigenstates such that we have to consider the projection of the polarization state of the input field on the two polarization modes of the cavity. Each polarization eigenstate is associated to a set of cavity resonances, so that if the input field doesn't match one polarization state, two interlaced sets of

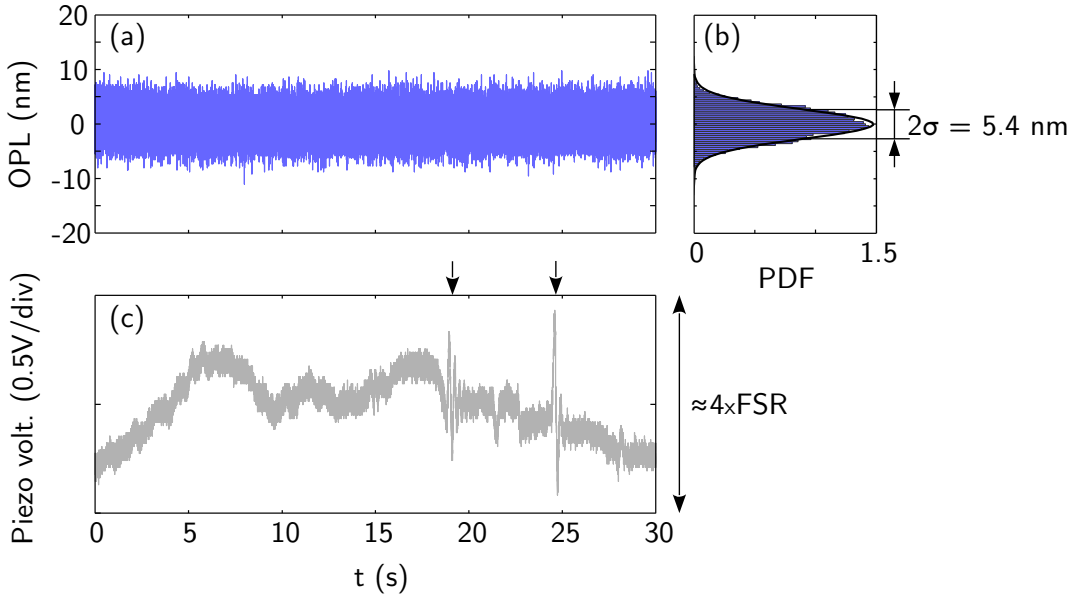

Figure 3.2 – Efficiency of the phase locking system. (a) Relative fluctuations of the optical path length of the cavity when the locking is on. (b) Corresponding normal distribution fit. (c) Evolution of the piezo voltage (error signal) for the same 30 s window. The response of the system to two artificial mechanical perturbations (slight taps on the fiber spool) is pointed out by arrows. $L = 51.6\,\mathrm{m}$, $\mathcal{F} = 18$, Piezo tuning of the pump wavelength: 0.125 pm/V.

resonances are observed at the output. In practice, one has to tune the polarization state of each beam thanks to the controllers placed before the cavity so that they each correspond to one eigenstate [93]. Once this is done, the polarization state of each beam can be preserved for several hours.

This done, the detuning of the pump beam can be determined by recording three consecutive resonances for both the control beam and the pump beam (in the linear regime). One example is proposed in Fig. 3.3. The x-axis can be mapped to the phase accumulation by noting that the distance between two consecutive resonances corresponds to a 2π shift. Taking the tip of a resonance of the pump beam as reference, the abscissa axis corresponds to the detuning δ_0. Then, pointing out the PID setpoint on the resonance of the control beam gives the value of the locked detuning. It then appears that the range over which the detuning can be set is limited to the width of the control resonance. Indeed, the locking device fails to operate aways from the resonances because of the flatness of the transfert function. Fortunately, the distance between the two sets of resonances, which depends on the optical path difference between the two eigenstates, can be modified thanks to the polarization controller included inside the cavity (see Fig. 3.1). This finally allows to operate the cavity with any value of

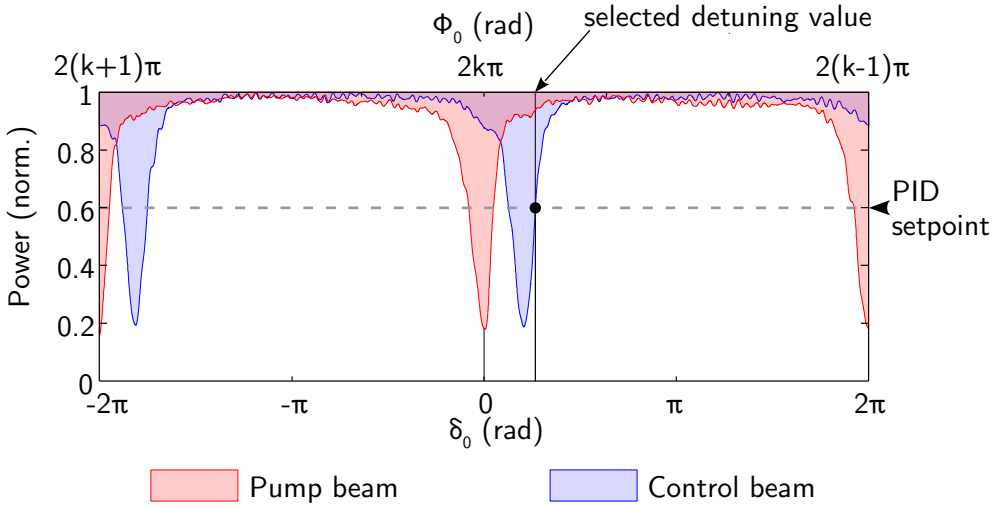

Figure 3.3 – Example of determination of the detuning in an experiment. $\mathcal{F} \approx 16$, $\delta_0 \approx 0.9\,\text{rad} \rightarrow \Delta \approx 4.4$.

the detuning. Note that since the intracavity polarization controller changes both the eigenvalues and eigenvectors of the polarization modes, the separation between the two sets of resonances has to be fixed before the polarization of each beam. In the example illustrated in Fig. 3.3, the system is locked on the positive slope of the resonance and the resulting detuning is estimated to be $\approx 0.9\,\text{rad}$ with a precision better than $0.05\,\text{rad}$. This precision increases with the steepness of the resonance, i.e. with the finesse of the cavity.

Modulation instability spectrum

Now that we exposed how the detuning parameter can be controlled, we describe briefly how it can affect the observation of modulation instability. We recorded the MI (Turing) spectrum in a uniform SMF-28 fiber-cavity with an optical signal analyser (OSA) (description in Sec. 3.3.1) in three distinct regimes that we labelled"*Unstabilized*", "*Scanning*", and "*Locked*". Results are gathered in Fig. 3.4 where the upper row shows both the intensity of the control output and the piezo voltage, and the lower row, the corresponding MI spectrum.

• **The *Unstabilized mode*** corresponds to the case where the locking device is *off*, i.e. no piezo tuning is applied to the laser source. The detuning "freely" evolves depending on the environmental fluctuations. The corresponding optical spectrum exhibits a series of random peaks evolving rapidly in time. This is due to the fact that, during the sweeping of the spectrum analyser, the system eventually crosses regions of parameters where MI occurs.

• **The *Scanning mode*** corresponds to the case where the pump wavelength is continuously swept across the resonances. This mode is of particular practical interest because it allows to rapidly check the cavity synchronization. Indeed, by scanning the detuning, we observe rather stable spectral components at wavelengths presenting MI gain and their harmonics, only if sufficient synchronization is achieved. By finely tuning the repetition rate of the pump pulses, one can maximize the amplitude of these bands, which guarantees a good cavity synchronization.

• **The *Locked mode*** corresponds to the case where the locking device is *on*, i.e. the detuning seen by the Pump beam is fixed. If all conditions are met (correct detuning, pump power, synchronization, polarization states, ...), the pump, the MI sidebands, and the harmonics appear in the spectrum as a series of sharp peaks arranged in a triangular shape [108]. Fig. 3.4(f) shows a typical experimental recording of a MI spectrum with a stabilized detuning.

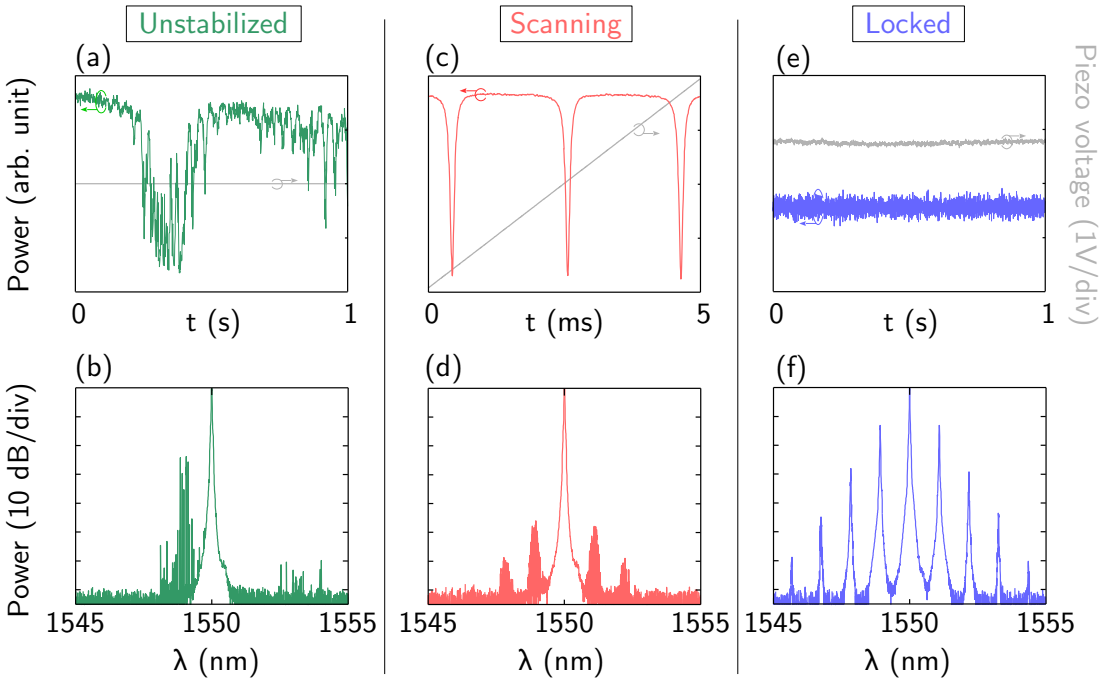

Figure 3.4 – (b, d, f) Typical MI spectra (single sweep) and (a, c, e) corresponding evolution of the intensity of the control output for three different states of the locking device. The evolution of the piezo voltage applied to the pump laser is also given in the upper row as dashed gray lines.

In order to be comparable with theory and numerical simulations, all the experimental investigations presented in the following chapters were realized at fixed detuning, i.e. in the *Locked mode*.

3.3 The detection/recording stage

In this section, we list the different acquisition methods that we implemented. We describe the associated setup, give the general principle and interest of each method, and discuss their limitations. This part of the setup being only intended to the analysis of the pump beam, we deliberately do not show the control beam in the following schematics for clarity.

3.3.1 Optical spectrum analyser (OSA)

We used a commercial optical spectrum analyser (OSA) in most of our experiments. It is designed to analyse waveforms in the range 1200 – 2400 nm with a spectral resolution of up to 0.02 nm (≈ 4 GHz). Its great sensitivity allows to reveal signals as weak as −70 dBm (0.1 µW). However, it is not suitable for the investigation of the dynamics of the cavity because of its rather slow acquisition speed. At maximum resolution, the limited sweeping speed of the monochromator implies that it takes up to 10 s for the acquisition of a 15 nm wide spectrum (which is a typical spectral span in our experiments), not to mention the recording time. These numbers have to be compared to the typical round-trip time of the cavity: ≈ 250 ns for a 50 m long resonator, which means that a single sweep of the OSA covers a few millions of round-trips. Consequently, the OSA can be used to record the spectrum at the output of the cavity, but we should keep in mind that it gives an average vision of the behaviour of the cavity and not a snapshot. The OSA is always implemented in our experiments and serves both for high resolution average recordings and for monitoring the state of the cavity (Is the locking device functioning or not, and/or on which branch does the cavity operate?). Examples of experimental OSA traces are reported in Fig. 3.4(b, d, f).

3.3.2 Time stretch dispersive Fourier transformation technique (TS-DFT)

Nonlinear cavities are known to exhibit complex dynamical behaviours associated to optical bistability [56–59, 125]. Adding dispersion to the system entails the appearance of localized structures which are also governed by highly complex dynamics [126]. Turing and Faraday instabilities are no exception. To investigate such dynamics, we implemented a real-time spectroscopy technique referred to as *time stretch dispersive Fourier transformation* (TS-DFT or DFT for short). In this method, the temporal envelope of a short signal is transformed into its spectrum by means of the GVD of a highly and purely dispersive element. As a consequence of the GVD, each spectral component travels at a different velocity in the dispersive element. The signal is progressively stretched and its spectrum becomes mapped into the time domain. When the signal is

sufficiently stretched, it can be directly recorded by a fast photodetector coupled to an oscilloscope [127].

The recent development of real-time spectroscopy techniques such as the DFT enabled the recording of shot-to-shot spectral fluctuations associated to ultrafast nonlinear phenomena such as MI in the single-pass configuration [44, 128] or supercontinuum generation [129]. An active version of the technique has also been developed in the context of Raman spectroscopy [127, 130]. The recent years have seen a growing interest in this technique to investigate the round-trip-to-round-trip dynamics of both passive and active fiber cavities [94, 131–135]. In this dissertation, we describe the first use of this technique to reveal the dynamics of both the MI and the parametric MI processes in optical cavities. Note that the underlying principle of the DFT method was first introduced as a way to determine the unknown GVD of a fiber thanks to a signal whose spectrum is known [136].

The "*frequency-to-time*" mapping realized by the dispersive element follows the relation:

$$T(f) = 2\pi\beta_2 L(f - f_0) + 2\pi^2\beta_3 L(f - f_0)^2 \tag{3.2}$$

where $f_0 = c/\lambda_0$. This expression allows to retrieve the spectrum from the time trace. It appears that the spectral resolution is improved by increasing the length of the dispersive element and/or its GVD. But both losses and dispersion inevitably reduce the peak intensity of the waveform such that there is a trade-off to be made between spectral resolution and vertical sensitivity. In our case, the mapping is done by an 8 –km-long dispersion compensating fiber (DCF) whose dispersive coefficients are: $\beta_2 L = 870\,\mathrm{ps}^2$ and $\beta_3 L = -5.5\,\mathrm{ps}^3$. We use a high-speed photodetector coupled to a 6 GHz oscilloscope for detection which, in the present case, limits the spectral resolution of the setup to ≈ 30 GHz [137].

Generally speaking, several parameters can affect and limit the spectral resolution of the DFT setup: the GVD and the length of the dispersive element as well as the bandwidth of the photodetector and the sampling rate of the oscilloscope. Once the DFT setup is fully determined (i.e. the parameters of the dispersive element and of the detection stage), the spectral width of the signal to analyse imposes a minimum length for the cavity by the fact that spectra of consecutive round-trips should not overlap after stretching. In our case, this condition is largely fulfilled since the stretched signals extend over 15 ns while the round-trip time of the cavity is ≈ 250 ns. In order to avoid the saturation of the photodetector and to be able to reveal weak spectral components, the pump is filtered out using a fiber Bragg grating (FBG) as a notch filter (band-stop filter) centered at the pump wavelength. This setup is depicted in Fig. 3.5.

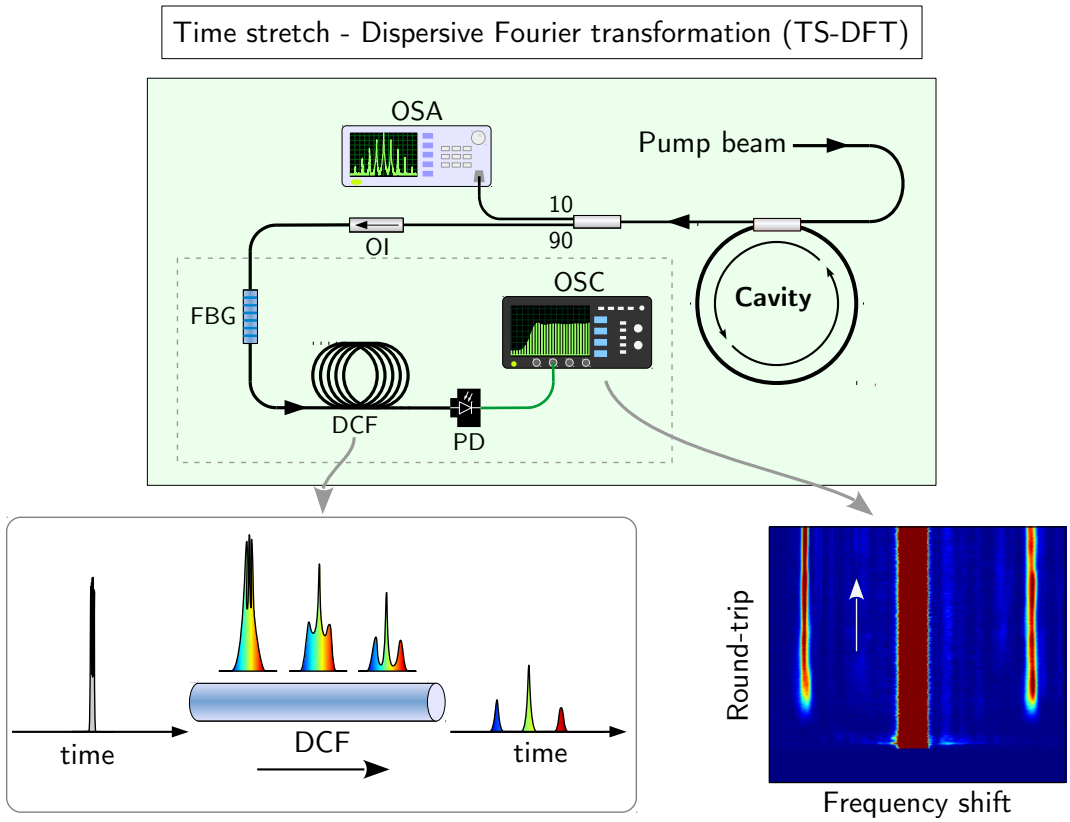

Figure 3.5 – Experimental setup for the real-time spectroscopy technique. The principle of the DFT technique is sketched in the bottom left corner. An example of experimental recording is presented in the bottom right corner. OSA: optical spectrum analyser, FBG: fiber Bragg grating, DCF: dispersion compensating fiber, OSC: oscilloscope.

Since the cavity is pumped by a train of pulses, each pulse exiting the system can be analysed with the DFT technique which allows us to record the output spectrum at each round-trip and, after numerical post-processing, to reconstruct its dynamics. An example of experimental recording is presented in the bottom right corner of Fig. 3.5. It shows how the output spectrum evolves during the 300 round-trips following the turning on of the pump beam (the transfer function of the FBG used to filter out the pump is compensated which results in the broad central red stripe). These results are detailed in Chap. 4.

3.3.3 Time lens system

Measuring in real-time the temporal waveform of ultrashort pulses is a very challenging task. Even a current ultrafast oscilloscope cannot reveal events shorter than a tens of picoseconds. In the field of optical cavities, and more specifically concerning modulation

instability, this technical limitation has hindered experimental studies in the time domain, which generally reduces to autocorrelation traces [62, 70, 138]. This method doesn't allow in general to perform recordings of the round-trip-to-round-trip dynamics. In this work, we implemented a commercial "time lens" system from PicoLuz/Thorlabs which allows to directly access the temporal waveform of the output pulses in real-time.

Temporal imaging, as it has been named in 1989 by Kolner and Nazarathy [139], finds its origin in the general concept of space-time duality, which allows a parallel between paraxial diffraction in space and dispersion in time. Accordingly, one can come to the conclusion that a spatial thin lens is analogous to a quadratic phase modulation in time [140]. Where a spatial lens can either focus or defocus a light beam, a "time lens" can compress or expand a signal without distortion (this is fundamentally different from the DFT technique described previously where the temporal shape of the signal is, intentionally, not preserved). In practice, several techniques exist to apply a temporally quadratic phase onto the signal, including FWM process on a silicon chip [141]. In fiber optics experiments, temporal imaging has recently found application in the single-shot observation of rogue waves and breathers at the output of a fiber [142, 143]. In our case, the temporal imaging is used to reveal for the first time the real-time temporal dynamics of a passive fiber-ring cavity.

The experimental setup associated to the time lens system is depicted in Fig. 3.6. In order to achieve the time lens effect, we used a commercially available ultrafast temporal magnifier (UTM) unit (framed with a dashed line in Fig. 3.6) and a band-pass filtered femtosecond laser as the pump for the FWM process. The signal enters the UTM unit along with the pump. This latter is chirped and interacts with the signal through FWM in the Silicon waveguide. This generates an idler wave which incorporates a quadratic phase shift. This wave is isolated thanks to a BPF and is actually the magnified signal that exits the UTM unit [144]. Note that, since the FWM process is very sensitive to the relative polarization between the signal and the pump, we add polarization controllers on the path of each beam. The magnified signal can then be detected and sampled by means of a photodetector coupled to a high-bandwidth oscilloscope. Thanks to the time lens system, the oscilloscope runs as if its bandwidth were multiplied by the magnifying factor of the device. Particular care must be taken regarding the synchronization between the signal and the FWM pump. Indeed, each pulse exiting the cavity has to be magnified by the time lens system and recorded in order to reconstruct the dynamics of the cavity in the time domain. In other words, the repetition rate of the femtosecond laser has to match a multiple of the FSR of the cavity. This is ensured by taking the clock signal of the femtosecond laser (which is fixed) as a reference to drive the pattern generator (PG) for the pump beam. The repetition rate of the pump beam being no longer freely adjustable, the length of the cavity has to be adjusted so as to achieve coherent driving

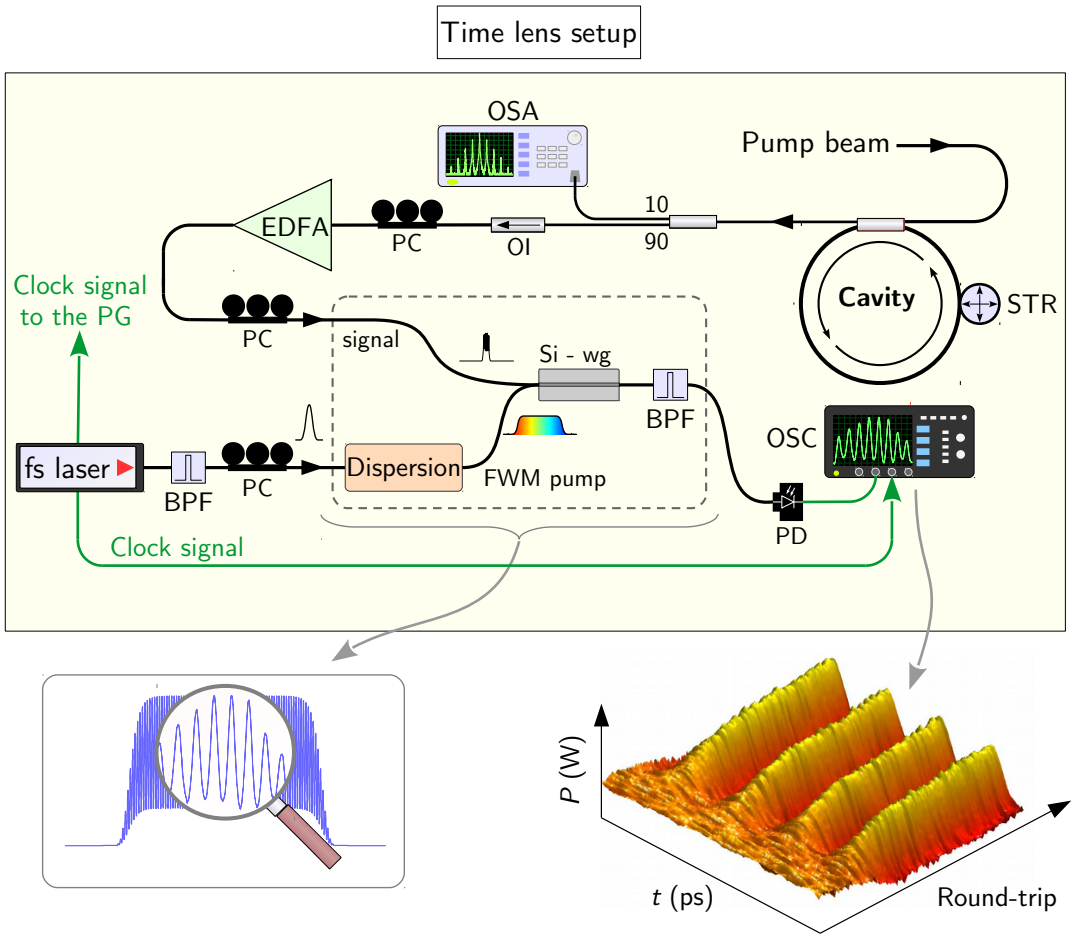

Figure 3.6 – Experimental setup for the time lens system. A sketch of the temporal magnifying concept is illustrated in the bottom left corner and an example of experimentally recorded Turing instability dynamics in the time domain is shown in the right corner. UTM: ultrafast temporal magnifier, STR: fiber stretcher, Si-wg: Silicon waveguide.

of the resonator (see Sec. 3.2.1). This is done by cutting or adding a piece of fiber to the cavity with a precision of the order of a few centimeters. A mechanical fiber stretcher embedded in the cavity then allows to finely tune the total length of the resonator. Note that this mechanical tuning is independent from the active wavelength tuning realized by the phase locking device. With our configuration, we were able to record temporal traces of consecutive round-trips with a magnifying factor of 100 and a recording length of 50 ps with a sub-ps resolution. This situation is pictorially described in the bottom left corner of Fig. 3.6: the pump pulses being 400 ps long, we only record a fraction of it, but which covers multiple instability periods with a satisfying resolution. An example of experimental recording of the dynamics of the Turing instability in the time domain is depicted in the bottom right corner of Fig. 3.6. It shows the emergence and saturation

of the so-called stable *Turing rolls* with a period of $\approx 5\,\mathrm{ps}$ which should be compared with the numerical simulation of Fig. 2.5.

3.4 Summary

- We have listed several reasons that make optical fiber-ring cavities valuable devices for fundamental investigations of nonlinear processes.
- The general configuration of our cavity system has been described. We have seen that we used two beams to operate the cavity under stable conditions: the pulsed pump beam that undergoes the nonlinear effects in the cavity, and the control beam which is used to actively stabilize the optical path length of the resonator (linear phase accumulation).
- We described the functioning of the phase locking device, its efficiency, and how the value of the detuning can be controlled and measured. To illustrate the role of the stabilization of the cavity, we showed its impact on the modulation instability spectrum.
- The three different acquisition methods that we used have been described: (i) The OSA gives access to the average optical spectrum at the output of the cavity with great resolution and dynamic range; (ii) Thanks to the time stretch dispersive Fourier transformation, the round-trip-to-round-trip evolution of this spectrum can be revealed; (iii) The ultrafast temporal structures associated to both Turing and Faraday instabilities can be recorded in real-time thanks to a time lens system.

"Knowing is not enough, we must apply.
Willing is not enough, we must do"
— Johann W. von Goethe / Bruce Lee

CHAPTER 4

Turing and Faraday instabilities in a longitudinally modulated cavity

In Chap. 2, we have described the characteristics of both the modulation instability (Turing) and the parametric modulation instability (Faraday) occurring in longitudinally modulated passive fiber-ring cavities. Chapter 3 was intended to introduce the experimental setup for our investigations of such resonators and the acquisition methods that

we implemented. In the present chapter, we report the results of the first experimental study of a longitudinally modulated fiber-ring cavity. We verify the main features of both Turing and Faraday instabilities introduced previously. In the first section, we start by listing the different requirements that need to be fulfilled to end up with the design of the cavity that we built. Next, we give an overview of what can be expected to be observed in this cavity regarding Turing and Faraday instabilities. We then detail the first experimental results concerning the stationary regime and the dynamics of both instabilities in the spectral domain in Secs. 4.3 and 4.4 respectively. Finally in Sec. 4.5, we address the case of the dynamics of these instabilities in the time domain, confirming our predictions, namely the appearance of both P1 and P2 (period doubling) regimes.

4.1 Design of a suitable cavity

The first step toward our experimental implementation of a longitudinally modulated cavity is, obviously, the determination of its dispersion design (i.e. the length and GVD of each fiber used to build the loop). The parameters of the cavity are mostly dictated by the observations we want to make but also by some technical limitations of the experimental setup. In this section, we first list the requirements for the design of the cavity and then we fix the different "free" parameters. At the end, we give the characteristics of the implemented cavity.

4.1.1 General requirements

Here we list the few essential items that need to be taken into account prior to entering into the details of the cavity conception:

- The FSR of the cavity must lie in the range of 1 – 20 MHz or equivalently, its length should roughly be comprised between 10 and 200 m. A longer cavity would lower the critical power of SBS to a level comparable with the one associated to Turing and Faraday instabilities, while a shorter cavity is not compatible with the DFT measurements (consecutive spectra would overlap after the stretching, see Sec. 3.3.2 for details about the method). Also, the sensitivity of the resonator to environmental perturbations increases with its length such that, in practice, we will try to keep it as short as possible.

- The resonator must present a normal average dispersion so that Turing and Faraday instabilities appear separately on different branches of the bistable cycle (see explanation on page 42 and Fig. 2.7).

- The spectral shift of the instability sidebands from the pump must lie in the range 0.1 – 1.5 THz. This ensures a fairly rapid acquisition of the spectrum with an OSA and a good resolution of the DFT measurements. For these latter, the frequency shift has to be sufficiently large so that we can filter out the intense pump in order to avoid saturation of the detector.
- For clarity, the Faraday regime induced by the longitudinally varying GVD must feature a single pair of sidebands instead of multiple ones as it appears in Figs. 2.7, 2.8 and 2.9. This prevents from spurious wave mixing between sidebands and will allow for a comprehensible investigation in the time domain. Indeed, the temporal waveform resulting from a single pair of sidebands in the spectrum is a modulation at the frequency of the sidebands. Conversely, the temporal waveform resulting from multiple sidebands as well as its stability are not trivial, yet should be interesting to study. Additionally, this pair of bands should correspond to the first resonance condition ($m = 1$) in order to observe the P2 regime (see Section 4.5.1 for the details).

To these requirements we add the necessity to use a standard SMF-28 coupler for the cavity as we had no other options available at the time of the experiment. Also, for the sake of simplicity, the cavity should be composed of only two pieces of uniform fibers. In other words, we want to build the cavity by simply splicing the coupler (with potentially an additional section of SMF-28) to a different fiber. These conditions will help us in determining a full set of parameters for our cavity.

4.1.2 Determination of the parameters of the cavity

We have opted for a total length of the cavity of around 50 m. In addition to fulfilling the minimum requirement for the operation of the DFT measurements, this is a good trade-off between sufficient gain for the nonlinear processes on one side, and a limited sensitivity to environmental perturbations on the other side.

All the remaining items are actually closely linked and thus, cannot be addressed separately. However, a few more points can be inferred before having to resort to a parametric study: to obtain an average normal dispersion, the fiber to be spliced to the coupler must necessarily present a normal GVD at the pump wavelength in order to compensate for the large anomalous dispersion of the SMF-28. Furthermore, to observe sidebands with a frequency shift of the order of 1 THz, we estimated that the average dispersion of the cavity should be around $1 - 1.5\,\mathrm{ps}^2/\mathrm{km}$ (This has been determined by fixing all other parameters to realistic values).

At this point, remain to be determined the length of SMF, the dispersion of the second fiber, and its length. For the latter, we have fabricated a uniform single mode

fiber of approximately 50 m with a dispersion of 2 ps^2/km at a pump wavelength of 1550 nm and a nonlinear coefficient $\gamma \approx 5.6$ /W/km. We will use this fiber as the main element of our cavity and refer to it as the DSF (dispersion shifted fiber) as its ZDW is around 1600 nm. Indeed, its low normal dispersion implies that the length of SMF-28 inside the cavity will be very small in comparison in order to obtain the aimed average dispersion.

The length of SMF-28

From there, the length of SMF-28 is the only parameter that remains to be determined. We remind that, according to our requirements, only one pair of Faraday sidebands should be observed, that is to say, the power threshold for the first Faraday sideband should be lower than the one for higher order sidebands. To determine the optimum length of SMF-28, we calculated the gain spectrum in the bistable case, for a cavity composed of 50 m of the DSF and of a variable length L_{SMF} of SMF-28 (see Sec. 2.2.2 for the equations). We recorded the power threshold for the first two Faraday sidebands as a function of L_{SMF} and identified a region of interest around $L_{SMF} = 2$ m (We can limit the recording to these two bands without affecting the conclusions). Figure 4.1 describes these results. Around this length, the average dispersion of the cavity β_2^{av} varies from 1.5 to 0.8 ps^2/km as illustrated in Fig. 4.1(a). The corresponding evolution of the power threshold for the first two sidebands ($m = 1$ and $m = 2$) is given in Fig. 4.1(b). As we can see, the power threshold for the first Faraday sideband is lower than the one of the second sideband for these parameters. For $L_{SMF} < 1.2$ m, the first band actually vanishes and the second one drives the dynamics of the system. For $L_{SMF} > 2$ m, the two thresholds increase monotonously but the one of the first sideband is always lower. Three examples of 2D gain spectrum mapping as a function of the intracavity power are given in Fig. 4.1(c-e). For $L_{SMF} = 1.3$ m (black cross), the power thresholds for the two sidebands are rather close to each other. This configuration is thus not optimum for our study. For $L_{SMF} = 2.9$ m (black square), the power threshold of the second sideband is shifted to very high power which is what we want, but the power threshold of the first sideband is also increased and its parametric gain becomes very large, which implies that the transition of the system to the chaotic regime might occur for a lower input power. In our case, we want to stay as close as possible to the conditions of the linear stability analysis and therefore do not necessarily seek a large parametric gain. A fairly good trade-off is obtained by setting the length of SMF-28 to a value between 1.5 and 2.1 m. A 2D gain mapping obtained in this range is given in Fig. 4.1(d) (black dot).

Ultimately, we have decided to set the length of SMF-28 composing the cavity to a value close to 1.6 m. Very importantly, we stress that the spectral positions of the

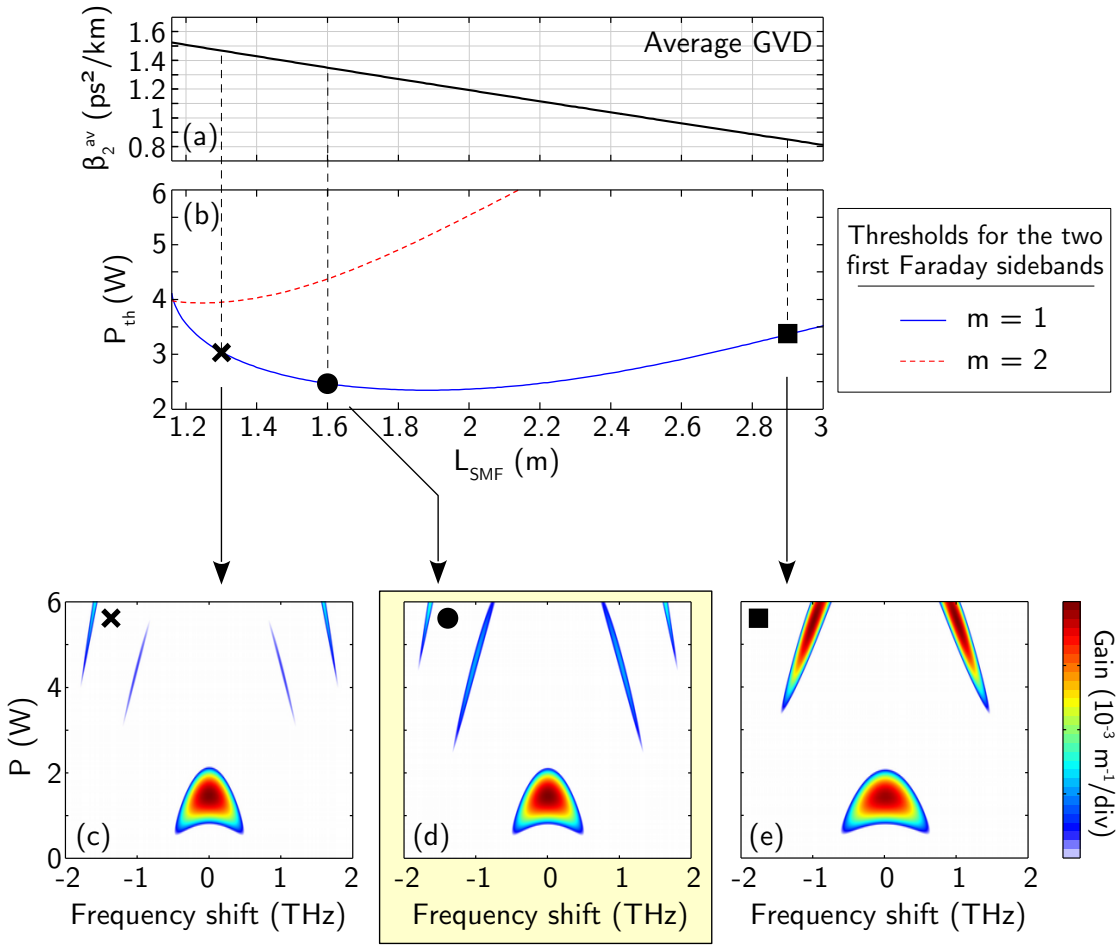

Figure 4.1 – Determination of the optimum length of SMF-28 to be included to the fiber cavity. (a) Average dispersion of the cavity as a function of the length of SMF-28 and (b) corresponding evolution of the power threshold of the first two Faraday sidebands. (c-e) 2D mapping of the parametric gain spectrum as a function of the intracavity power for $L_{SMF} = 1.3, 1.6$ and $2.9\,$m. $\beta_2^{SMF} = -19\,\text{ps}^2/\text{km}$, $\beta_2^{DSF} = 2\,\text{ps}^2/\text{km}$, $L_{DSF} = 50\,$m, $\alpha = 0.157$, $\Delta = 4$, $\gamma = 5.5\,$/W/km.

sidebands associated to the Turing and Faraday instabilities are very different. This is what allowed us to identify unambiguously in practice which instability is experienced by the system.

Parameters of the cavity

Now that the design of the cavity is fully determined, we can summarize its parameters:

The cavity consists of a 51.6 m long fiber loop which corresponds to a 4 MHz FSR. It is closed by a 90/10 standard fiber coupler. The loop consists of 1.6 m of SMF-28

($L_{SMF} = 1.6\,\mathrm{m}$, $\beta_2^{SMF}(1550\,\mathrm{nm}) = -19\,\mathrm{ps}^2/\mathrm{km}$) coming mostly from the coupler spliced to 50 m of a custom-made single-mode DSF ($L_{DSF} = 50\,\mathrm{m}$, $\beta_2^{DSF}(1550\,\mathrm{nm}) = 2\,\mathrm{ps}^2/\mathrm{km}$). All together, the average dispersion of the cavity at the pump wavelength is normal and its value is $\approx 1.35\,\mathrm{ps}^2/\mathrm{km}$. The dispersion profile of the resonator is illustrated in Fig. 4.2. The total losses originating from the coupler, the fibers, and the splicings lumped together yield a finesse comprised between 17 and 20, or equivalently, a resonance linewidth of $\approx 200\,\mathrm{kHz}$. Note that the losses and the nonlinear coefficients of the two fibers are intrinsically different, but we checked numerically that in our case, this doesn't impact the behaviour of the system. This is actually very important since it has been demonstrated that a longitudinal modulation of either the losses or the nonlinearity of a resonator can induce parametric MI in a fashion similar to the modulation of the dispersion that we study [110–112]. We will thus consider an average nonlinear coefficient $\gamma = 5.5\,/\mathrm{W/km}$ (For information, $\gamma_{SMF} = 1.2\,/\mathrm{W/km}$).

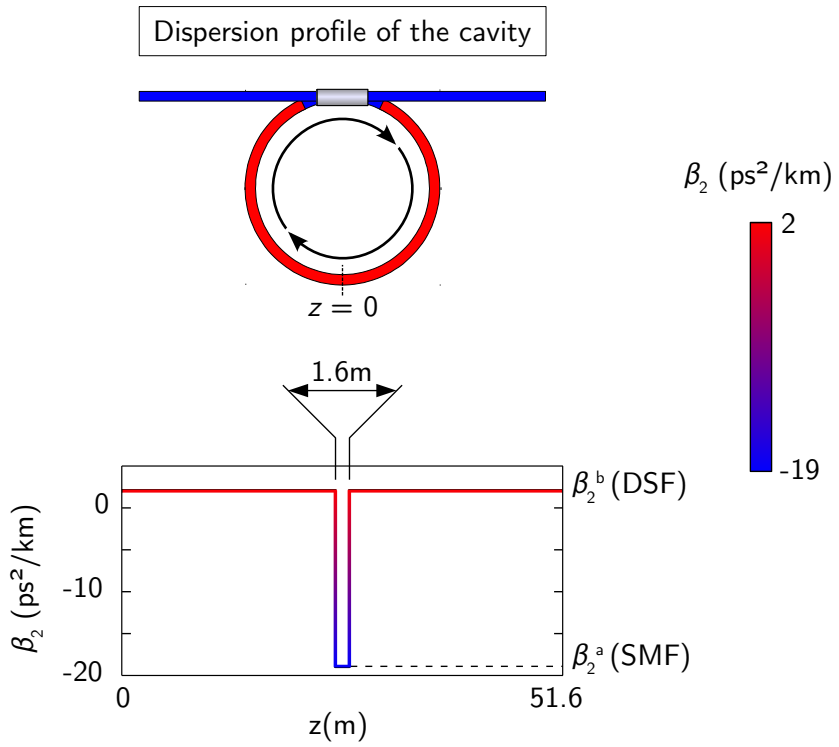

Figure 4.2 – Dispersion profile of the fiber-ring cavity built for the experimental observation of both Turing and Faraday instabilities.

4.2 What can we expect to observe?

After having introduced the fiber-ring cavity that we have designed and before the description of our experimental results, it appears essential to give a general overview of what can possibly be observed in our system. This is the purpose of this section. We will first describe the *instability chart*, which summarizes the different domains of operation as a function of the controlling parameters of our system, namely the power and the detuning. We use this chart to identify the different scenarios that we experimentally verify in the next sections.

4.2.1 Instability chart

Once the design of the cavity is fixed, only two parameters can be tuned during the experiment: the pump power P_{in} and the detuning δ_0 (We remind here that the detuning is related to Φ_0, the linear phase accumulated by the field during one round-trip). We have already described in Chap. 3 how these two parameters can be set to any desired value in experiments. Here we will use the intracavity power P instead of P_{in} to describe the state of the cavity as it happens to be more convenient, but we recall that one can switch from one to the other through the cavity response function (see Eq. (1.23) on page 22 for its expression in the LL model). We will also use the normalized detuning $\Delta = \delta_0/\alpha$ because of its common usage. We can thus say that the state of the cavity (and hence the regime of instability potentially undergone by the optical field) is fully determined for a set of parameters $[\Delta, P]$. For this reason, we decided to draw up an instability chart that gives the different domains of operation of the cavity in the (Δ, P) plane similarly to Fig. 2.1 and Refs. [63, 68]. To do so, we have calculated the gain in this plane and identified the different regions where it is non-null. The result is given in Fig. 4.3.

This figure is essentially an extension of Fig. 2.1(b) (page 30) to the case of our longitudinally modulated cavity. The region labelled "Inaccessible" still accounts for the negative slope branch of the bistable cycle which is unconditionally unstable, and, since our cavity exhibits a normal average dispersion, the Turing instability occurs on a rather small portion of the lower branch in the bistable regime (blue domain). It is bounded on the left by the fact that the normalized detuning has to exceed 4.25 for stable Turing patterns to exist [69]. It is also limited in terms of intracavity power P by the threshold $P_{th} = \alpha/(\gamma L) = 0.55\,\mathrm{W}$, and on its upper side by the merging of the Turing branch to the steady-state bistable curve (see Fig. 2.4 on page 34).

The impact of the longitudinal modulation of the dispersion of our cavity is particularly noteworthy in this figure. Indeed, a large domain covering both the monostable regime ($\Delta < \sqrt{3}$) and the bistable regime now exhibits parametric gain as a consequence

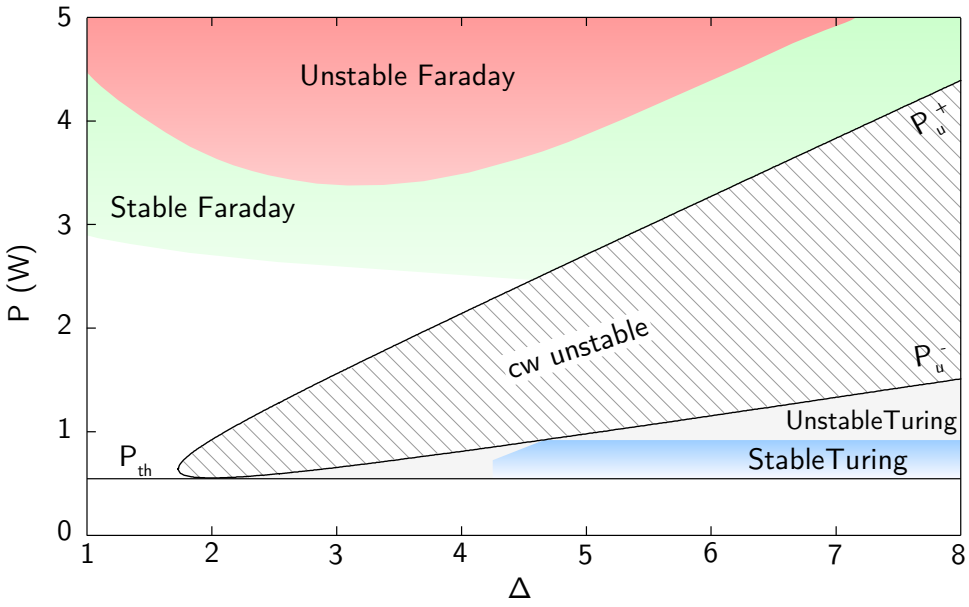

Figure 4.3 – Instability chart of the different domains of instability in our longitudinally modulated cavity.

of the dispersion management: Above a certain power threshold, the system enters the region labelled "Stable Faraday" (green domain) where the Faraday instability triggers the formation of stable temporal patterns (and consequently, a stable optical spectrum). For higher power, the system eventually becomes unstable and might even evolve toward temporal chaos which is beyond the scope of this dissertation (red domain). We emphasise here that in a uniform cavity, this domain is stable against modulations (see Fig. 2.1(b)). Note that if the average dispersion had been anomalous, the Turing domain would not have been limited to the lower branch of the bistable curve but would have largely overlapped the Faraday domain. Because we want to observe the two instabilities separately, we deliberately choose to operate in the average normal regime of dispersion.

As an illustration, we present in Fig. 4.4(a) the results of extensive numerical simulations of the LLE at a fixed detuning ($\Delta = 4$) for input power ranging from 0.6 to 10 W. We set the initial intracavity field to the steady-state of the cavity and simulate its evolution until a stable state is reached (we estimate that it is the case when the contrast of the modulation in the time domain evolves by less than 1% over 100 round-trips). We recorded the value of the power at each maxima and minima of the temporal trace at the end of each simulation and superimposed them as coloured crosses on the bistable steady-state curve at the corresponding value of input power. This way, a stable modulated state with a fixed contrast (i.e. gap between the maximum and minimum

of the temporal trace) is characterised by unique values of power for all the maxima and minima of the temporal trace. In Fig. 4.4(a), this corresponds to input powers comprised between 0.7 and 7 W (green background). We can see that as the input power is increased, the contrast of the modulation grows rapidly at first and then saturates. We point out here the excellent agreement between the threshold of the Faraday instability predicted by our analytical model (see the tip of the tongue in Fig. 4.1(d) on page 77) and the one observed in the simulations of the LLE: $P_{th}^{Faraday} = 2.5\,\mathrm{W}$. Note that we plot as a dashed gray line the portion of the upper branch of the bistable curve that is unstable with respect to the Faraday mechanism. An example of stable temporal trace obtained for $P_{in} = 3\,\mathrm{W}$ is given in Fig. 4.4(b) and the corresponding spectrum is plotted in Fig. 4.4(c).

For input powers exceeding 7 W, a stable state is never reached. We thus stop the simulation after 1000 round-trips. The corresponding temporal traces are not stable as can be inferred from the fact that multiple distinct maxima and minima of the intracavity power are recorded for each input power. We label this domain "unstable Faraday regime" (red background) and provide an example of temporal trace obtained for $P_{in} = 8\,\mathrm{W}$ in Fig. 4.4(d). We observed that, in this regime, the intracavity field still exhibits a fast modulation due to the Faraday instability but the envelope of this modulation is not constant and strongly fluctuates over consecutive round-trips which is characteristic of temporal chaos. Accordingly, the corresponding spectrum is very broad (see Fig. 4.4(e)). For this particular value of the detuning, we observe the transition to the unstable Faraday regime for an intracavity power of 3.6 W (marked by a gray bullet on the steady-state curve). By repeating this kind of numerical simulations for other values of the detuning, we determined the unstable domain in red in Fig. 4.3. We emphasise that the chaotic behaviour observed here corresponds to the strong driving regime of the cavity that is not described by the analytical model of Chap. 2. Note that this particular transition is very sensitive to most of the parameters of the system. In practice, the fluctuations of the input power and cavity detuning combined with the unavoidable synchronization mismatch between the pump repetition rate and FSR of the cavity can alter this transition.

In our case, we limit our experiments to the stable regime of the Faraday instability. The study of the chaotic behaviour that potentially occurs in this system is beyond the scope of this work.

4.2.2 Identification of noteworthy scenarios

So far in this chapter, we have established a list of requirements for our longitudinally modulated cavity and have isolated an experimental setup that fulfils all of them. We

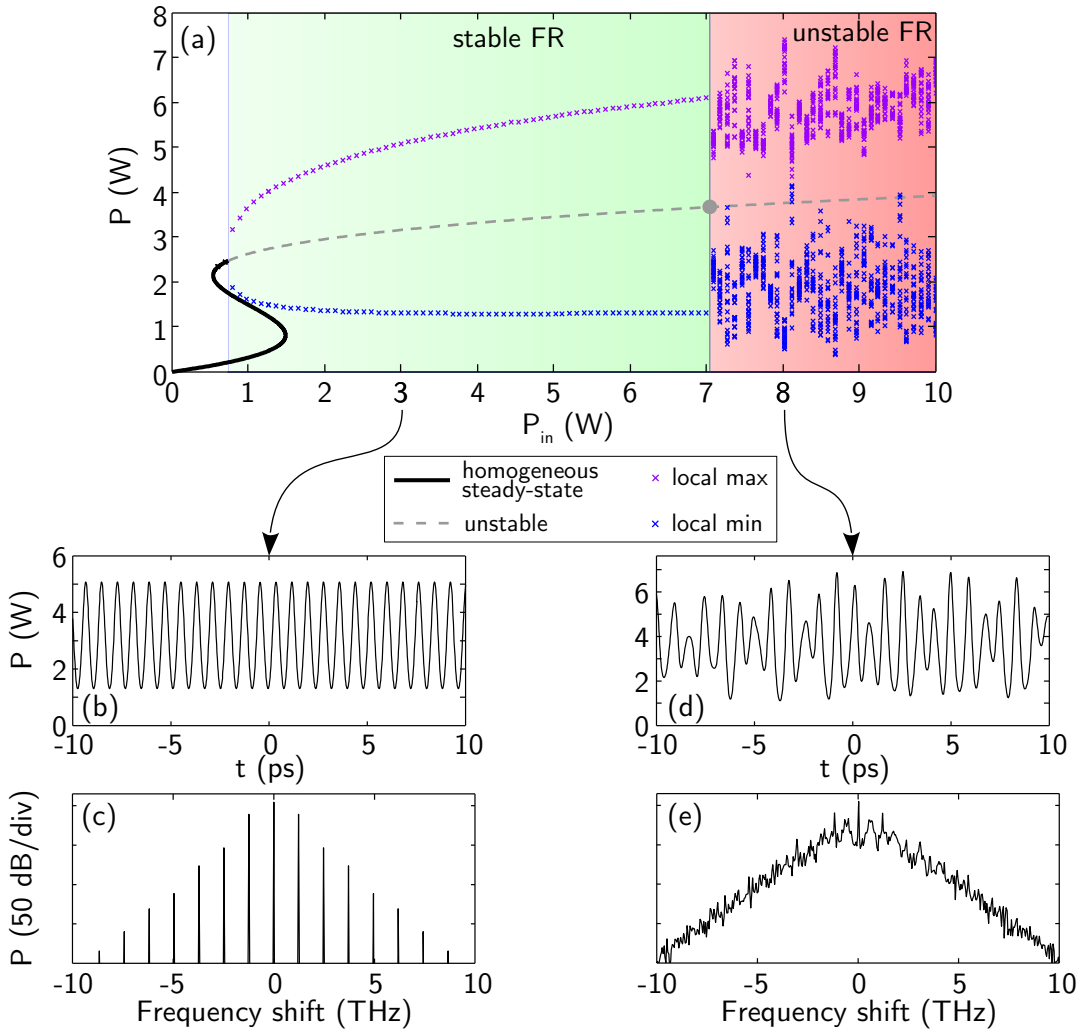

Figure 4.4 – Stability of the temporal pattern induced by the Faraday mechanism in the bistable regime ($\Delta = 4$). (a) Evolution of the contrast of the temporal modulation as a function of the input power P_{in}. (b, d) Temporal trace for $P_{in} = 3\,\mathrm{W}$ and $8\,\mathrm{W}$ respectively. (c, e) Corresponding spectra. FR: Faraday regime.

have analytically and numerically identified the different domains of instability which exist in this system. We especially evaluated the stability of the Faraday regime through extensive numerical simulations of the LLE.

From Fig. 4.3 we can considered two distinct scenarios in the bistable regime that encompass all the peculiar aspects of our device. The experiments we present in the next section aim to confirm these predictions:

- For $\Delta < 4.25$, the system can switch between the homogeneous steady-state lower branch and the upper branch which is Faraday unstable. In this case, the Turing instability can only favour such switching since no stable Turing structures can be

created.

- For $\Delta > 4.25$, the switching between the stable Turing regime and the stable Faraday regime can occur through an appropriate tuning of the input power.

In the next section, we experimentally address these two scenarios in the stationary regime, that is to say, in the case where the cavity is continuously driven by pump pulses. In Sec. 4.4, we complete these results by revealing the spectral dynamics associated with both instabilities. Finally, we confirm in Sec. 4.5 the peculiar period doubling dynamics associated to the Faraday instability by means of real-time direct measurements of the temporal waveform.

4.3 The stationary regime

In the stationary regime, the occurrence of instability in our system is reflected by the presence of a pair of sidebands in the optical spectrum whose frequency shift with respect to the pump is characteristic of either the Turing or the Faraday regime. In our case, the frequency shift of the sidebands associated to the Faraday regime is predicted to be nearly 70% greater than the one associated to the Turing regime. This will allow us to distinguish without any ambiguity which kind of instability is experienced by the system. Therefore in practice, when coherently pumping the cavity with a continuous train of pulses, the regime under which the cavity operates (either homogeneous, Turing or Faraday) can be determined using a simple optical spectrum analyser (OSA). In this section we report such experiments. A simplified version of the corresponding setup is illustrated in Fig. 4.5 (see Fig. 3.1 on page 58 for the complete setup).

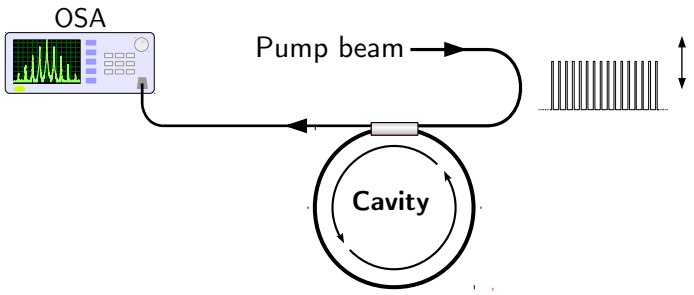

Figure 4.5 – Sketch of the experimental setup for the determination of the state of the cavity.

In order to validate the general behaviour depicted in Fig. 4.3, we will contrast experimental results obtained for two relevant values of the normalized detuning, namely, $\Delta = 4$ and 6.25.

4.3.1 $\Delta = 4$

By means of the locking setup described in detail in Sec. 3.2.2, we first set the detuning to a fixed value $\delta_0 = 0.7$ rad. We measured a finesse $\mathcal{F}$ of 18 which yields a normalized detuning $\Delta = \delta_0 \mathcal{F}/\pi = 4$. This situation is depicted in Figs. 4.6(a, b) which show side by side the bistable curve and the analytically calculated 2D plot of the parametric gain. For intracavity powers below the MI threshold $P_{th} = \alpha/(\gamma L) = 0.62$ W (corresponding to input powers below 1.9 W), the system simply stays on the homogeneous part of the lower branch (in black in Fig. 4.6(a). We recall here that the Turing branch in blue is calculated in the framework of a three wave model mentioned in Sec. 2.1.2 and originally developed in Ref. [68]). However, when the power exceeds this threshold, the system directly jumps onto the upper branch which is unstable owing to the first parametric (Faraday) resonance ($m = 1$) as shown by the gain tongues in Fig. 4.6(b). Correspondingly, in experiments we observe the stable generation of Faraday sideband pairs (primary and harmonics) as shown by the spectra reported in green in Fig. 4.6(c, d) which correspond to the two pump powers labelled 1 and 2 on the upper branch of Fig. 4.6(a). These are in excellent agreement with spectra calculated from numerical simulations of the LLE (dashed red lines).

Moreover, the primary sidebands appear at 1.24 THz and 1.22 THz, for case 1 and 2 respectively, thus confirming the expected slight down-shift for increasing power, highlighted by the close-up in the inset of Fig. 4.6(d). This is in good agreement with the analytical estimates from Eq. (2.15) which gives 1.26 THz and 1.23 THz respectively (vertical gray lines). We also notice an amplitude asymmetry between the harmonics which is attributed to the third-order dispersion (TOD) β_3 that is known to induce symmetry breaking in uniform passive cavities operated in the rather weak dispersion regime [145]. Finally, we remind that in this case (i. e. $\Delta < 4.25$), stationary Turing sidebands cannot be observed because the Turing branch is unstable (as already presented in Fig. 2.4(a) and in Ref. [68]). Yet, the Turing instability still plays a role, being responsible for the premature up-switching at $P_{in} = 1.9$ W, thus lowering the threshold for the formation of Faraday structures slightly below the up-switching power $P_{in} = 2$ W (see Fig. 4.6(a)).

To complete these results, we recorded the evolution of the steady-state output spectrum when adiabatically increasing the input power. The outcome is given as a 2D color plot in Fig. 4.7. For low power (bottom of the figure), the system lies in the homogeneous regime (only the pump appears in the spectrum). By increasing the pump power, we observe the appearance of the Faraday instability sidebands for $P_{in} = 1.7$ W, which is in good agreement with the switching threshold of 1.9 W predicted with the LL model. Note that that we have shown in Chap. 1 that the LL model differs from the full cavity map especially in this range of powers (in the vicinity of the up-switching

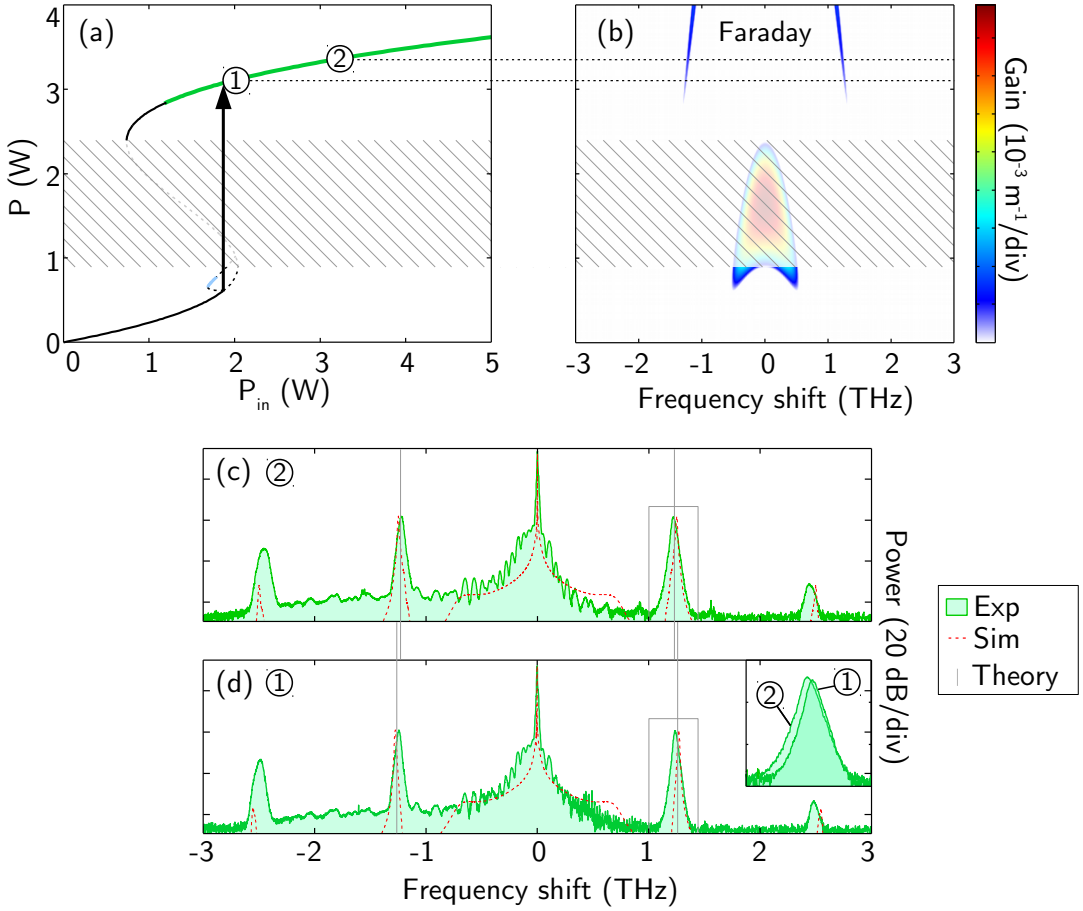

Figure 4.6 – (a) Bistable response of the cavity calculated for $\Delta = 4$ ($\delta_0 = 0.7$ rad, $\alpha = 0.175$). (b) 2D color plot of the analytic gain spectrum as a function of the intracavity power. (c, d) Comparison of experimental spectra, spectra obtained from numerical integrations of the LLE, and analytical estimates for two different powers labelled 1 and 2 on the upper branch: (c) $P_{in} = 3.2$ W; (d) $P_{in} = 2$ W. Inset: close-up view of the primary sidebands on the positive frequency shift side for the two powers.

point) which could explain the discrepancy. The slight down-shift of the sidebands as the power is further increased is also apparent as well as the amplitude asymmetry, especially when looking at the harmonics. Note that the ripples observed around the pump peak are due to the filtering stage of the pump beam which consisted of Bragg gratings for these experiments.

The results presented in this subsection thus constitute the first experimental evidence of the occurrence of Faraday instability in a passive fiber-ring resonator induced by the longitudinal modulation of its dispersion. To do this, we have set the system in a regime where no other instability is excited. This is not the case in the experiments presented in the following subsection.

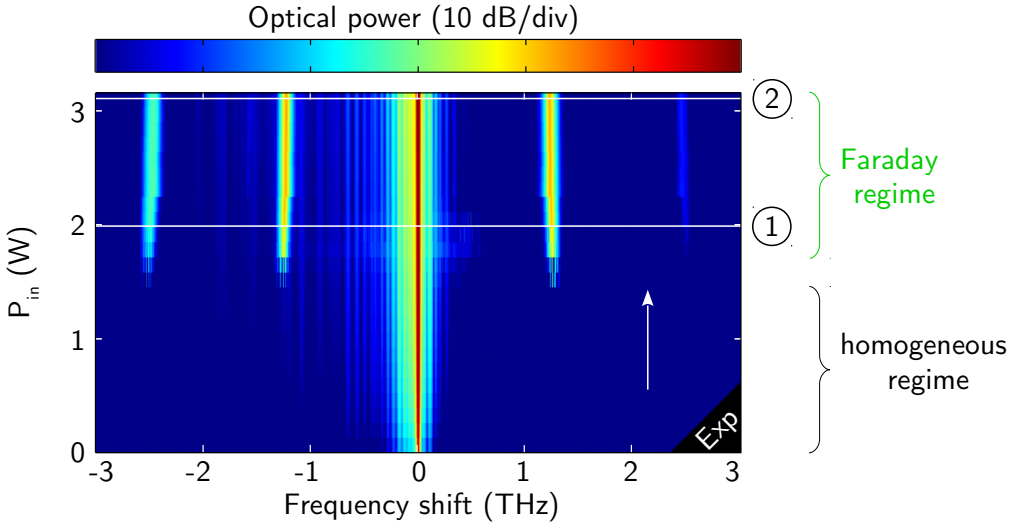

Figure 4.7 – Experimental evolution of the spectrum at the output of the cavity as a function of the input power for $\Delta = 4$. Labels on the right side of the plot refer to the cases highlighted in Fig. 4.6.

4.3.2 $\Delta = 6.25$

In a second run of experiments, we set the detuning to $\delta_0 = 1$ rad and measured a slightly higher finesse due to some rearrangement of the cavity ($\mathcal{F} = 20$). The corresponding normalized detuning was thus $\Delta = 6.25$. Again, the bistable curve and the mapping of the gain spectrum are presented in Fig. 4.8(a, b). The main difference between this case and the previous one is that the detuning parameter is now large enough for stable Turing patterns to be excited on the lower branch. This is clearly visible in Fig. 4.8(a) by the fact that above the MI threshold ($P_{th} = 0.55$ W or equivalently $P_{in} = 3.9$ W) the system now bifurcates subcritically from the homogeneous part of the lower branch (black line) to the stable Turing branch (blue line). This latter merges with the homogeneous steady-state curve for $P_{in} = 5$ W, slightly before the up-switching point ($P_{in} = 5.2$ W).

Above the merging point, the system switches again toward the upper branch of the bistable curve which is still unstable with respect to the first Faraday resonance. Figure 4.8(b) shows how the switching between the two instability regimes is accompanied by a large change in the frequency shift of the gain sidebands.

We managed to observe this switching in our experiments as illustrated by the two spectra plotted in Figs. 4.8(c, d) which correspond to the Faraday regime and the Turing regime respectively. These experimental spectra are again in good agreement with numerical simulations of the LLE (though an adjustment of the input power was necessary) and the position of the bands is well predicted by Eq. (2.15) for the Faraday regime and Eq. (2.7) for the Turing regime: we observed the bands for frequency shifts

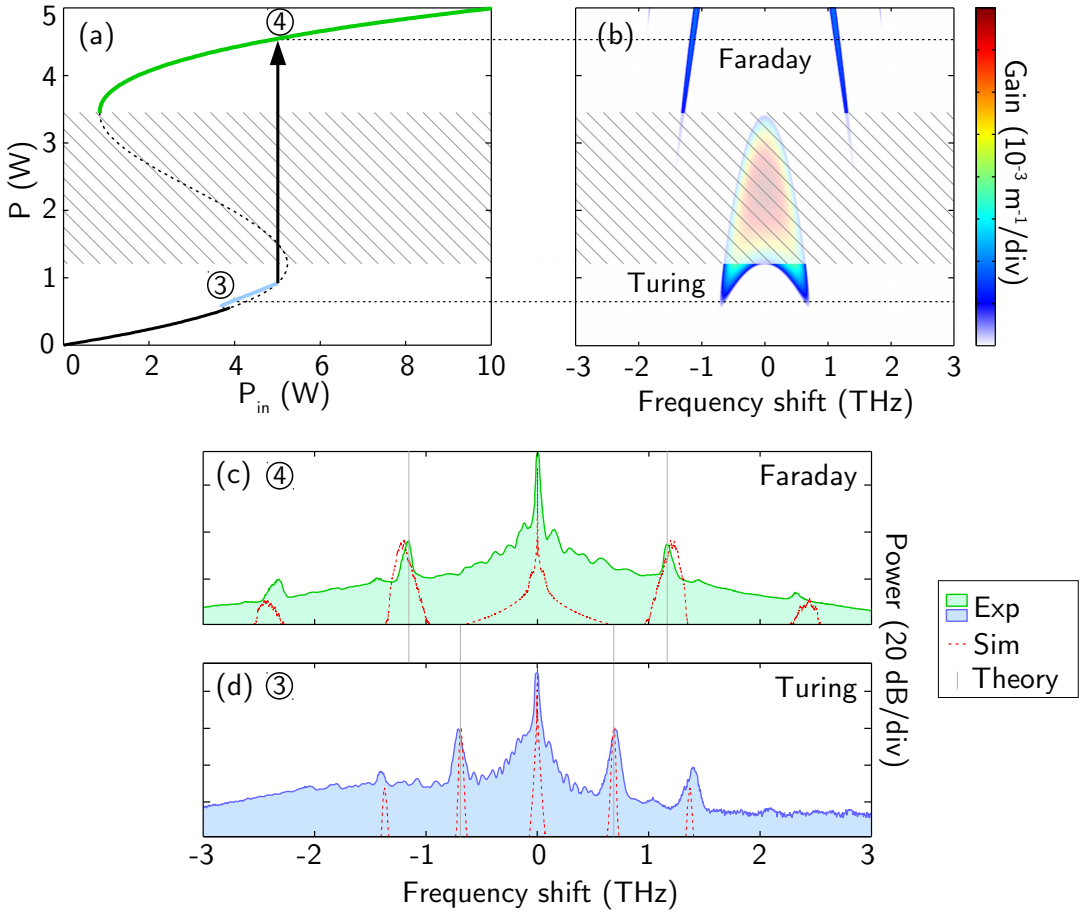

Figure 4.8 – Same as Fig. 4.6 for $\Delta = 6.25$ ($\delta_0 = 1$ rad, $\alpha = 0.157$). (c) $P_{in} = 5.05$ W (4.27 W in experiments); (d) $P_{in} = 3.9$ W (3.55 W in experiments).

of 1.16 THz and 0.70 THz, to be compared with the analytical estimates 1.15 THz and 0.69 THz respectively. The large difference of frequency shifts between Fig. 4.8(c) and 4.8(d) allows us to claim that we unambiguously observed the crossover between the two instabilities.

Similarly to Fig. 4.7, we show in Fig. 4.9 how the output spectrum evolves when the input power is increased, crossing the two regimes of instability in this configuration. The Turing sidebands are observed for input powers ranging from 3.4 to 3.9 W, which is lower than the theoretical expectation (3.9 – 5 W, see Fig. 4.8(a)). Again, we attribute this larger difference to the discrepancy between the LL model and the cavity map, which increases with the detuning. Also we note that the bistable response of the system is increasingly sensitive to environmental fluctuations because of the large detuning. Indeed, in this case, we consistently observed typically up to 15% variations in the power threshold between repeated runs of the experiment. Also, intermediate bands appear

between the pump and the primary sidebands and between the primary sideband and the first harmonic. We impute these to a resonance between the Turing mode and its subharmonic [146]. At $P_{in} = 3.9\,\mathrm{W}$, we can see the abrupt switching to higher frequency sidebands which is the clear-cut signature of the crossover to the Faraday regime.

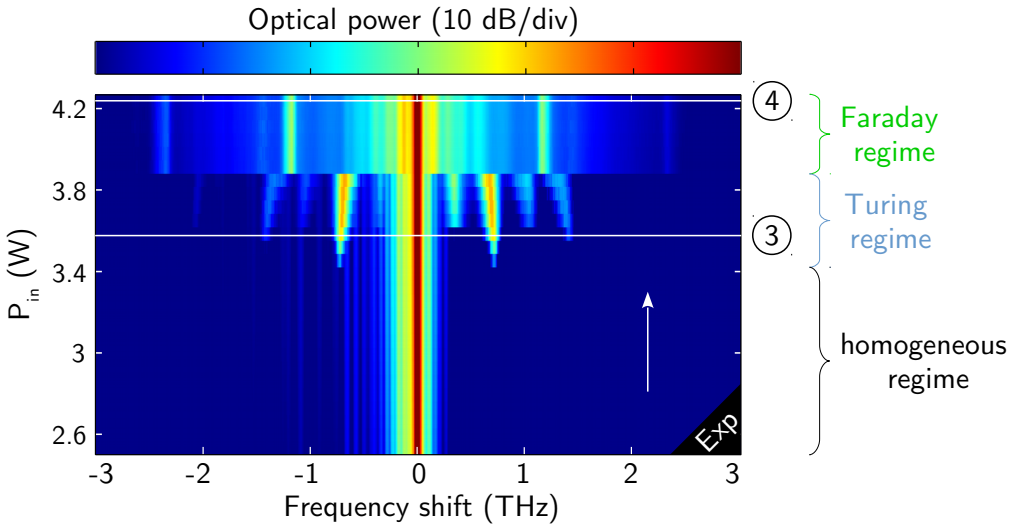

Figure 4.9 – Same as Fig. 4.7 for $\Delta = 6.25$.

Additionally, we recorded the spectrum at the output of the cavity when adiabatically decreasing the input power, the system being initially on the upper branch (and thus experiencing Faraday instability). This recording confirms in an original way the hysteretic nature of the system, that is to say, the fact that the input powers corresponding to up-switching and down-switching are distinct. We represent in Fig. 4.10(a) the bistable curve of the cavity and in Figs. 4.10(b) and 4.10(c) the evolution of the output spectrum for increasing and decreasing input powers respectively. Figure 4.10(b) is the same as Fig. 4.9 and shows that when increasing the input power starting from the homogeneous lower branch, the system enters in the Turing regime toward the end of the lower branch and then jumps on the parametrically (Faraday) unstable upper branch. This path is schematically illustrated by the blue arrow in Fig. 4.10(a). When decreasing the input power starting from this point, Faraday instabilities are sustained to input powers below the primary (Turing) threshold on the lower branch. The system then falls back to the modulationally stable part of the lower branch (Fig. 4.10(c) and red arrow in Fig. 4.10(a)). Note the slight narrowing of the sidebands when decreasing the input power in agreement with the prediction of the gain spectrum by the Floquet theory (see Fig. 4.8(b)). We point out that the down-switching power does not correspond to the down-switching knee of the bistable curve due to the fact that the system does not actually follow the homogeneous upper branch but the Faraday branch that is not

represented here. Also, the observed hysteresis is very sensitive to the synchronization between the pump pulse train and the round-trip time of the cavity and can even be inhibited if the mismatch is too important [88].

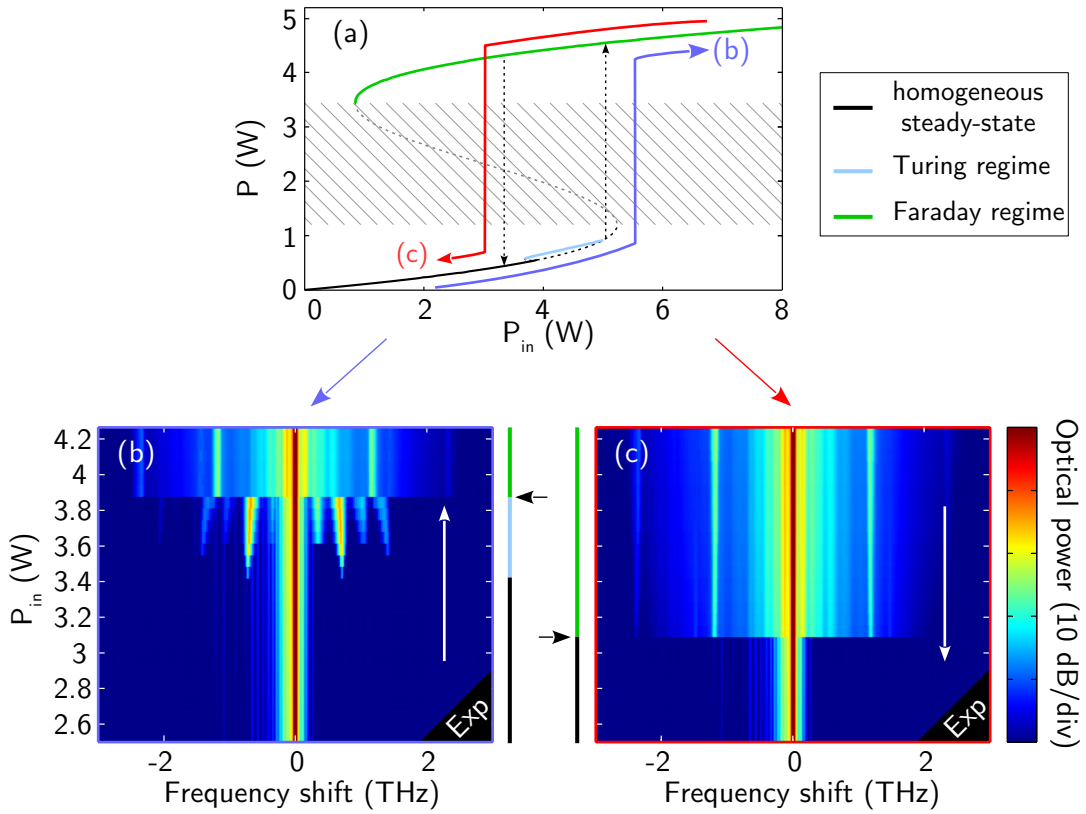

Figure 4.10 – Hysteretis of the cavity in the bistable regime highligted by the Turing and Faraday sidebands. (a) Sketch of the hysteresis cycle superimposed on the bistable curve. (b, c) Experimental recordings of the evolution of the output spectrum when the input power is successively increased and decreased respectively.

It is important to emphasise that all the spectra presented in this section can remain stationary for about 10 min which corresponds to a few billion round-trips. Until now, the only evidence of the appearance of the Turing sidebands in the normal dispersion region of a uniform passive fiber cavity was given in the transient regime [68, 69] or associated with period-doubling dynamics [67]. Our results thus constitute the first experimental observation of stationary modulation instability spectra on both the lower and upper branches of the bistable response of a passive cavity due to nonlinear mechanisms of distinct physical origins. In the next section, we reveal the dynamics of both the Turing and Faraday instabilities by means of real-time spectral recordings.

4.4 Dynamics of the instabilities in the spectral domain

We have seen previously that the regime of instability occuring in the cavity is fully determined by the intracavity power and detuning. We have confirmed this experimentally and verified two scenarios when fixing the detuning and sweeping the input power. In this section, we focus on the second scenario (i.e. large detuning) that allows the switching between Turing and Faraday instabilities by a simple tuning of the power. More specifically, we present our experimental investigation of the round-trip-to-round-trip dynamics of the system in the spectral domain using the time stretch - dispersive Fourier transformation (TS-DFT) technique (see Sec. 3.3.2 for details). We first address the buildup dynamics of both Turing and Faraday instabilities, contrasting their differences and emphasising the influence of random noise conditions. Finally, we report on our observation of the transition between the Turing and the Faraday regimes that we triggered by either an abrupt increase or a ramp of input power.

We recall in Fig. 4.11(a) the setup associated to the DFT measurements. The output field is splitted in two: one part is directed toward an OSA and a larger fraction is injected into the highly dispersive fiber which realizes the frequency-to-time mapping. The dispersed pulses are then photodetected and recorded via an oscilloscope. We estimate the spectral resolution of our system to be $\approx 30\,\mathrm{GHz}$. Note that the duration of the pulses has been reduced down to 400 ps to reach the asymptotic regime of the DFT [127]. In this section, we will use three different pumping schemes illustrated in the top right corner of Fig. 4.11(a): burst of pulses of tunable peak power, duration and separation; two-levels patterns, each level being tunable so that it can set the system either on the Turing or the Faraday branch; or a power ramp. All these schemes are easily obtained thanks to the combination of two EOMs on the path of the pump beam. Note that the tailoring of the shape of the input pulses is independent of the cavity synchronization which still needs to be fulfilled.

The accuracy of the frequency-to-time conversion has been checked by comparing the results of the DFT technique to an OSA trace. Figure 4.11(b) shows an OSA trace along with the superposition of 1500 consecutive spectra acquired using the DFT setup and the corresponding averaged spectrum. The OSA trace is shifted upward for clarity. A good agreement between the two detection methods is obtained for the range of frequency of interest, which validates our setup. Note that in this case (as in most of the following cases), we used a Bragg grating to filter-out the pump before the dispersive fiber. Its transfer function, which is not flat over the entire spectrum, is compensated in the data plotted in Fig. 4.11(b). The broad, high intensity band around null frequency shift thus corresponds to the range of frequencies filtered-out by the FBG.

Before starting to describe our experimental results, we point out that the design of

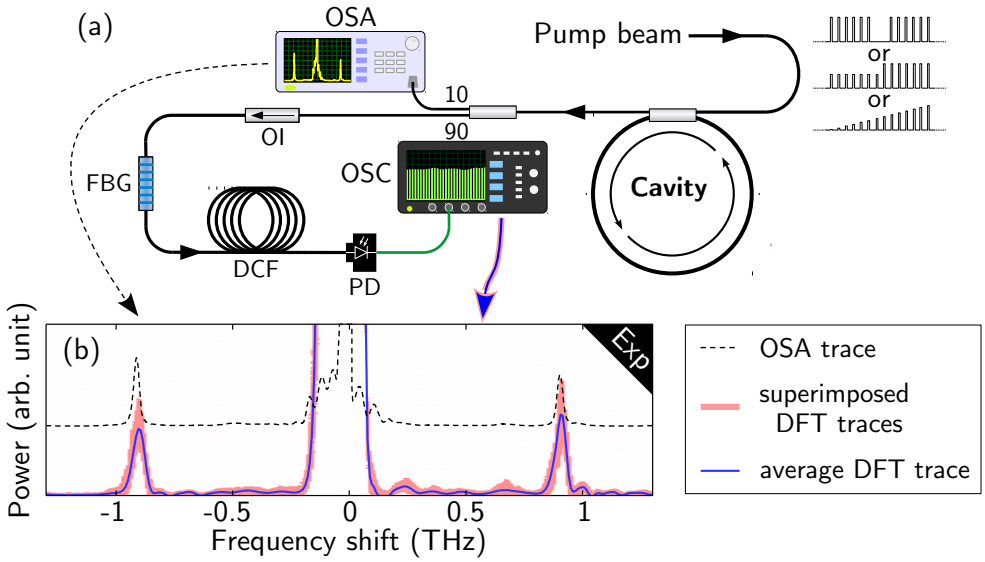

Figure 4.11 – (a) Sketch of the experimental setup for the recording of the real time spectral dynamics of the system. (b) Accuracy of the DFT method compared to the standard OSA. The resonator is driven with a pulse train of peak power 13 W and normalized detuning $\Delta = 9$, this led to the observation of the Faraday instability sidebands in the spectrum.

the cavity is slightly different as we had to reconstruct it: the lengths of SMF and DSF are now 1.8 m and 47.5 m respectively, yielding an average dispersion $\beta_2^{av} = 1.2\,\mathrm{ps}^2/\mathrm{km}$. The measured finesse is $\mathcal{F} = 19$ and the detuning is fixed to a rather large value, $\Delta \approx 9$, so that the Turing regime is accessible over a comfortable range of input powers.

4.4.1 Buildup dynamics of the Turing and Faraday instability spectra

We start by reporting on our experimental recordings of the transient evolution of the output spectrum from the empty cavity toward a stable state when a burst of pulses is launched, or in other words, when the input laser is turned on. Since the detuning is large enough, Turing and Faraday instabilities can occur separately depending on the peak power of the input pulses launched inside the cavity. The recording of the real-time spectra is triggered with the beginning of the input burst of pulses.

• For a burst of pulses of 10 W peak power, the system might experience the **Turing instability** on the lower branch of the bistable curve. This situation is described in Figs. 4.12(a, b) which show the bistable response of the cavity and the experimental input burst of pulses. The final state of the cavity on the Turing branch is marked by a black bullet. The experimental evolution of the spectrum in response to such a burst of pulses is given in Fig. 4.12(c) as a 2D color plot. The burst of pulses starts at round-trip No. 50 (indicated by the dashed white line and the appearance of the

broad pump peak) and lasts for several hundreds of round-trips. We observe that a pair of sidebands appear symmetrically with respect to the pump after roughly 100 round-trips or 20 µs in physical unit. These bands can be identified as the Turing sidebands thanks to their frequency shift relative to the pump. The growth of the power of the Turing mode eventually saturates as the system reaches a stable attractor of the dynamics [64]. This is clearly illustrated by Fig. 4.12(d) which showcases the round-trip-to-round-trip evolution of the power content of the sideband on the anti-Stokes side. After the stable state is reached, the spectrum remains stable as long as the input pump pulses are sustained or until failure of the locking device. In order to compare with the experimental recording, we conducted the corresponding numerical simulation based on the full cavity map (Equations (1.7)), including a weak monochromatic seed at the most unstable (Turing) frequency. The outcome is displayed as a dashed black line and agrees very well with the experiment. Note that in Fig. 4.12(c) the impulse response of the photodetector is responsible for the appearance of small ripples on the traces, which translate into the weak vertical bands visible on the anti-Stokes side of the pump.

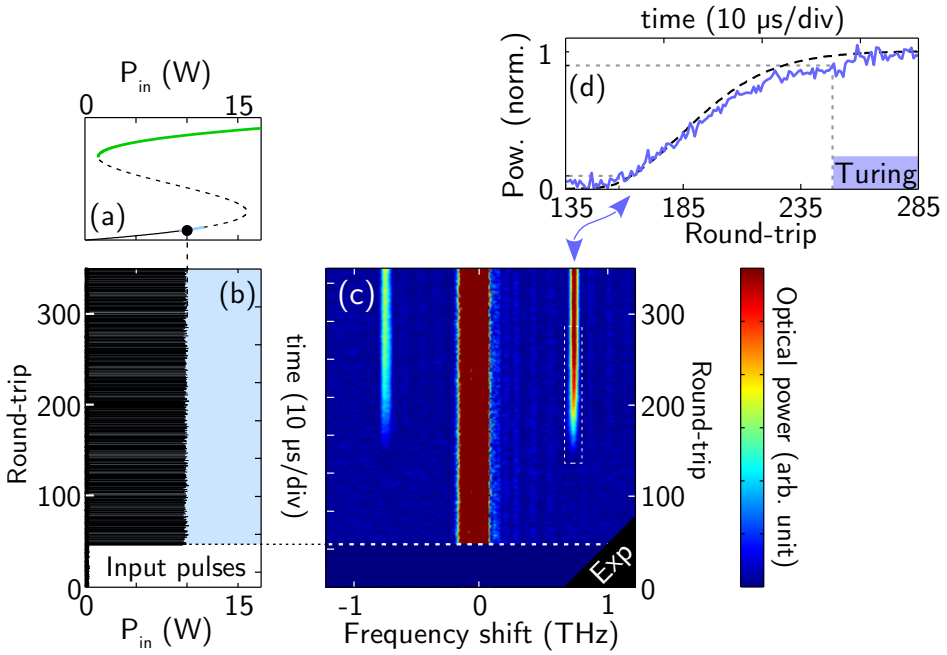

Figure 4.12 – Buildup dynamics of the Turing instability spectrum. (a) Bistable curve with the final state of the system marked by a black bullet. (b) Experimental input burst of pulses (P_{in} = 10 W). (c) 2D color plot of the evolution of the experimental output spectrum for 300 round-trips following the turning on of the laser. (d) In blue, round-trip-to-round-trip evolution of the power contained in the spectral sideband indicated by the blue arrow. The numerical simulation of this transition is superimposed as a dashed black line. The dashed gray lines illustrate the rise time of the power. $\Delta = 9$.

• A similar recording is presented in Fig. 4.13 but for 13 W peak power pulses. Under this condition, the final state of the system is upon the upper branch of the bistable curve which exhibits the **Faraday instability**. The experimental results presented in Fig. 4.13(c) shows again the emergence of a pair of sidebands but with a slightly higher frequency shift than previously and after only 50 round-trips (10 µs in physical unit) which is twice shorter than in the case of the Turing instability. This slightly higher frequency shift allows to state that these sidebands corresponds to the Faraday instability. We also observe a transient broadening of the pump just a few round-trips after the beginning of the burst that is related to the switching waves that occur when the system switches from the lower branch to the upper branch [147]. Accordingly, this broadening is not observed in the previous case since the system remained on the lower branch.

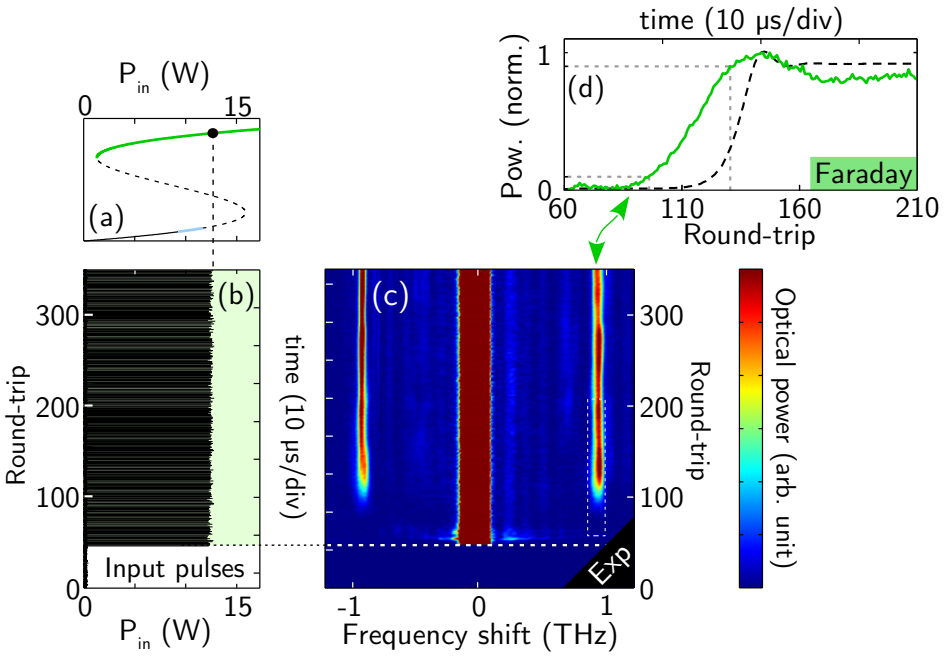

Figure 4.13 – Same as Fig. 4.12 but for P_{in} = 13 W: Faraday instability spectrum.

Again, the round-trip-to-round-trip evolution of the power contained in the anti-Stokes Faraday sideband is plotted as a green line in Fig. 4.13(d) along with the result of the numerical simulation. A good qualitative agreement is obtained, clearly highlighting the faster transition in this case compared to the case of the Turing instability. A simple and intuitive explanation lies in the difference of growth rate, or gain between the two regimes of instability. Indeed, we verified that the gain (estimated from the equations of page 46) is more than two times higher in the Faraday case compared to the Turing case. On the other hand, the rise time of the Faraday mode is nearly two times shorter than the one of the Turing mode, as can be seen by the dashed gray lines in Figs. 4.12(d) and

4.13(d) that indicate 10% and 90% of the maximum power. This supports the argument that the difference in the dynamics between these two regimes is essentially driven by the strength of the gain.

To conclude, we have observed experimentally for the first time and in great details the transient spectral dynamics leading to the emergence of stable Turing and Faraday patterns in a passive cavity. To do so, we have measured in real-time the growth and saturation of the power of the unstable sidebands thanks to the DFT technique. We note that, in a previous experimental study by Coen *et al.*, the spectral dynamics of a uniform passive fiber-ring cavity with normal dispersion was addressed and proved the role of MI as a triggering mechanism for the up-switching process. However, no stable modulated state was reached in that case [68].

Impact of the noise

Over successive runs of the previous experiments, we consistently observed variations on the transient regime of the cavity in terms of rise time. We attributed this to the random noise intrinsic to the system and verified it through numerical simulations of the full cavity map. We performed 2000 numerical simulations of the same transition from the empty cavity to the stable Faraday regime, each one only differing from the others by the noise conditions. We also allowed a 2% fluctuation of the input power and detuning from round-trip to round-trip which is close to realistic conditions. The normalized evolution of the power of the Faraday sideband for each simulation is plotted in Fig. 4.14(a) as a gray line and one of the trace is highlighted in green for clarity.

We can see that, even if the initial and final states are always the same, the different traces spread over tens of round-trips. Note that this result is also obtained without allowing the 2% fluctuation of the parameters, this latter only being responsible for the noisy aspect of the traces. For each trace, we pointed the round-trip at which the power exceeds half of its maximum and we plot in Fig. 4.14(b) the corresponding histogram. As we can see, most of the simulations yield a transition around the 85^{th} round-trip but in some cases, it can be delayed beyond the 100^{th}.

4.4.2 Switching between Turing and Faraday instabilities

As we have previously demonstrated in the stationary regime (see Sec. 4.3.2), it is possible to switch between the two instability regimes by simply tuning the input power while keeping the detuning fixed. The signature of this switching is the abrupt change of the frequency of the sidebands in the optical spectrum, each position of the sidebands being characteristic of one regime of instability. Here, we address the question of the transition between those instabilities by recording the real-time evolution of the

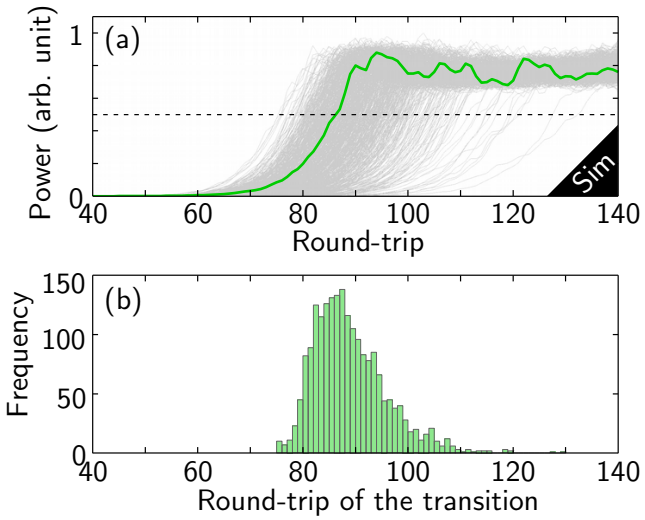

Figure 4.14 – Impact of the random noise conditions on the dynamics of the transition to the Faraday regime. (a) Round-trip-to-round-trip evolution of the power of the Faraday sideband for one particular numerical simulation (green line) superimposed on the outcome of 2000 identical numerical simulations except for the random noise (gray lines). (b) Histogram highlighting the spreading of the results: for each simulation, we point the round-trip at which the power exceeds half of its maximum.

spectrum at the output of the cavity when tuning the input pump power either abruptly or smoothly. In both cases we observe the crossover between Turing and Faraday regimes with qualitatively different dynamics.

Transition induced by an abrupt power increase

Figure 4.15(c) shows the experimental evolution of the output spectrum corresponding to the pump power evolution of Fig. 4.15(b): around the round-trip No. 200, the pump power is abruptly increased from 10 to 13 W (from one round-trip to the next one), thus triggering the transition. Note that this power step is preceded by a large number of pump pulses of 10 W peak power so that the system is actually in a stable Turing state at round-trip No. 0. An example of single-shot spectrum exhibiting the Turing sidebands is presented in Fig. 4.15(f). After the power increase, the Turing sidebands rapidly vanish and the Faraday sidebands emerge in a fashion similar to the one depicted in Fig. 4.13(c). The transition is characterized by a sudden boost of the power of the low frequency components (illustrated in the single-shot spectrum of Fig. 4.15(e)) which, again, corresponds to the switching of the system from the lower branch to the upper branch. Finally, the system stabilizes over a Faraday state characterized by the sidebands with a slightly higher frequency shift than the Turing ones (Fig. 4.15(d)).

Similarly to Figs 4.12(d) and 4.13(d), the evolution of the power of the spectral

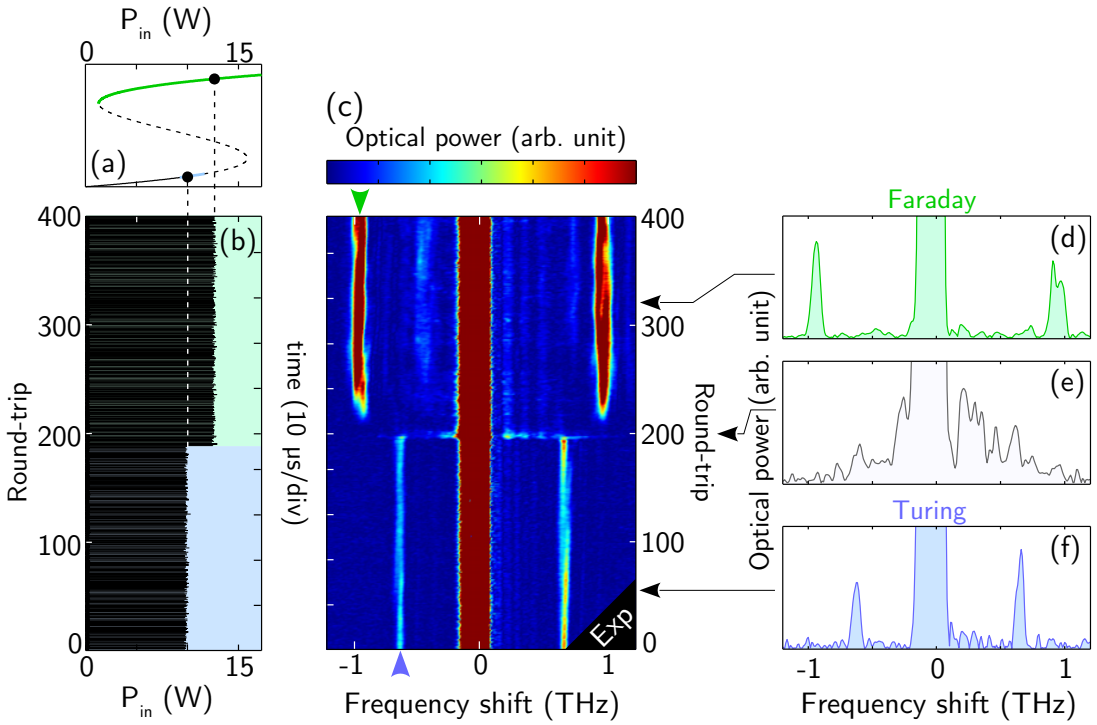

Figure 4.15 – Transition between Turing and Faraday instabilities triggered by an abrupt increase of input power. (a) Bistable curve with the initial and final states of the system marked by black bullets. (b) Experimental input pulses. (c) 2D color plot of the corresponding evolution of the output spectrum. (d-f) Single-shot spectra peaked at three relevant stages of the recording. $\Delta = 9$.

content at the characteristic frequencies of both Turing and Faraday instabilities has been extracted from Fig. 4.15(c) (see the green and blue triangles) and is plotted in Fig. 4.16(a). As described previously, we observe the rapid vanishing of the Turing band preceded by a short peak consecutive to the switching to the upper branch, before the Faraday instability settles in. Both curves being normalized with respect to the maximum of the power of the Faraday mode, we can see that the power of the Turing band is nearly 4 times weaker than the one of the Faraday band. Corresponding numerical simulations are presented in Fig. 4.16(b) and accurately reproduce this behaviour. Discrepancies can be found in the delay between the vanishing of the Turing sidebands and the emergence of the Faraday ones and in the intensity of the peak at the transition, but we attribute these to the sensitivity to the noise conditions discussed earlier. Indeed, quantitatively different results were obtained over consecutive recordings but the scenario remained the same. On the same footing, we note the very good agreement in the relative powers of the stationary levels of the two regimes.

Conversely, we point out that the bistable nature of the system and the underpinning

hysteresis (demonstrated in Sec. 4.3.2) can result in a more complex dynamics for the "Faraday-to-Turing" transition, which extends beyond the simple tuning of the input power that we applied. We thus do not address this case here.

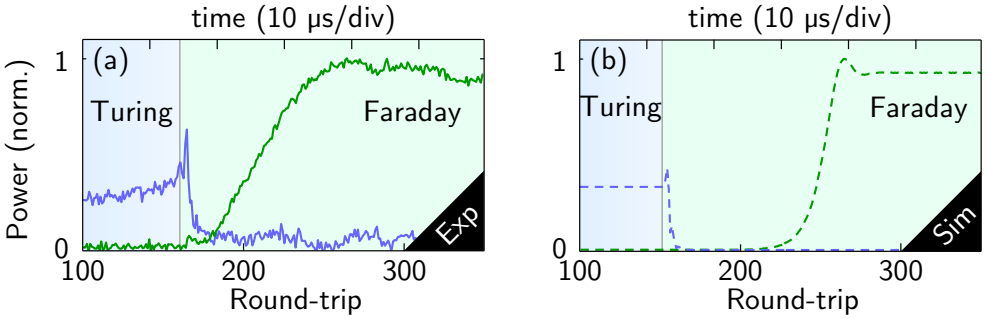

Figure 4.16 – (a) In blue (green), round-trip-to-round-trip evolution of the power contained in the spectral sideband associated to the Turing (Faraday) instability extracted from Fig. 4.15(c). The input power of 10 or 13 W is echoed in the blue or green background respectively. (b) Corresponding numerical simulations.

Transition induced by a ramp of power

The crossover between Turing and Faraday instabilities can also be observed when the input power is linearly increased. We have performed such recordings by launching in the cavity pulses modulated by a sawtooth waveform. Two relevant results which emphasize the key role of the slope of the sawtooth modulation (i.e. the speed at which the power is increased) are illustrated in Fig. 4.17. For these experiments, the detuning was set to $\Delta \approx 7$ and the pump has been only partially filtered-out so that the increase of the input pump power can be directly visualized in the spectrum by the intensity of the central band.

• For a speed of 2 W/100µs (left panels), the system crosses the Turing region rather fastly and, consequently, Turing sidebands are observed during only a few tens of round-trips before the switching occurs. After that, the system experiences the Faraday instability as confirmed by the presence of the high frequency sidebands.

• For a slower speed of 1.5 W/100µs (right panel), the Turing regime is clearly distinguished between round-trips No. 800 and 1200 and we can see the power dependence of the sidebands' frequency. Around the 1300^{th} round-trip, the switching occurs, still visible through the transient spectral broadening of the pump, and the Faraday instability settles in. Figure 4.17(d) shares great similarities with Fig. 4.9 on page 88 obtained in the stationary regime. We can thus state that this recording corresponds to a nearly adiabatic increase of the input power.

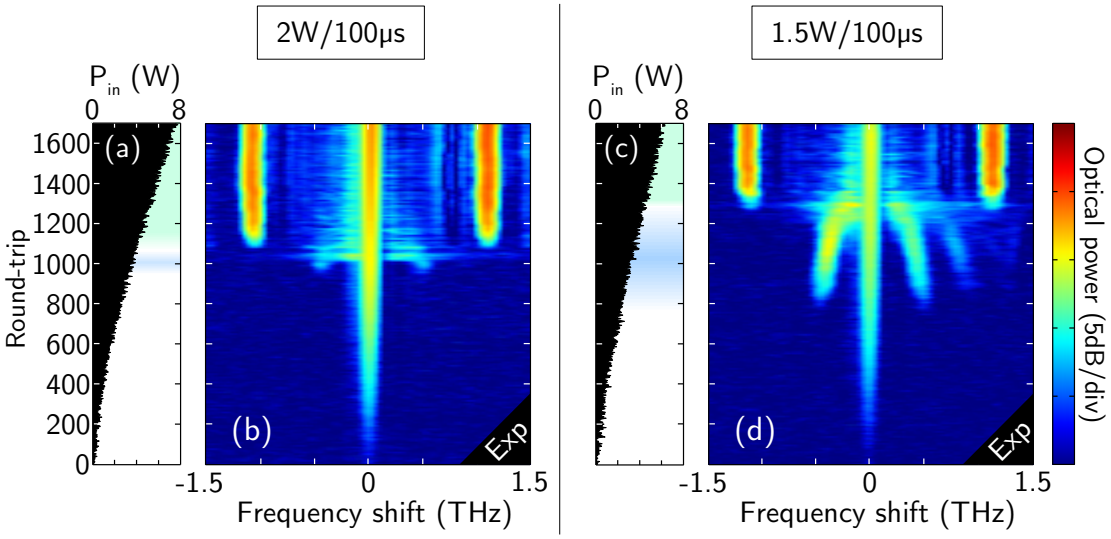

Figure 4.17 – Dynamical recordings of the crossover between Turing and Faraday instabilities as the input power is linearly increased at two different speeds. (a, c) Evolution of the pump power for 1650 round-trips for the two speeds respectively. (b, d) Corresponding 2D color plot of the evolution of the output spectrum. $\Delta = 7$.

To summarize, we have reported in this section our investigations on the dynamics of both Turing and Faraday instabilities in the spectral domain using the real-time DFT technique that allows for round-trip-to-round-trip recordings of the spectrum. We revealed the buildup dynamics of these instabilities as well as their interaction when the input power is tuned. In the next section, we report the first experimental investigation of the ultra-fast temporal dynamics associated to the Turing and Faraday regimes.

4.5 Dynamics of the temporal waveforms

Until now in this chapter, Turing and Faraday instabilities have been distinguished one from the other thanks to the difference of spectral positions of the generated sidebands. In this section, we will show how we have further distinguished these two mechanisms through real-time recordings of the dynamics of the temporal waveform at the output of the cavity. Indeed, we demonstrated in Chap. 2 that in our case, the Faraday instability, contrary to the Turing instability, can exhibit a period doubling dynamics whose signature is evident in the time domain. First, we will see why our cavity is particularly suitable for this experiment. Then, we recall the setup we used for the ultrafast temporal measurements, and finally, we report on our experimental results which confirm the predicted temporal dynamics for both Turing and Faraday instability regimes.

4.5.1 Why is our cavity suitable?

Keeping in mind that we want to confirm that Turing and Faraday instabilities can, in principle, be governed by different temporal dynamics, it is important to establish whether it is actually the case in our cavity.

• First, the Turing instability as we have described it until now always follows a P1 dynamics (i.e. in the stationary regime, the temporal trace is reproduced identical to itself at each round-trip). This is the case when the linear phase accumulation Φ_0 is set close to a resonance, which is the case in our experiments. Note however that, under antiresonant conditions, the modulation instability follows a P2 dynamics. The existence of this regime has already been proved but only through the observation of the P2-MI spectral sidebands [93]. We do not address this case here and thus, the Turing instability is always associated to a P1 dynamics in our system.

• Concerning the Faraday instability, the conditions under which the system follows a P1 or a P2 dynamics have already been discussed in details in Sec. 2.2.3 on page 47. We remind that it solely depends on the number of dispersion periods per round-trip and the order of the Faraday resonance which governs the dynamics. In our cavity, and according to the requirements we fixed for its design, the period of the dispersion management is equal to the cavity length, or equavalently, the dispersion profile consists of only 1 period ($L/\Lambda = 1$), and Faraday instability sets in by the destabilization of the 1^{st} resonance. These two quantities being odd, the Faraday instability in our cavity is characterized by a period doubling dynamics (see Table 2.1 on page 48).

These considerations lead us to the conclusion that our cavity can indeed be used to observe both P1 and P2 dynamics associated to Turing and Faraday regimes respectively.

4.5.2 Setup

The observation of the two temporal dynamics of interest are very challenging since they imply recording temporal traces with, in our case, a sub-ps resolution. Indeed, as we have seen in the previous sections, the two instabilities involve the generation of sidebands whose frequencies lie in the range 0.5 – 1.2 THz or, equivalently, temporal features in the range 0.6 – 2 ps. This is below the current limitation of detectors and oscilloscopes whose bandwidth hardly exceed 100 GHz. Also, the fact that we want to access the round-trip-to-round-trip dynamics of the temporal waveform implies that we have to perform single-shot recordings at a repetition rate of a few megahertz (i.e. we have to get a temporal trace for each pulse exiting the cavity). This prevent us from implementing an optical sampling oscilloscope or an autocorrelator system which cannot be used to record non-repetitive events. To circumvent this, we have thus implemented the time lens system that we have described in Chap. 3. This acquisition

scheme allowed us to record the temporal waveform of the output pulses over a window of a few tens of picoseconds with a resolution of $\approx 300\,\mathrm{fs}$. In a fashion similar to the real-time spectral recordings presented earlier, we are able, after numerical post-processing, to reconstruct the temporal dynamics of the system. The setup for the recording of the temporal traces is depicted in Fig. 4.18 and shows the commercial ultrafast temporal magnifier (UTM-1500) unit from PicoLuz/Thorlabs that we used.

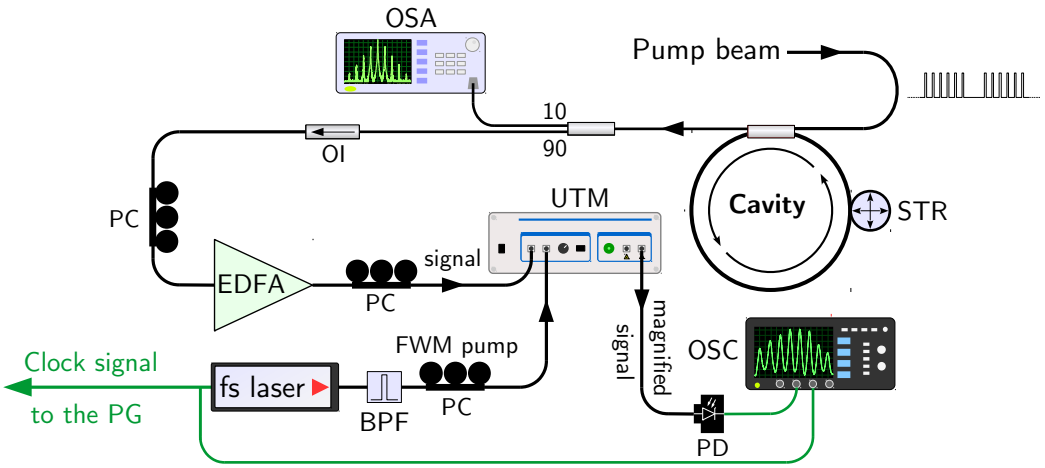

Figure 4.18 – Sketch of the experimental setup for the recording of the real time temporal dynamics of the system. UTM: ultrafast temporal magnifier.

We recall that the mechanical fiber stretcher embedded in the cavity is absolutely essential in the operation of the system: In order to get the time lens system synchronized with the pump pulses, we use a clock signal derived from the femtosecond laser (used for the time lens system) to drive the pattern generator. Accordingly, the length of the cavity has to be precisely tuned so that it corresponds to the input pulses repetition rate. In our case where we record the dynamics of the temporal waveform, extreme care has to be given regarding the minimization of the synchronization mismatch. Indeed, the slightest mismatch is responsible for a linear drift of the temporal patterns generated through the instabilities which might prevent us from getting unambiguous results. In the Appendix A, we present experimental results obtained with the same setup in a uniform cavity, confirming for the first time the drift of the Turing pattern induced by the synchronization mismatch. We also noticed that the latter is reflected in the spectral domain by a shift of the frequency of the instability sidebands which can be used to optimize the synchronization. In the present case, we managed to reduce this mismatch such that the linear drift is nearly null over a tens of round-trips.

Again, the cavity was slightly adjusted: its total length was 49.7 m with 1.6 m of SMF-28. For the experiment, we set the detuning at a value $\Delta \approx 5$ which, we recall, is

large enough for both Turing and Faraday instabilities to be observed. The experiments detailed in this section do not necessitate a control over the Turing regime as critical as the ones from the previous section. For that reason we fixed the detuning to a smaller value which allows us to operate the cavity in both Turing and Faraday regimes while keeping the input power as low as possible.

4.5.3 Results

The experimental results basically consist in two recordings showing the evolution of the temporal waveforms for 8 consecutive round-trips in the steady-state of each of the regime of instability. We restricted the fast time axis of the plots so that it covers 4 periods of the temporal pattern. The results of numerical simulations of the LLE presented in Figs. 4.19(a-d) illustrate the two dynamics associated to P1 and P2 regimes. In both cases, we recorded the temporal waveforms after each round-trip and stacked them to produce a 2D color plot. For the Turing mechanism (P1), Fig. 4.19(a) shows how the temporal waveform remains identical from one round-trip to the other in the stationary regime (see Fig. 2.12 on page 51 for a more thorough explanation). Correspondingly, the 2D color plot of Fig. 4.19(b) exhibits 4 bright vertical stripes at the maxima of the waveforms. On the other side, for the Faraday mechanism (P2), Fig. 4.19(c) shows that the trace alternates between two out-of-phase modulated waveforms at each round-trip (see Fig. 2.10 on page 49 for a similar figure). This time, the 2D color plot takes the peculiar form of a check pattern [Fig. 4.19(d)].

We aimed to reproduce these two figures in experiment to directly and unambiguously demonstrate the occurrence of period doubling in the Faraday regime in contrast with the Turing regime. To do so, we first recorded consecutive temporal traces in response to a burst of pulses of peak power $P_{in} \approx 3.6\,\mathrm{W}$ and stacked them in order to reconstruct the dynamics. For this power, the system experiences the Turing instability. As expected, we observed the growth of the Turing pattern until it reached a quasi-constant contrast ratio. However, the first recordings featured a linear drift that, as previously described, are due to a small synchronization mismatch between the input pulses and the cavity round-trip time. By gently adjusting the length of the cavity by means of the intracavity fiber stretcher, we reduced the synchronization mismatch and reiterated the measurements. After several iterations of these two steps, we managed to obtain a recording of the evolution of the Turing pattern over consecutive round-trips which exhibits a very low temporal drift. These results are given in Figs. 4.19(e, f) which retain the same form as Figs. 4.19(a, b). They clearly illustrate the generation of a stable modulated state with a period of 1.7 ps. The superposition of 4 consecutive traces in Fig. 4.19(e) shows an excellent overlap which is characteristic of the P1 regime.

Next, we increased the input power up to 4.8 W and performed the same recording. This time, the system is expected to undergo the P2 Faraday instability. Note that we operated rather fastly and in a stable environment to make sure to maintain the synchronization mismatch to a very low value. Corresponding results are plotted in Figs.4.19(g, h) and should be compared to Figs. 4.19(c, d). The difference with the previous experimental recording is striking, as is the agreement with our prediction: Temporal traces of even round-trips are easily distinguished from odd ones and the check pattern is clearly identified in Figs. 4.19(g) and (h) respectively. This result is a clear evidence of the period doubling dynamics associated to the parametric MI (Faraday) that we predicted. We measured a period for the Faraday pattern of around 950 fs which is, as expected, shorter than the period of the Turing pattern. Note that a small synchronization mismatch of ≈ 35 fs per round-trip is observed but we point out that it represents less than 0.01% of the pump pulse duration and 0.00002% of the round-trip time.

To summarize this section, we have experimentally recorded the round-trip-to-round-trip evolution of the modulated temporal waveform generated through the Turing and Faraday instabilities with a remarkable resolution. These single-shot acquisitions allowed us to unambiguously demonstrate that the two regimes exhibit distinct dynamics, and especially that the parametric Faraday pattern is associated to period doubling. This constitutes the first direct observation in the time domain of such dynamics induced by parametric MI.

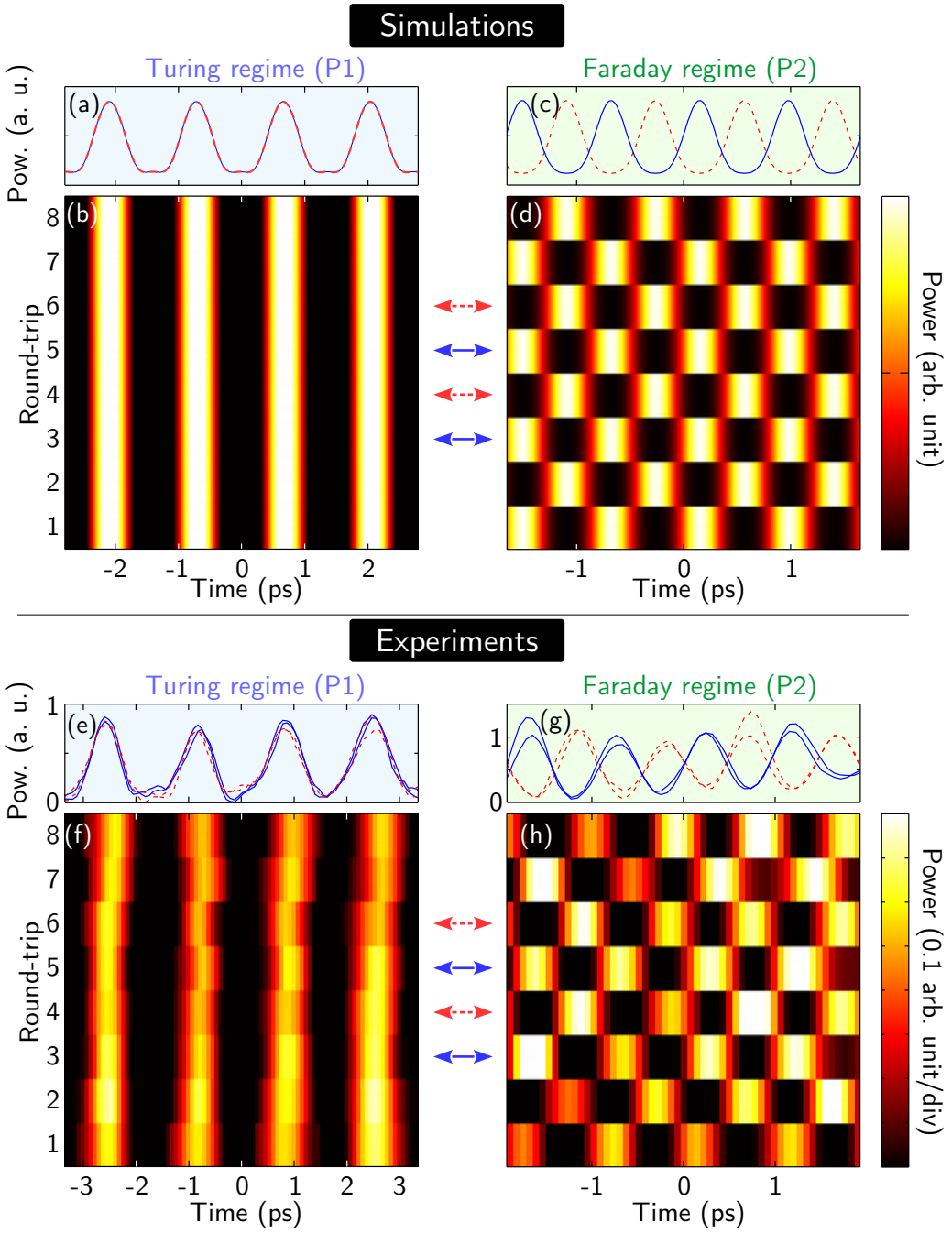

Figure 4.19 – (a, c) Temporal waveforms of 4 consecutive round-trips superimposed in the stationary regime of the Turing (P1) and Faraday (P2, period doubling) instabilities respectively, obtained by numerical simulations of the LLE. (b, d) Corresponding 2D color plots of the evolution of the temporal waveform recorded after each round-trip for 8 consecutive round-trips. (e-h) Corresponding experimental recordings obtained at the output of the cavity. Coloured arrows indicate the temporal traces of the same colour.

4.6 Summary

- We have described the parameters of our modulated fiber-ring cavity, aiming to demonstrate the existence of modulation instability (Turing) and parametric modulation instability (Faraday) in the same device. The design of the cavity fulfils several requirements that we listed.
- The different regimes under which the designed cavity operates (homogeneous/ Turing/Faraday, stable/unstable) have been determined as a function of the parameters that we control in experiments, i.e. the input power and the phase detuning. This allowed us to establish two experimental scenarios that encompass all the peculiarities of the system.
- We first demonstrated that our system indeed exhibits both Turing and Faraday instabilities through the observation of spectral sidebands at frequencies specific to each of the instabilities. These results obtained in the stationary regime also confirmed the hysteretic nature of the resonator in the bistable regime.
- The experimental real-time / round-trip-to-round-trip dynamics of the instability spectrum has been revealed, showing the emergence and the interplay between the different instabilities when the input power is varied at characteristic speeds with respect to the time scale of the resonator.
- We have performed time-resolved measurements (with a sub-ps resolution) of the round-trip-to-round-trip dynamics of the modulated waveforms generated through both Turing and Faraday mechanisms. These ultra-fast recordings confirmed a fundamental difference that we introduced previously between the two processes: The parametric modulation instability exhibits a period doubling dynamics as opposed to the modulation instability. This is the first time, to our knowledge, that period-doubling is directly identified at this time scale.

"Nothing is too wonderful to be true, if it be consistent with the laws of nature"

— Michael Faraday

CHAPTER 5

Role of higher order dispersion in the Faraday instability

In the previous chapter we deliberately designed a cavity where a single instability tongue is induced by the modulation of the dispersion inside the cavity. However, we have seen in Chap. 2 that a periodic dispersion can, in principle, destabilize an infinite number of sidebands in the optical spectrum. In this chapter we report the experimental study of a new cavity whose design aims at observing a large number of parametric "Faraday" sidebands as a consequence of dispersion management. To exacerbate the parametric modulation instabilities, the cavity is pumped close to a ZDW, thus requiring the inclusion of higher order dispersion terms into the model to properly describe the system. Indeed, it is well known that in fibers (in the single-pass configuration) with small β_2, the MI process is affected by higher order dispersion (HOD) terms. For example, the fourth order dispersion (FOD, β_4) can extend the range of existence of MI

to the normal dispersion regime [148–150]. In periodic dispersion fibers, the impact of β_4 is also significant: It can either produce new sidebands in the spectrum [43] or suppress the MI process [40]. HOD terms have been found at the origin of numerous effects in cavities as well. Recent studies have shown, for instance, that the first HOD term (β_3) is responsible for the emergence of convective and absolute instabilities [151], the asymmetry observed in intracavity MI spectrum [145] or short pulses spectrum [152]. β_3 also impacts the stability of Kerr frequency combs triggered by MI in both fiber cavities and microresonators [153]. Contrary to odd dispersion terms like β_3 that mostly influence the nonlinear stage of the instability, even terms, and especially β_4, drastically impact the linear stage of MI. For instance, It has been predicted that a positive value of FOD can greatly modify the unstable frequencies in photonic crystal fiber-ring cavities with anomalous dispersion [154]. Very recently, we demonstrated experimentally that a negative value of β_4 is responsible for the generation of new high-frequency sidebands in the spectrum of a uniform fiber-ring cavity pumped in the weak normal dispersion regime [155]. It is thus legitimate to think that the FOD will play a significant role regarding the parametric MI process taking place in our dispersion oscillating fiber-ring cavities.

In the first section, we describe how the theoretical model developed in Sec. 2.2 for the calculation of the parametric gain in longitudinally modulated cavities can be completed to take into account the effect of higher order dispersion terms. We specifically emphasise how the FOD plays a major role in the shape of the gain spectrum. We then detail in Sec. 5.2 the dispersion profile of the cavity that we have studied. Secs. 5.3 and 5.4 are devoted to experimental results. First, we show how we used the DFT technique to record the complex spectral dynamics associated to the simultaneous emergence of multiple Faraday sidebands. Finally, we demonstrate how we were able to observe all the Faraday sidebands in excellent agreement with theory, by driving the cavity with short bursts of pulses.

5.1 Theoretical aspect

The purpose of this section is to present how higher order dispersion can affect the parametric MI gain spectrum, especially in regions where the GVD is weak. The regime of weak GVD is particularly interesting because it exacerbates the impact of the longitudinal modulation of the dispersion, that is to say, the Faraday instability. We first complete the previously described analytical model to include the frequency dependence of the GVD of the resonator. We then focus on the effect of FOD which is the first higher order dispersion term that remarkably alters the gain spectrum of the Faraday instability.

5.1.1 Extension to higher order dispersion

We start by considering the generalized version of the LL equation (1.21):

$$i\frac{\partial E}{\partial z}+\sum_{q=2}^{N}\frac{i^q\beta_q(z)}{q!}\frac{\partial^q E}{\partial \tau^q}+\gamma|E|^2E=i\frac{\theta}{L}E_{in}+\left(\frac{\delta_0}{L}-i\frac{\alpha}{L}\right)E \tag{5.1}$$

where $\beta_q(z)$ is the longitudinal profile of the dispersion of order q along the ring of length L. We can perform the linear stability analysis of Eq. (5.1) relative to the ansatz $E(z,t)=\sqrt{P_s}+[u(z,t)+iv(z,t)]$ similarly to what has been presented in Sec. 2.1.1. We recall that P_s is the intracavity steady-state power and u,v are real functions describing the perturbation applied to the steady-state. When introducing the Fourier transforms in time $[\hat{u}(z,\omega)=\int u(z,t)e^{i\omega t}dt]$ and $[\hat{v}(z,\omega)=\int v(z,t)e^{i\omega t}dt]$, the linearised system now takes the following form:

$$\frac{d}{dz}\begin{pmatrix}\hat{u}\\ \hat{v}\end{pmatrix}=\begin{pmatrix}-\left(\frac{\alpha}{L}+i\zeta\right) & -g(\omega,z)\\ h(\omega,z) & -\left(\frac{\alpha}{L}+i\zeta\right)\end{pmatrix}\begin{pmatrix}\hat{u}\\ \hat{v}\end{pmatrix} \tag{5.2}$$

where only odd order dispersion terms appear in ζ and where g and h are recasted to include every even order dispersion terms:

$$\begin{cases}\zeta=\sum\limits_{q=1}^{\infty}\dfrac{\beta_{2q+1}(z)}{(2q+1)!}\omega^{2q+1},\\ g(z)=\sum\limits_{q=1}^{\infty}\dfrac{\beta_{2q}(z)}{(2q)!}\omega^{2q}+\gamma P_s-\dfrac{\delta_0}{L},\\ h(z)=\sum\limits_{q=1}^{\infty}\dfrac{\beta_{2q}(z)}{(2q)!}\omega^{2q}+3\gamma P_s-\dfrac{\delta_0}{L}\end{cases} \tag{5.3}$$

From Eqs. (5.2) and (5.3), the same approach as the one developed in Sec. 2.2 can by followed. In our case, we limit the expansion up to the fourth order term β_4 (i.e. $N=4$ in Eq. (5.1)) since higher orders do not significantly impact the behaviour of the system (This has been checked *a posteriori*). The Faraday instability still appears under parametric resonance conditions which is now expressed for the m^{th} resonance as follows:

$$\left(\frac{\beta_2^{av}\omega^2}{2}+\frac{\beta_4^{av}\omega^4}{24}+2\gamma P_s-\frac{\delta_0}{L}\right)^2-\gamma^2P_s^2=\left(\frac{m\pi}{\Lambda}\right)^2 \tag{5.4}$$

where β_2^{av} and β_4^{av} are the average second and fourth order dispersion terms. It is then straightforward to find the angular frequencies that fulfil these resonance conditions:

$$\omega_{F,m} = \pm\sqrt{-6\frac{\beta_2^{av}}{\beta_4^{av}} \pm 2\sqrt{9\left(\frac{\beta_2^{av}}{\beta_4^{av}}\right)^2 + \frac{6}{\beta_4^{av}}\left\{\pm\sqrt{\left(\frac{m\pi}{\Lambda}\right)^2 + \gamma^2 P_s^2} + \left(\frac{\delta_0}{L} - 2\gamma P_s\right)\right\}}} \tag{5.5}$$

This expression should be compared to Eq. (2.15) (recalled below for convenience), which has been derived for the same system without taking account of β_4:

$$\omega_{F,m} = \sqrt{\left\{\frac{2}{\beta_2^{av}}\left(\frac{\delta_0}{L} - 2\gamma P_s\right)\right\} \pm \left[\frac{2}{\beta_2^{av}}\sqrt{\left(\frac{m\pi}{L}\right)^2 + (\gamma P_s)^2}\right]} \tag{5.6}$$

We will see later that the frequencies predicted by Eqs. (5.6) and (5.5) are nearly identical, except in the vicinity of the average ZDW λ_0^{av} (when β_2^{av} is weak). We also repeat here for convenience the expression of the most unstable frequency for the Turing instability (derived considering a uniform cavity):

$$\omega_T = \sqrt{\frac{2}{\beta_2}\left(\frac{\delta_0}{L} - 2\gamma P_s\right)} \tag{5.7}$$

In a fashion quite similar to what we have described in Sec. 2.2.2, if we consider that the ring cavity is composed of two pieces of uniform fiber, a and b, of length L_a and L_b spliced together, then the growth rate, or gain $G(\omega)$ can be calculated according to the following set of expressions:

$$\begin{cases} G(\omega) = \ln(\max|\sigma^{\pm}|)/L, \\ \sigma^{\pm} = \dfrac{D}{2} \pm \sqrt{\dfrac{D^2}{4} - \exp\left[-2\left(\frac{\alpha}{L} + i\zeta\right)L\right]}, \\ D = \exp\left[-\left(\frac{\alpha}{L} + i\zeta\right)L\right] \cdot \left[2\cos(k_a L_a)\cos(k_b L_b) - \dfrac{g_a h_b, + g_b h_a}{k_a k_b}\sin(k_a L_a)\sin(k_b L_b)\right], \\ k_{a,b} = \sqrt{g_{a,b} h_{a,b}} \end{cases} \tag{5.8}$$

where *a (b)* refers to the *fiber a (b)*.

5.1.2 Impact of the fourth order dispersion on the gain spectrum

In this section, we perform a general numerical study of the influence of β_4 on the MI gain spectrum based on the previously derived expressions (Eqs. (5.8)). We computed the gain for a cavity composed of two uniform fibers of equal length (i.e. $L_a = L_b = L/2$). The difference of GVD between the two fibers is considered constant $\beta_2^b(\lambda) - \beta_2^a(\lambda) = 10\,\mathrm{ps}^2/\mathrm{km}$. We consider the system to be in the bistable regime ($\Delta = 4$) with steady-state set on the upper branch of the cavity response ($P_s = 7.8\,\mathrm{W}$). For uniform

cavities, this branch is modulationally unstable in the average anomalous dispersion regime with the characteristic frequency given by Eq. (5.7), and stable in the average normal dispersion regime (see Fig. 2.1 on page 30). To clearly highlight the influence of β_4 on the gain spectrum, we contrast in the two following paragraphs simulations done without and with the inclusion of this term.

- $\beta_4 = 0$:

Let us first neglect the FOD Fig. (5.1). The evolution of the GVD of each fiber composing the cavity is represented in Fig. 5.1(a) as a function of the wavelength and shows the ZDW of each of the fiber, λ_0^a and λ_0^b respectively. The average dispersion of the cavity is plotted in black and lies in between the two previous curves and the resulting average ZDW is $\lambda_0^{av} = (\lambda_0^a + \lambda_0^b)/2$. Figure 5.1(c) displays a 2D color plot of the gain spectrum (y-axis) as a function of the pump wavelength (x-axis) calculated from Eqs. (5.8). For $\lambda \ll \lambda_0^a$ (left of the figure), the average dispersion is normal and the spectrum exhibits only one pair of weak sidebands. When increasing the pump wavelength, the number of bands grows, is maximum for $\lambda = \lambda_0^a$, and then decreases until no sidebands exists in the vicinity of λ_0^{av}. The position of each sideband corresponds to a solution of Eq. (5.6) for $m \neq 0$. For example, the calculated position for the $m = 1$ condition is superimposed as dashed green lines (Note that we don't plot the positions related to other sidebands for the sake of clarity). For longer pump wavelengths the average dispersion becomes anomalous. Again, several pairs of sidebands emerge and when $\lambda = \lambda_0^b$, a large number of bands appear in a fashion similar to the case ($\lambda = \lambda_0^a$) described above. Then, less and less sidebands exist as the wavelength is further increased above λ_0^b. The main difference between the average normal and average anomalous dispersion regions is the pair of broad, low frequency and high gain bands that can be seen in the anomalous regime. These bands are associated to the Turing instability that occurs upon the upper branch of the bistable curve for average anomalous dispersion, as it can be inferred from the agreement with the predictions of Eq. (5.7) (superimposed as dashed blue lines), which gives the position of the MI sidelobes in the case of constant dispersion. As a qualitative comparison, the experiments reported in Chap. 4 in a different cavity were performed at a fixed pump wavelength which lied between λ_0^a and λ_0^{av}, and more precisely, in the region where a single pair of Faraday sidebands is observed.

In order to get a clearer insight of what occurs when λ lies in the vicinity of one of the ZDW of the cavity, a closer view of the region around λ_0^a (rotated by 90° anticlockwise for convenience) is plotted in Fig. 5.1(d). The gain spectrum exhibits more and more sidebands as λ approaches λ_0^a as highlighted in Figs. 5.1(e-g), which show three specific spectra. For $\lambda = \lambda_0^a$, an infinite number of sidebands are destabilized with almost the same gain (Fig. 5.1(e)). This latter observation results from the exact cancellation of the dispersion operator of one of the fibers for that specific pump wavelength and is thus

not physically meaningful. Indeed in regions of low dispersion (i.e. in the vicinity of a ZDW), HOD terms become significant and cannot be neglected any more. In the next paragraph we thus consider a realistic configuration taking account of the FOD.

- $\beta_4 = \beta_4^{av} = -1 \times 10^{-3}\,\mathrm{ps}^4/\mathrm{km}$:

Numerical results obtained when considering the FOD are presented in Fig. 5.2, which keeps the same structure as Fig. 5.1. In this example β_4 is negative and constant all along the length of the cavity. Note that β_3 and more generally odd order dispersion terms do not play any role in the gain [156]. Figure 5.2(a) represents the dispersion of each fiber as a function of the wavelength and Fig. 5.2(b) the bistable response of the cavity. It appears from Fig. 5.2(c) that the gain spectrum is influenced by β_4 mostly in the vicinity of the ring's ZDWs (i.e. when the dispersion is locally low) and remains the same otherwise. It can also be pointed out that the predicted positions of the sidebands by Eq. (5.5) (in dashed green lines) is essentially the same as when $\beta_4 = 0$. Figure 5.2(d) shows a close-up view of the region around λ_0^a as in Fig. 5.1(d) and clearly illustrates the strong modification of the gain spectrum under the influence of β_4. Indeed, the branches that tend toward infinite frequencies in Fig. 5.1(d) are now curved toward lower wavelengths. At the ZDW of *fiber a* (λ_0^a), the gain spectrum is now limited to a rather narrow range of frequencies and the number of sidebands becomes finite (Fig. 5.2(e)). For shorter pump wavelengths, the gain spectrum is also significantly modified by the presence of β_4. Indeed, new high frequency *clusters* of sidebands appear. For wavelengths just slightly shorter than λ_0^a (Fig. 5.2(f)), these *clusters* are still connected to the lowest frequency sideband pairs (which are nearly unaffected by β_4) and form a rather broad spectrum. But for even shorter wavelengths (Fig. 5.2(g)), they eventually form detached high frequency *clusters*. Note that the same observation stands around the ZDW of *fiber b* (λ_0^b) in the average anomalous GVD region (see Fig. 5.2(c)).

The existence of the high frequency *cluster* is thus due to the FOD and its spectral position can be calculated by noting that it is solely driven by the even dispersion coefficients (β_2 and β_4) of the locally low dispersion fiber section (*fiber a* in the case of Fig. 5.2(d-g)). The expression for this position is simply obtained by dropping the contribution of the dispersion modulation in Eq. (5.5) and is equivalent to the one obtained in Ref. [155]:

$$\omega_{FOD} = \pm\sqrt{-6\frac{\beta_2^a}{\beta_4^a} \pm 2\sqrt{9\left(\frac{\beta_2^a}{\beta_4^a}\right)^2 + \frac{6}{\beta_4^a}\left(\frac{\delta_0}{L} - 2\gamma P_s\right)}}. \tag{5.9}$$

This frequency is reported in Fig. 5.2(d) as dashed black lines and coincide exactly

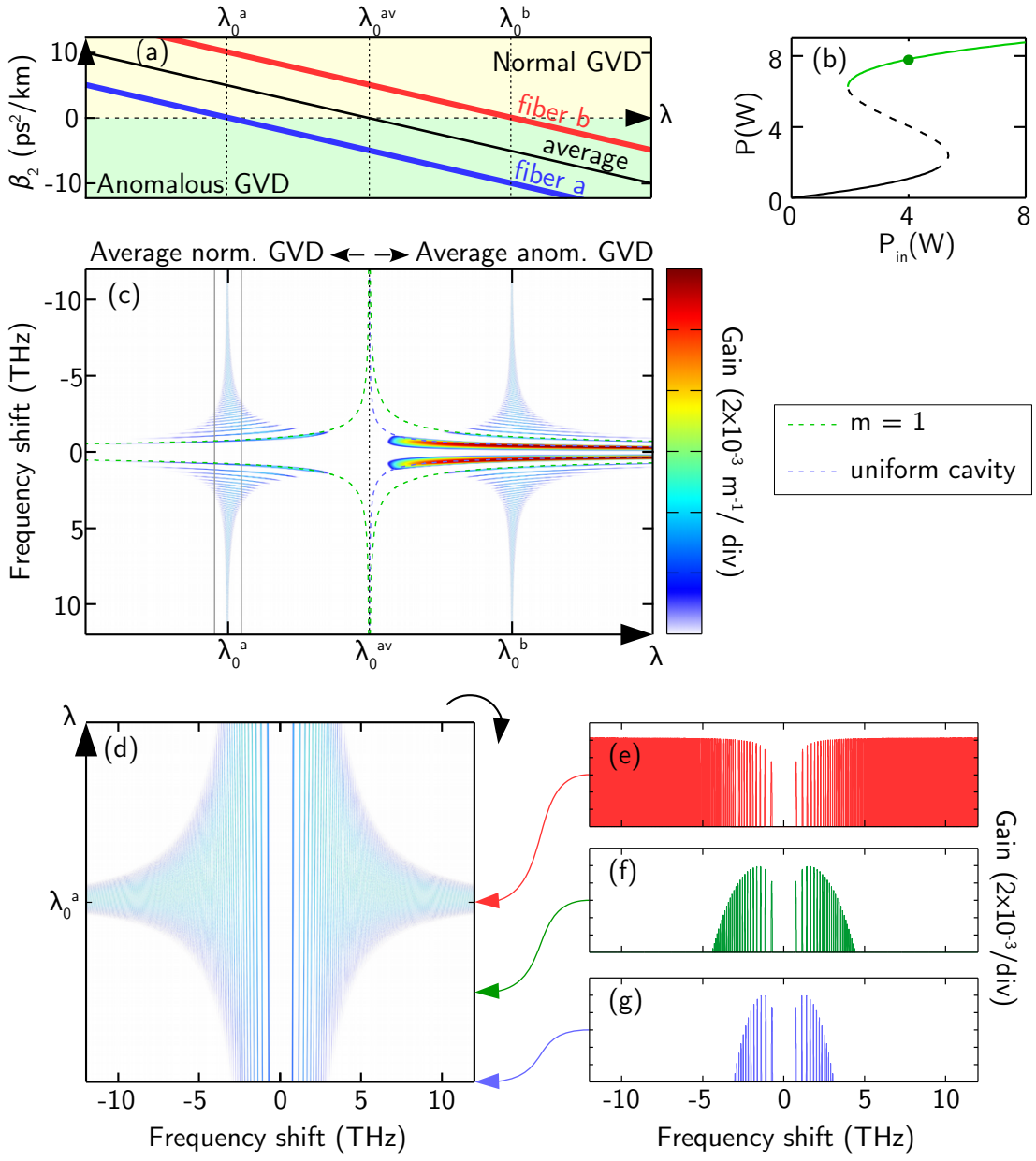

Figure 5.1 – Faraday instability with only GVD: (a) Evolution of the GVD as a function of the pump wavelength λ for the two fibers composing the ring. (b) Bistable response of the cavity, the operating point is marked by a green bullet. (c) 2D color plot of the gain spectrum as a function of the pump wavelength. The theoretical position of the first sidebands calculated from Eq. (5.6) in green and Eq. (5.7) in blue are superimposed. (d) Close-up view of (c) in the vicinity of λ_0^a (rotated by 90 ° anticlockwise). (e-g) Gain spectra for 3 pump wavelengths indicated by coloured arrows in (d). $\beta_4 = 0\,\mathrm{ps}^4/\mathrm{km}$, $L = 43\,\mathrm{m}$.

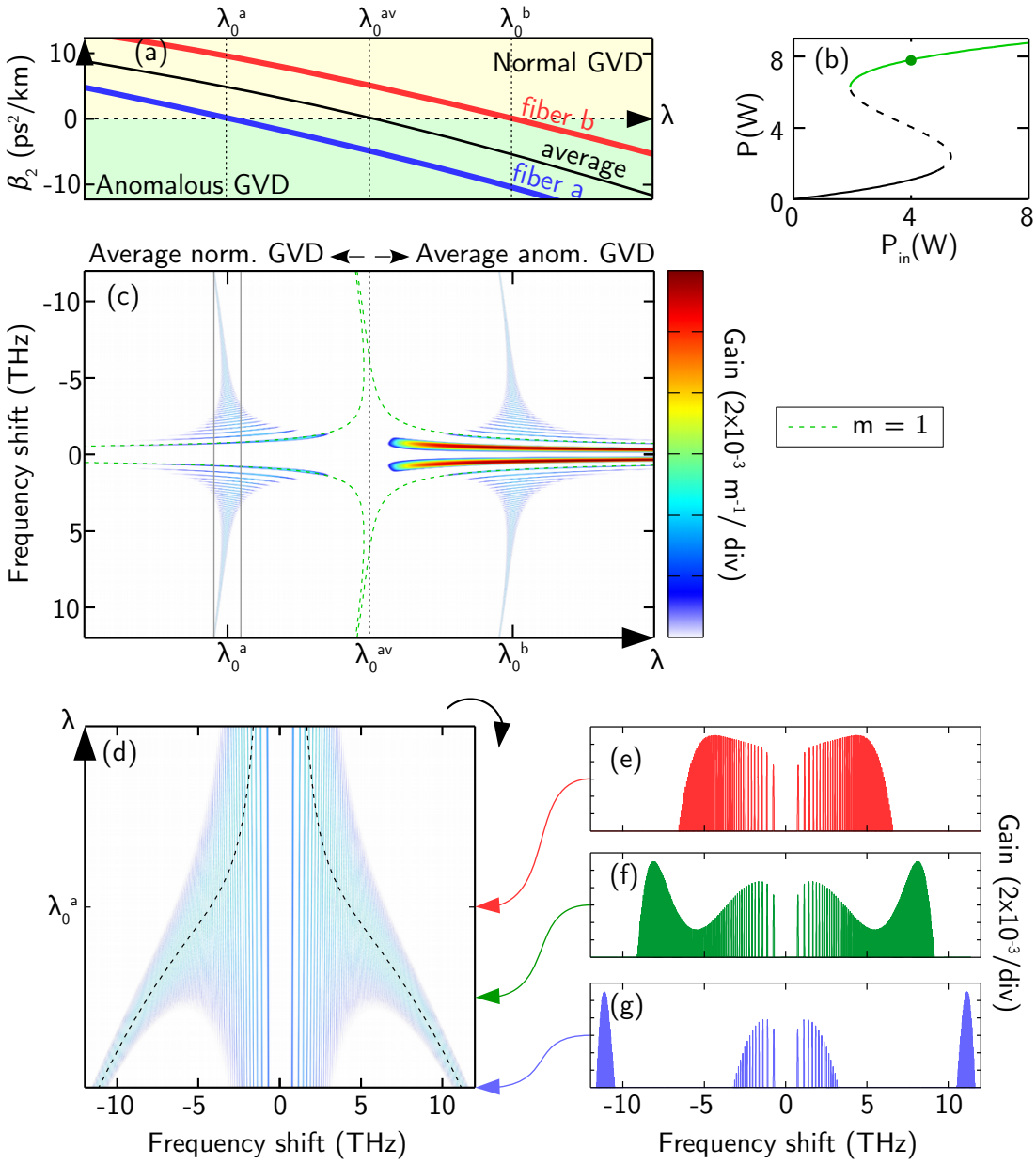

Figure 5.2 – Faraday instability when accounting for the FOD: Same configuration as Fig. 5.1. (c) The theoretical position of the sidebands for $m = 1$ calculated from Eq. (5.5) is superimposed in green. (d) The position of the FOD branches calculated from Eq. (5.9) is highlighted by dashed black lines. $\beta_4 = -1 \times 10^{-3}\,\mathrm{ps}^4/\mathrm{km}$, $L = 43\,\mathrm{m}$.

with the maximum of the envelope of the spectrum.

In the next section, we describe the dispersion profile of the fiber-ring cavity that we built. This latter aimed to confirm the theoretical predictions that we have made in the current section, namely the emergence of a large number of parametric (Faraday) spectral sidebands very dependent of the pump wavelength.

5.2 Design of the cavity and setup

The ring cavity that we designed is depicted in Fig. 5.3(a). It is composed of 22.6 m of dispersion shifted fiber (DSF) with a ZDW $\lambda_0^a = 1551.05\,\text{nm}$ (*fiber a*) and 20.5 m of dispersion compensating fiber (DCF) (*fiber b*). The evolution of the GVD as a function of the wavelength is represented in Fig. 5.3(b) for the two fibers. The range of pump wavelength accessible in the experiment (limited by the pump laser) is shaded and corresponds to a small region below λ_0^a. In this region, the cavity operates in the average normal dispersion regime. Consequently, all the predicted sidebands exhibit a parametric MI gain of the same order of magnitude (see the previous discussion and Fig. 5.2(d)) which facilitate their observation as opposed to the region around λ_0^b where the first pair of Turing sidebands has a gain six times larger than the others. Figures 5.3(c, d) display the longitudinal profile of the second and fourth order dispersions β_2 and β_4 respectively along the length of the cavity.

We can see that, for the range of pump wavelength investigated, both fibers exhibit normal dispersion with a nearly constant difference ($\beta_2^b - \beta_2^a \approx 10\,\text{ps}^2/\text{km}\ \forall\ \lambda$). Note that a greater (smaller) gap of dispersion between the two fibers would have led to a higher (lower) average dispersion and would have thus decreased (increased) the spacing between the sidebands. Furthermore, *fiber a* exhibits a very low GVD in this region which will emphasise the effect of β_4. The two fibers are characterized by FODs of respectively $\beta_4^a = -1 \times 10^{-3}\,\text{ps}^4/\text{km}$ and $\beta_4^b = 1.38 \times 10^{-3}\,\text{ps}^4/\text{km}$ which yields $\beta_4^{av} \approx 1.3 \times 10^{-4}\,\text{ps}^4/\text{km}$, and the nonlinearity is estimated to be $\gamma = 2.5$ /W/km for both fibers. We measured a finesse of 18 and thus estimate the overall losses to be $\alpha \approx 0.17$. For all the following experiments, the detuning was fixed to $\pi/4.5\,\text{rad}$, which leads to a normalized detuning $\Delta = \delta_0/\alpha = 4 > \sqrt{3}$, that is to say the cavity was driven in the bistable regime. We recall that for this set of parameters, only the upper branch of the bistable cycle undergoes an instability (Faraday) since the system cannot exhibit stable Turing pattern on the lower branch unless $\Delta > 4.25$ [68].

The setup used for these experiments is schematically depicted in Fig. 5.4. Concerning the pump beam, the main difference with the experiments described in the previous chapter is the repetition rate of the train of 400 –ps-long pulses which has been set to 4.74 MHz to fit with the round-trip time of the 43.1 –m-long ring cavity. Also, in

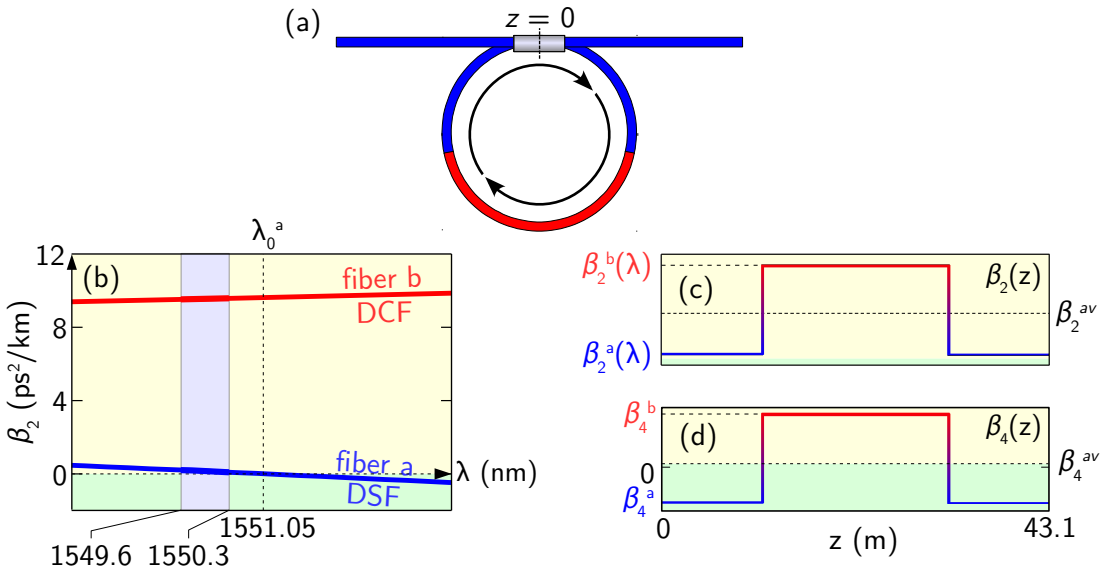

Figure 5.3 – Dispersion profile of the longitudinally modulated cavity. (a) Sketch of the designed cavity. (b) GVD as a function of the wavelength for the two fibers which constitutes the ring cavity. The shaded region corresponds to the accessible range of pump wavelength. Longitudinal profile of (c) β_2 and (d) β_4 along the length of the cavity.

these experiments we changed the pump wavelength between different recordings in the range 1549.6 – 1550.3 nm. The pump wavelength is adjusted through thermal tuning of the laser such that up to one minute is needed between successive recordings to make sure the system has achieved equilibrium.

The rest of this chapter is dedicated to the experimental results obtained in this cavity using the two complementary acquisition methods: (i) the DFT method for round-trip-to-round-trip recordings of the output spectrum (used in Sec. 5.3); (ii) the OSA for average recordings (used in Sec. 5.4).

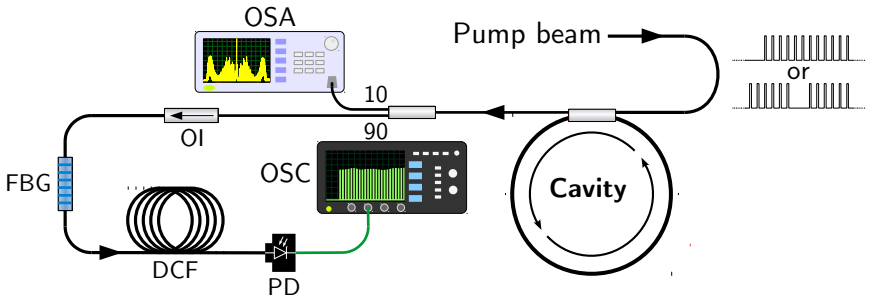

Figure 5.4 – Sketch of the experimental setup for the recording of both single-shot (DFT) and averaged (OSA) spectra.

5.3 Observation of the competition between multiple parametric sidebands

The regime of instability we investigate is characterized by tens of spectral sidebands. It is important to emphasize here that the theoretical spectra shown so far in Figs. 5.1 and 5.2 are gain spectra which do not take into account wave mixing between the different gain bands. The consequence of such a potential parasitic wave mixing, favoured by the weak dispersion value of the cavity, is that the output spectra, when a steady-state is reached, is not likely to contain all the predicted gain bands. In this section, we provide experimental results concerning the real-time spectral dynamics of the system, confirming the strong impact of the competition between the different parametric sidebands.

5.3.1 Transition to a stationary regime

By means of the DFT method (see Sec. 3.3.2 for details) we were able to record the dynamical evolution of the output spectrum. We launched pulses of 4 W peak power such that the system lies on the upper branch of the bistable curve and thus undergoes the Faraday instability. The pump wavelength was set to 1550.3 nm, which is the closest to λ_0^a (1551.05 nm) that we could achieve. Under these conditions, the theoretical gain spectrum is similar to the one illustrated in Fig. 5.2(f) and features high frequency clusters of sidelobes connected to lower frequency sidelobes. Figure 5.5(b) shows an experimental recording of the evolution of the optical spectrum at the output of the cavity during the 1500 round-trips following the turning on of the laser. The plot of the spectrum is restricted to one side of the pump for the sake of clarity.

It appears from this 2D color plot that the system goes through a transient regime, which lasts nearly 800 round-trips. First, multiple sidebands appear around round-trip No. 150 and we can identify the low frequency components (range $0-4$ THz) and the cluster of sidebands (range $6-8$ THz). Note that the rather large noise level of the DFT setup prevent us from revealing the weakest sidebands which are expected to appear between 4 and 6 THz. After round-trip No. 500, the cluster has completely vanished and some low frequency sidebands persist until round-trip No. 800. After that, only 4 sidebands (corresponding to $m = 1, 2, 5$ and 6) "survive" and persist as long as the driving field is sustained (although we recorded this steady spectrum for more than 6000 round-trips, we report a truncated version for the sake of clarity). Two snapshots at round-trips Nos. 1500 and 400 are plotted in Figs. 5.5(a) and 5.5(c) respectively, clearly illustrating the fact that the optical spectrum transiently exhibits a very large number of parametric bands. Note that the most detuned bands corresponding to the

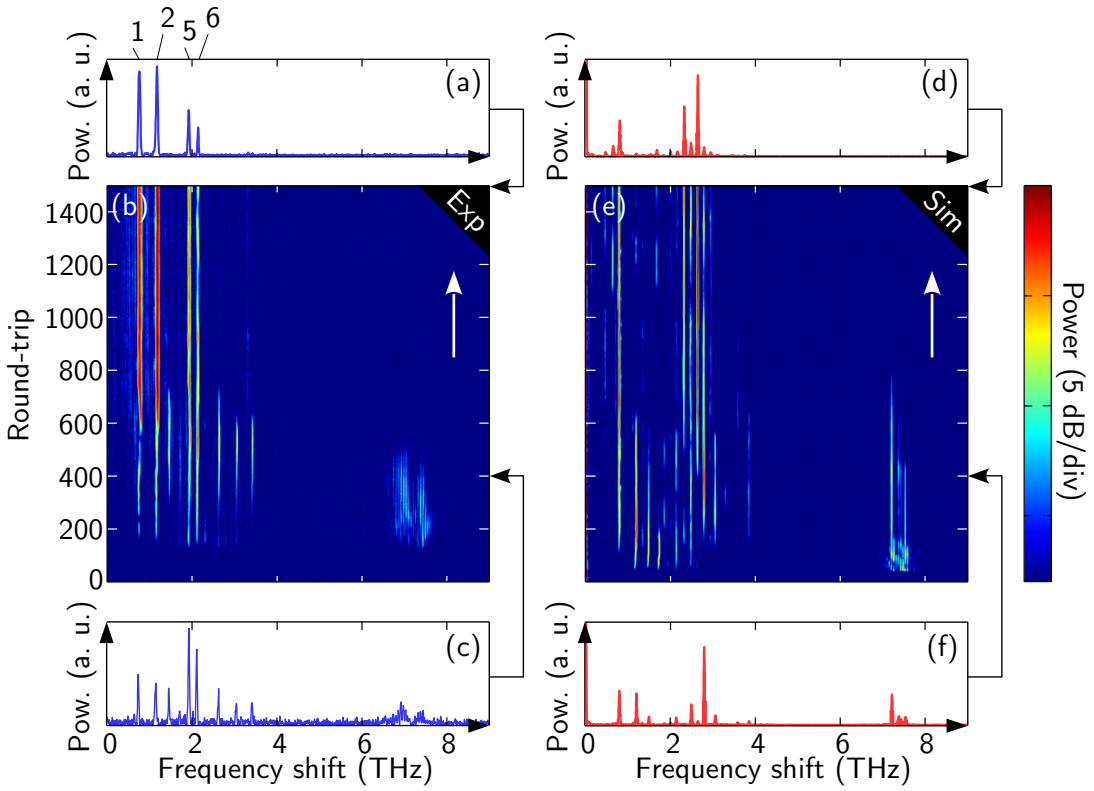

Figure 5.5 – Build-up dynamics of the Faraday instability spectrum in the weak dispersion regime. (b) 2D color logarithmic plot of the real-time evolution of the spectrum for the first 1500 round-trips of a burst. The beginning of the burst corresponds to the round-trips No. 0. (a, c) Snapshots of (b) for roundtrips Nos. 1500 and 400 respectively. (d-f) Corresponding numerical simulations of the LLE (Eq. (5.1)). The Stokes side of the spectrum is not shown for clarity.

cluster are the most attenuated by the DFT setup.

We carried out numerical simulations of the LL model (Eq. (5.1)) with dispersion terms up to β_4, and the results are plotted in Fig. 5.5(d-f) for comparison. The main features are well reproduced with a comparable timescale: emergence of numerous lobes followed by the vanishing of the cluster and of other lobes before a stable spectrum sets in. These results constitute a clear evidence of a competition scenario driven by the parametric MI gain.

A perfect quantitative agreement is not achieved in Fig. 5.5 because the parametric MI is a noise-seeded process. We will see this in greater details in the next subsection.

5.3.2 Influence of the random noise conditions

The randomness of initial conditions is known to significantly alter the dynamical behaviour of fundamental effects such as the MI or the underlying generation of supercontinuum [128, 129, 157]. In the cavity configuration, the stochastic nature of the driving field leads to the spontaneous formation of patterns and thus plays a critical role in the dynamics of the system.

In our case, we observed that the random noise conditions strongly affect the transitory regime of the system when the pump laser is turned on. To illustrate this, we show in Fig. 5.6(a) three consecutive experimental recordings of the evolution of the optical spectrum for 450 round-trips after the laser is turned on. Quite remarkably we can see that, although these recordings share some great similarities, they all differ from each other by the lobes that appear and vanish. To get a clearer insight, we plot in Fig. 5.6(b) the spectrum at round-trip No. 400 for the three experimental recordings. This clearly emphasize that the system can exhibit a great variety of states at the same stage of the process. Note that we limited ourselves to three samples for clarity, but that the experiment has been done a very large number of times and always led to a different outcome. Nevertheless, after 1500 round-trips the same stable state is eventually reached (not shown here). For comparison, Fig. 5.6(c) shows the outcome of three numerical simulations of Eq. (5.1) after 400 round-trips, each realization only differing from the other by the random noise conditions. Three drastically different spectra are obtained in agreement with our experiments, thus confirming the preponderant role of the random noise in the early-stage of the parametric process.

We have confirmed experimentally in this section that multiple Faraday resonances can be observed in the longitudinally modulated cavity that we designed. However, the strong impact of the competition between the different sidelobes and of the randomness of the noise conditions together with the low sensitivity of the DFT setup prevented us from obtaining a single-shot observation of all the predicted parametric resonances. In the next section, we circumvent these issues by implementing a new pumping scheme based on a standard OSA, thus performing an averaging and benefiting from an increased sensitivity.

5.4 Detection of all the parametric sidebands

The noise-seeded nature of the Faraday instability in our experiments is responsible for the transient spontaneous emergence of a large number of sidebands in the optical spectrum. However, for a single run of the experiment, only a subset of all the theoretical sidebands appear. Consequently, we came to the conclusion that an exhaustive image of

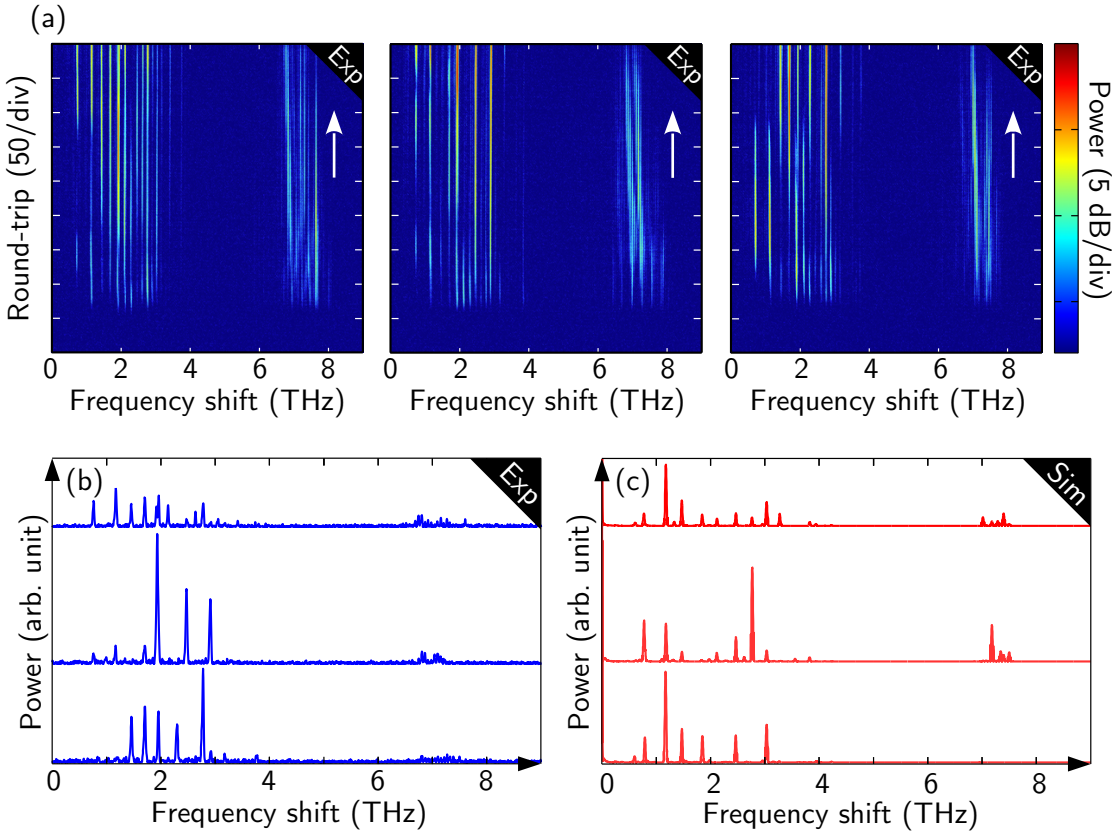

Figure 5.6 – Impact of the random noise conditions on the dynamics of the Faraday regime with multiple resonances. (a) Three different recordings of the transient evolution of the spectrum after the laser is turned on. (b) Spectra after 400 round-trips for the three previous recordings. (c) Corresponding numerical simulations of the LLE (Eq. (5.1)). The Stokes side of the spectrum is not shown for clarity.

the gain cannot be obtained through a single-shot recording of the optical spectrum at the output of the cavity. We have thus decided to resort to average recordings, which will give a statistical overview of the parametric MI spectrum. In order to do this, we used an OSA whose acquisition time is far greater than the timescale over which the parametric process occurs. Nevertheless, a particular attention has to be paid to the driving of the cavity. Indeed, the detrimental wave mixing between the sidebands still needs to be mitigated to obtain comprehensible results (wave mixing is not taken into account when calculating the gain spectrum). One way to do so is to reduce the power of the quasi-phase-matched (QPM) sidebands as it is known that the wave mixing is less effective when the power of the frequency components is low. To achieve this, we propose an original pumping technique that we labelled *short burst pumping* which is illustrated in Fig. 5.7.

It consists in periodically turning off the coherent driving of the cavity before the

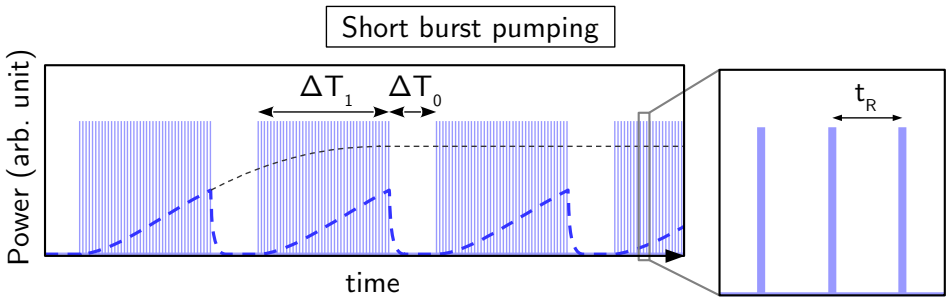

Figure 5.7 – Principle of the *short burst pumping* technique. The input pump pulses are in light blue and a sketch of the corresponding signal power is represented by a dashed blue line. The evolution of the signal power when the driving field is not turned off after the first burst is reported as a dashed black curve for comparison. Inset: zoom on the input pulses during a burst for three consecutive round-trips.

QPM sidebands reach a power level for which wave mixing is detrimental. When the driving field is on, the power of the sidebands (signal power) grows (see the dashed blue line) and when it is turned off, the power decays exponentially as the cavity empties itself. For comparison, the evolution of the signal power if the driving field is not turned off is sketched as a dashed black line. The *on* and *off* durations were adjusted experimentally: ΔT_1 is the largest value for which wave mixing is not too detrimental, thus maximising the signal power while circumventing the wave mixing issue. Accordingly, ΔT_1 was set to 100 µs (475 pulses) which corresponds to the time range when most of the Faraday sidebands transiently appear in the spectrum (see Fig. 5.5(b)). The dead time ΔT_0 was set just long enough to ensure that each burst acts as an independent run of the experiment: each burst experiencing different noise conditions, they will each result in a unique transitory regime (see Fig. 5.6(a)). In our case, ΔT_0 was set to 10 µs.

As we have already pointed out, it typically takes a few seconds to record an OSA trace which corresponds to hundreds of thousands of consecutive bursts in our case. The spectra presented in the following are therefore average representations of the dynamics of the cavity at the early-stage of the parametric amplification.

5.4.1 Average optical spectrum vs. gain spectrum

First, we applied the short burst pumping technique for the same pump wavelength and peak power as previously ($\lambda = 1550.3$ nm, $P_{in} = 4$ W). For this pump wavelength, we know from the previous results that the instability spectrum spans ≈ 16 THz or 130 nm (see Figs. 5.5 and 5.6). We performed the OSA recording with the best spectral resolution available (i.e. 4 GHz). Accordingly, it took around 80 s to obtain a full spectrum. We reemphasise here that it covers more than 700,000 bursts of input pulses.

The outcome of this recording is plotted in Fig. 5.8(a). The spectrum indeed features a huge number of sharp sideband pairs symmetrically located around the pump. It exhibits a very large intensity dynamics with nearly 50 dB of contrast between the weakest and the strongest bands. Note the reduced visibility of the bands in the clusters around ±7 THz which is likely due to the fact that, in this spectral region, the spacing between adjacent bands becomes closer to the resolution of the OSA. The corresponding analytical gain spectrum calculated from Eqs. (5.8) is plotted in Fig. 5.8(b). We find a remarkable resemblance with the experimental recording in its shape, especially with the predicted clusters of bands induced by the FOD which are clearly distinguishable. We were able to identify in the experimental recording of Fig. 5.8(a) 87 pairs of sidebands which correspond to the first 87 Faraday resonances of Eq. (5.5). To illustrate this, the positions of 10^{th} and 65^{th} sidelobes are marked by vertical arrows. Figure 5.8(c) displays the position of each sideband as a function of its order m for both the experiments and the analytics. It highlights that the bands get closer to each other as m increases as expected from Eq. (5.5). As can be seen, a perfect agreement between theory and experiment is obtained for the positions of the 87 pairs of sidebands. Finally, we can point out that the envelope of the spectrum in the experiment is relatively smooth except for the intensities of the first sidebands (roughly up to $m = 10$) which seem more uneven. This can be seen as the premises of the spurious wave mixing which eventually occurs as we discussed earlier. Indeed, we verified that this effect is reduced when the duration of the bursts is shortened. However in that case, we don't observe the weakest sidelobes as a counterpart. The result presented in Fig. 5.8(a) is thus the best trade-off that we found between visibility of the sidebands and smoothness of the envelope.

5.4.2 Impact of the pump wavelength

After the confirmation that our *short burst pumping* allows us to obtain a clear image of the Faraday gain spectrum, we applied this technique to confirm that the shape of this spectrum greatly depends on the pump wavelength as we predicted in our analytical investigation (see Fig. 5.2(d)). To do so, we reiterated the previous recording of the spectrum at the output of the cavity for different pump wavelengths. The result is given as a 2D color plot in Fig. 5.9(a). Note that our experimental setup allowed us to span only a relatively narrow range of pump wavelength (0.7 nm) below the ZDW λ_0^a. Nevertheless, this range is very relevant as regards the impact of the pump wavelength on the instability spectrum. In agreement with our theoretical study, we clearly observed the shifting of the clusters toward higher frequency as the pump wavelength is decreased below λ_0^a (1551.05 nm). For $\lambda = 1550.3$ nm, the spectrum

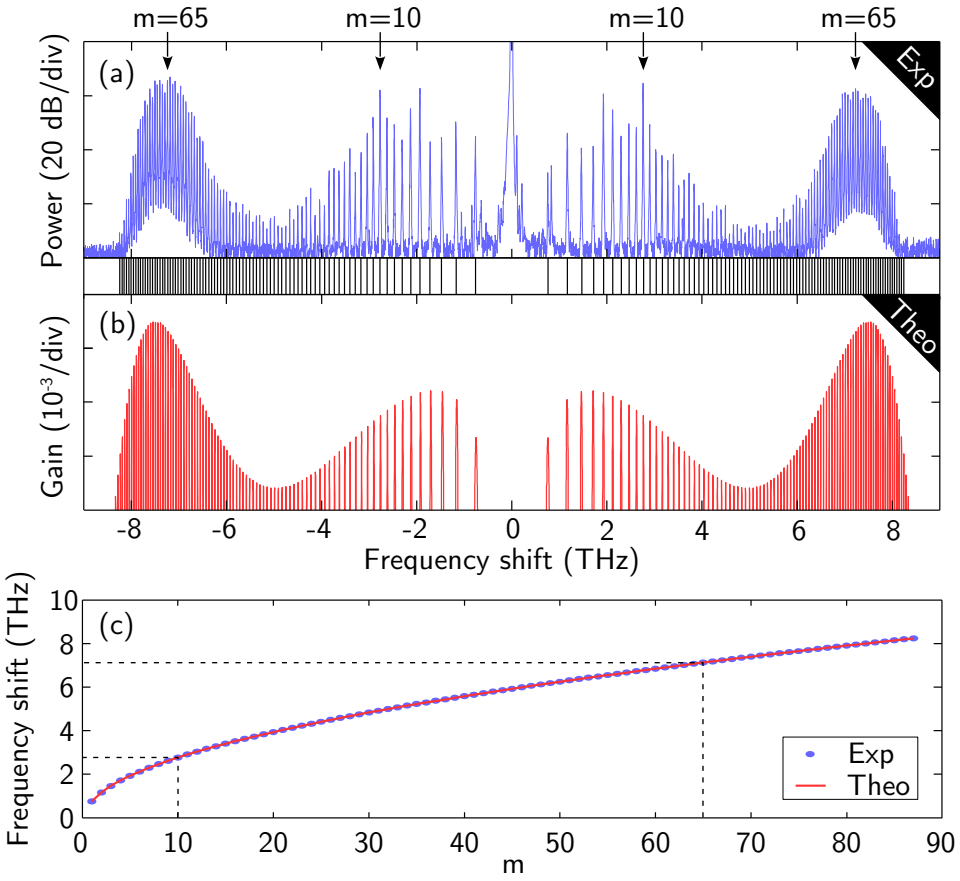

Figure 5.8 – (a) Average experimental spectrum featuring 87 pairs of Faraday sidebands. (b) Corresponding theoretical gain spectrum calculated from Eqs. (5.8). (c) Spectral positions of the sidebands as a function of their order m both experimentally and theoretically. Sidelobes Nos. 10 and 65 are identified in (a) for clarity. $\lambda = 1550.3\,\text{nm}$

exhibits a quasi-continuum of sidebands as described in details in Fig. 5.8 but when we decrease the pump wavelength, the high-frequency clusters are not connected any more to the low frequency components. The position of the clusters is in excellent agreement with the predictions of Eq. (5.9) (superimposed as dashed black lines) calculated as if the cavity was made of a single piece of *fiber a*. Figure 5.9(b) shows 8 spectra picked along Fig. 5.9(a) in order to better appreciate these results, which qualitatively agree with the theoretical behaviour described in Fig. 5.2(d-g). The position of each pair of sidebands corresponds to a fulfilled parametric resonance condition (Eq. (5.4)). We were thus able to associate each peak to its order m up to 125 in the spectrum at the bottom (i.e. shortest pump wavelength).

To conclude, we have shown in this section that by appropriately tuning the field at the input of the longitudinally modulated cavity and by averaging the spectrum at the

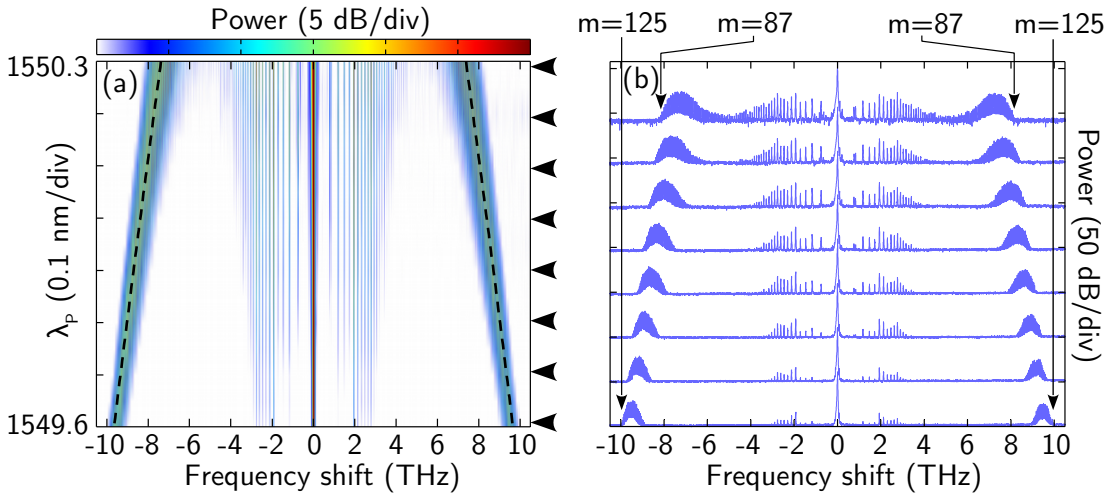

Figure 5.9 – (a) 2D color plot of the experimental evolution of the Faraday instability spectrum as a function of the pump wavelength. The analytically estimated position of the high frequency branch (Eq. (5.9)) is superimposed as dashed black lines. 8 spectra along this figure (indicated by the black triangles on the right side) are reported in (b) for clarity. The positions and orders of the high-frequency cut-off sidebands are highlighted by arrows for the first and last spectrum.

output, it is possible to observe a very large number of parametric "Faraday" resonances. This method gives a statistical overview of the dynamics of the early-stage of the process in excellent concordance with the analytical gain spectrum. Using this method, we were able to experimentally confirm the predicted dependence of the spectrum with the pump wavelength, especially concerning the spectral positions of the FOD induced high-frequency clusters of sidebands.

5.5 Summary

- We have provided an extended version of the analytical model for the calculation of the parametric MI gain in longitudinally modulated cavities accounting for higher orders of dispersion.
- In the case of a cavity with piecewise constant dispersion, we have shown that the FOD drastically alters the gain spectrum in regions of weak dispersion. Indeed, close to a ZDW, the spectrum exhibits a very large number of Faraday resonances whose intensities strongly depend on the FOD and the pump wavelength.
- We implemented a new cavity to investigate this regime and, by means of the DFT technique, we recorded the emergence of multiple Faraday spectral bands. Using this technique to reveal the spectral dynamics of the system, we found that at the early-stage of the parametric process, a wave mixing occurs between the different resonances leading to a stable state featuring a limited number of bands. Also, we observed that the randomness of the noise conditions strongly affects the transient regime of the system. These observations are all corroborated by numerical simulations of the LLE.
- We introduced an original pumping scheme that we labelled *short burst pumping* which, when coupled to a standard OSA, allows to record average spectra of the dynamics of the system with a high sensitivity. By launching bursts of pulses of tunable duration inside the cavity, the predicted Faraday resonances can be detected thanks to the strong averaging realized by the OSA.
- The *short burst pumping* technique provides recordings in excellent agreement with analytical gain spectra with up to 87 pairs of Faraday sidebands observed in a single spectrum. We experimentally addressed the impact of the pump wavelength on the instability spectrum using this averaging technique and we confirmed our analytical predictions: high-frequency clusters of sidebands induced by the FOD appear at frequencies strongly dependent of the pump wavelength.

Conclusion

During this thesis, we studied passive optical fiber-ring resonators whose chromatic dispersion is longitudinally modulated. Specifically, we focused our attention on the regime of parametric modulation instability, which is induced by the dispersion management. In this dissertation, we detailed the theoretical analysis of this kind of system and our experimental demonstrations of the different predicted features of this regime of instability. The main results presented in this manuscript are summarized hereunder.

• We studied the stability of the steady-state homogeneous solutions of the cavity with respect to a weak harmonic perturbation. In a uniform cavity, this stability analysis is known to predict the occurrence of intracavity modulation instability often referred to as *Turing instability*. On the other side, in a longitudinally modulated cavity, we found that the periodic variation of dispersion encountered by light over successive round-trips acts as a forcing which can destabilize the system through the generation of multiple parametric resonances in the optical spectrum [78]. This regime is analogous to the well-known hydrodynamical *Faraday instability* [114]. Interestingly enough, Turing and Faraday mechanisms can appear in the same cavity, the first one being governed by the average characteristics of the system, and the second one by their longitudinal evolution. Depending on the sign of the average dispersion, we predicted two different scenarios: When the average dispersion is anomalous, the two instabilities coexist, whereas they can appear for distinct powers when the average dispersion is normal and the system operated in the bistable regime. We considered the latter configuration in all of our experiments because it allows to excite independently each instability by simply tuning the pump power, and thus, to investigate their characteristics. We found that the round-trip-to-round-trip evolution of the temporal pattern generated through the Faraday mechanism can follow a period-doubling dynamics. We derived an analytical model for the calculation of the gain spectrum in the case of a piecewise constant dispersion. This particular profile turns out to be the easiest to implement experimentally.

• We have unarguably demonstrated the occurrence of both Turing and Faraday instabilities in the same modulated cavity by the observation of sidebands in the optical spectrum at frequencies characteristic of each mechanism. Thanks to an active stabilisation device of the round-trip phase accumulation, we managed to operate the cavity under steady conditions which allowed us to switch between the two instability regimes by a simple tuning of the input power. Turing and Faraday instabilities occuring upon distinct transmission branches of the cavity, the optical bistability and underpinning hysteresis inherent to such Kerr cavity have been confirmed in an original way by the abrupt change in the position of the spectral sidebands when jumping from one branch to the other [79]. By means of the dispersive Fourier transform technique, we were able to record the round-trip-to-round-trip dynamics of the system in the spectral domain. We used this technique to reveal the spontaneous emergence and saturation of the intensity of the unstable modes inside the cavity. The transient behaviour of the system when suddenly increasing the power has been addressed and features clear signatures of bistable switching [80]. In the time domain, we were able to confirm the period doubling dynamics associated to the Faraday regime in our cavity through real-time direct measurements of the temporal waveform. The acquisition of such traces was made possible thanks to a temporal imaging system which allowed us to resolve the ultra-fast temporal pattern generated through both the Turing and Faraday mechanisms.

• Under weak dispersion conditions, we demonstrated that the contribution of the longitudinal modulation of the dispersion is exacerbated. As a consequence, an increased number of parametric "Faraday" sidebands can be observed in the optical spectrum. We found that the fourth order dispersion drastically affects the system by inducing a strong dependence of the gain spectrum on the pump wavelength. Our experimental investigation of the dynamics of the spectrum in such configuration revealed a striking competition between the different spontaneously generated Faraday resonances mediated by the random noise conditions. By performing an averaging of the optical spectrum over a very large number of experimental realisations, we managed to detect the occurrence of all the predicted parametric sidelobes with a record number of 87 pairs in a single spectrum. Using this same method, we experimentally investigated the influence of the pump wavelength and confirmed the existence of fourth order dispersion induced clusters of sidebands whose frequency shift is widely tunable [81].

The work described in this thesis naturally presents some potential lines of developments:

■ First, one might be interested in the field of temporal cavity solitons mentioned

in the introduction, which has attracted a tremendous attention over the recent years, motivated by the fact that they underpin the generation frequency combs that are at the basis of numerous applications [75–77]. These persisting dissipative structures, can be generated both in fiber-ring cavities [71, 158, 159] and microresonators [72–74]. In a longitudinally modulated resonator, such cavity solitons will perceive the variation of the dispersion as a perturbation which induces a periodic behaviour [160] and we can imagine an interplay between the Faraday mechanism and the potential emission of dispersive waves [161, 162]. Concerning the generation of frequency combs, a recent study proved that the Faraday instability, that we highlighted in this dissertation, can also trigger the formation of Kerr combs in dispersion managed microresonators with promising capacities [163].

■ Another topic that could be addressed is the generation of shock waves or switching waves in the normal dispersion regime of modulated cavities. In uniform resonators, switching waves are known to connect the two states of the bistable response of the cavity with or without the contribution of the Turing process [164, 165]. In our case, we can imagine a scenario where Turing and Faraday instabilities occur simultaneously but on distinct temporal locations in the resonator, connected by a mechanism that remains to be determined.

■ As for the experimental aspect, we can think of several interesting investigations that could be performed with some upgrades of our detection setup: with an improved resolution of the DFT setup, one should be able to record the real-time spontaneous emergence of the instabilities down to the longitudinal modes of the cavity. This would further emphasise the stochastic nature of the instability processes [128]. On another note, the round-trip-to-round-trip evolution of both the phase and amplitude of the instability sidebands could be recorded thanks to a heterodyne detection method that we have very recently successfully implemented in the context of the FPU recurrence in the single-pass configuration of uniform fibers [166, 167]. This will allow for a complete characterisation of the dynamics of the cavity, especially in the chaotic regime, by the reconstruction of the attractors of the system [65].

■ We should also mention one of our studies which appears in Appendix A, that is nearing completion at the time of writing this dissertation, concerning the emergence of convective and absolute regimes of instability induced by the pulse synchronisation mismatch of the cavity [151].

An important part of this PhD project has been the implementation of a reliable and scalable experimental setup, which continues to be used and improved to perform other observations like the influence of the fourth order dispersion on the MI process in uniform fiber cavities [155] (work of Florent Bessin, PhD started in October 2016).

"Sometimes I'll start a sentence and I don't even know where it's going. I just hope I find it along the way"

— Michael Scott in *The Office*

APPENDIX A

Influence of a synchronization mismatch on the Turing instability

One source of drift in a fiber-ring cavity comes from odd order terms in the Taylor expansion of the propagation constant $\beta(\omega)$, which break the reflection symmetry of the LL equation [145, 151, 168]. The first and third order dispersion terms (β_1 and β_3) are the most likely to have a significant impact. On one side, when the cavity exhibits a weak dispersion ($\beta_2 \approx 0$) β_3 needs to be taken into account. On the other side, when the cavity is pumped by a train of pulses, if the period of the pulse train does not match the round-trip time of the cavity, then there exists a walk-off between the input pulses and the intracavity pulse. When the system experiences modulation instabilities, this walk-off is responsible for the linear drift of the generated temporal pattern. The synchronization mismatch can be accounted for in the LL equation by including the gradient term $\Delta\beta_1 \partial E/\partial\tau$ [88, 168]:

$$i\frac{\partial E}{\partial z} + i\Delta\beta_1\frac{\partial E}{\partial \tau} - \frac{\beta_2}{2}\frac{\partial^2 E}{\partial \tau^2} + \gamma|E|^2E = i\frac{\theta}{L}E_{in} + \left(\frac{\delta_0}{L} - i\frac{\alpha}{L}\right)E \tag{A.1}$$

with

$$\Delta\beta_1 = \frac{\Delta T}{L} \qquad \Delta T = t_R - t_{R,0} \tag{A.2}$$

where t_R is the period of the input pulse train and $t_{R,0} = nL/c$ is the round-trip time of the cavity.

Using the time lens system described in Sec. 3.3.3, we were able to directly record for the first time to our knowledge, the formation of stable temporal patterns induced by MI in a uniform fiber-ring cavity, with a particular emphasis on the impact of the synchronization mismatch. We also found that the latter is translated in the spectral domain by a modification of the position of the instability sidebands, which allows to monitor the synchronization of the device.

For these experiments, we built a uniform fiber-ring cavity made of SMF-28 with a 95/5 coupler. In practice, the synchronization mismatch is tuned by slightly changing the length of the resonator thanks to the fiber stretcher embedded in the cavity while

keeping the repetition rate of the pulses fixed. In Fig. A.1(a), we present 5 recordings of the emergence of stable temporal modulations obtained for different values of synchronization mismatch. Accordingly, the evolution of the modulation appears more or less tilted. Note that we managed to reduce the synchronization mismatch to a value as low as −10 fs/round-trip, or equivalently −0.5 ps/km. Also, we point out that from the recording on the left ($\Delta\beta_1 = -14$ ps/km) to the one on the right ($\Delta\beta_1 = 19$ ps/km) the length of the cavity differs by less than 150 µm.

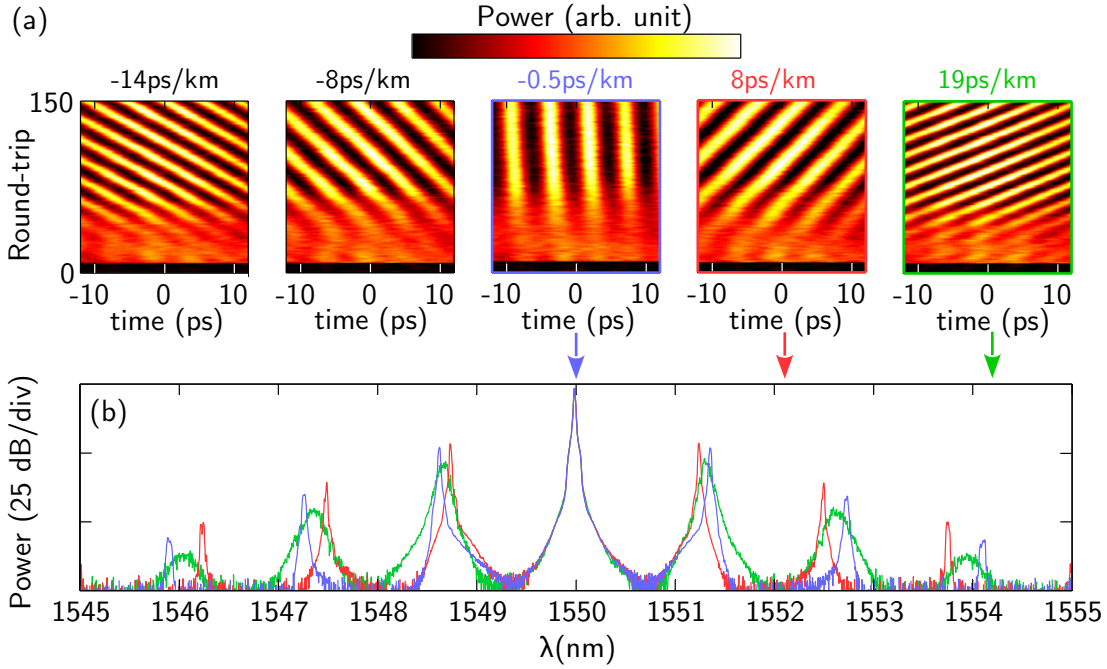

Figure A.1 – (a) Experimental recordings of the formation of Turing temporal patterns for increasing values of synchronization mismatch in a uniform fiber-ring cavity. From left to right, $\Delta\beta_1$ is varied from −14 to 19 ps/km, The laser is turned on at round-trip No. 15. (b) Stable spectra from OSA at the output of the cavity for three values of synchronization mismatch. $L = 21.7$ m, $\beta_2 \approx -20$ ps^2/km, $\gamma = 1.23$ /W/km, $P_{in} = 5$ W, $\delta_0 \approx 0.22$ rad, $\mathcal{F} \approx 25$.

For each temporal recording, we simultaneously recorded the output spectrum with an OSA. We superimpose 3 of them corresponding to $\Delta\beta_1 = -0.5,\ 8$ and 19 ps/km in Fig. A.1(b). Interestingly, we observed a significant dependence of the position of the MI sidelobes with the mismatch. This behaviour cannot be interpreted through the standard linear stability analysis which, we remind, only involves even order dispersion terms. To further investigate this experimentally, we switched to another method for generating the pump pulses, which allows for an extremely precise control of the period of the pulse train (≈ 1.7 fs), while keeping the length of the cavity fixed. We then recorded the spectrum for values of mismatch ranging from −80 to 120 ps/km. The result is plotted in Fig. A.2(a). We clearly observed that the spectrum is symmetrical with respect to null synchronization mismatch (the slight "scale discrepancy" between positive and negative values of mismatch can be imputed to a slow drift of the input power and cavity length

in the course of the recording). When the mismatch exceeds a certain level in absolute value, the sidebands are broad and when it is even further increased, they eventually vanish. By looking closely at the spectrum for rather small synchronization mismatches, we clearly see that the sidebands are sharp and that their position significantly change with the value of the mismatch (see Fig. A.2(b)). This is even more evident when looking at the harmonics of the primary sidebands. Such observation of the modification of the sidebands frequency induced by the walk-off between input pulses and intracavity pulse has, to the best of our knowledge, never been reported so far.

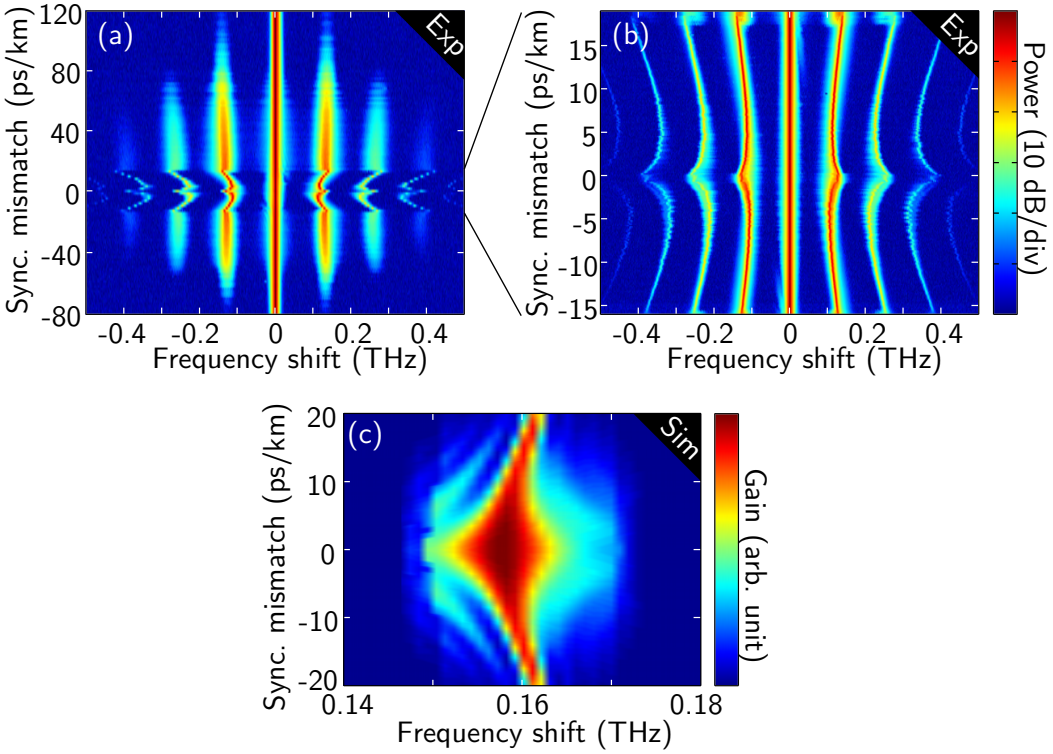

Figure A.2 – (a) Experimental recording of the evolution of the MI spectrum as a function of the value of the synchronization mismatch. (b) Close-up view on the region of small mismatch. (c) Numerical simulation of the gain spectrum from the LL model (Eq. (A.1)) $L = 10.2\,\mathrm{m}$, $\beta_2 \approx -20\,\mathrm{ps}^2/\mathrm{km}$, $\gamma = 1.23\,/\mathrm{W/km}$, $P_{in} \approx 0.5\,\mathrm{W}$, $\delta_0 \approx 0.22\,\mathrm{rad}$, $\mathcal{F} \approx 50$.

Numerical simulations of the gain spectrum from Eq. (A.1) confirm that the position of the primary sidebands is indeed affected by the drift term, as can be seen in the preliminary results plotted in Fig. A.2(c). At the time of writing, we are collaborating with Majid Taki and Saliya Coulibaly from the PhLAM laboratory (experts in theoretical nonlinear optics) to develop a theoretical framework for these observations.

To conclude, we have observed the temporal drifting of MI induced train of pulses, as a consequence of a synchronization mismatch of the cavity, and noted a spectral signature of this phenomenon. These observations have been useful to properly record the temporal dynamics of Turing and Faraday instabilities in longitudinally modulated cavities, but are also of fundamental interest in the investigation of absolute and convective instabilities in dissipative systems.

Bibliography

[1] C. V. Raman and K. S. Krishnan. "A New Type of Secondary Radiation". *Nature* 121 (1928), pp. 501–502 (cit. on p. 1).

[2] J. P. Gordon, H. J. Zeiger, and C. H. Townes. "Molecular Microwave Oscillator and New Hyperfine Structure in the Microwave Spectrum of NH3". *Physical Review* 95 (1) (1954), pp. 282–284 (cit. on p. 1).

[3] T. H. Maiman. "Optical and Microwave-Optical Experiments in Ruby". *Physical Review Letters* 4 (11) (1960), pp. 564–566 (cit. on p. 1).

[4] R. J. Collins. "Coherence, Narrowing, Directionality, and Relaxation Oscillations in the Light Emission from Ruby". *Physical Review Letters* 5 (7) (1960), pp. 303–305 (cit. on p. 1).

[5] P. A. Franken, A. E. Hill, C. W. Peters, and G. Weinreich. "Generation of Optical Harmonics". *Physical Review Letters* 7 (4) (1961), pp. 118–119 (cit. on p. 1).

[6] D. Keck and P. Schultz. "Method of producing optical waveguide fibers". US 3711262 A. 1973 (cit. on p. 1).

[7] R. H. Stolen, E. P. Ippen, and A. R. Tynes. "Raman Oscillation in Glass Optical Waveguide". *Applied Physics Letters* 20 (2) (1972), pp. 62–64 (cit. on p. 1).

[8] R. H. Stolen and E. P. Ippen. "Raman gain in glass optical waveguides". *Applied Physics Letters* 22 (6) (1973), pp. 276–278 (cit. on p. 1).

[9] E. Ippen and R. Stolen. "Stimulated Brillouin scattering in optical fibers". *Applied Physics Letters* 21 (11) (1972), pp. 539–541 (cit. on p. 1).

[10] R. H. Stolen and A. Ashkin. "Optical Kerr effect in glass waveguide". *Applied Physics Letters* 22 (6) (1973), pp. 294–296 (cit. on p. 1).

[11] R. H. Stolen, J. E. Bjorkholm, and A. Ashkin. "Phase-matched three-wave mixing in silica fiber optical waveguides". *Applied Physics Letters* 24 (7) (1974), pp. 308–310 (cit. on p. 1).

[12] R. H. Stolen. "Phase-matched-stimulated four-photon mixing in silica-fiber waveguides". *IEEE Journal of Quantum Electronics* 11 (3) (1975), pp. 100–103 (cit. on p. 1).

[13] R. H. Stolen and C. Lin. "Self-phase-modulation in silica optical fibers". *Physical Review A* 17 (4) (1978), pp. 1448–1453 (cit. on p. 1).

[14] A. Hasegawa and W. Brinkman. "Tunable coherent IR and FIR sources utilizing modulational instability". *IEEE Journal of Quantum Electronics* 16 (7) (1980), pp. 694–697 (cit. on p. 1).

[15] K. Tai, A. Hasegawa, and A. Tomita. "Observation of modulational instability in optical fibers". *Physical Review Letters* 56 (2) (1986), pp. 135–138 (cit. on pp. 1, 27).

[16] T. B. Benjamin and J. E. Feir. "The disintegration of wave trains on deep water Part 1. Theory". *Journal of Fluid Mechanics* 27 (03) (1967), pp. 417–430 (cit. on pp. 2, 27).

[17] T. Taniuti and H. Washimi. "Self-Trapping and Instability of Hydromagnetic Waves Along the Magnetic Field in a Cold Plasma". *Physical Review Letters* 21 (4) (July 1968), pp. 209–212 (cit. on pp. 2, 27).

[18] K. E. Strecker, G. B. Partridge, A. G. Truscott, and R. G. Hulet. "Formation and propagation of matter-wave soliton trains". *Nature* 417 (6885) (2002), pp. 150–153 (cit. on pp. 2, 27).

[19] A. Hasegawa. "Generation of a train of soliton pulses by induced modulational instability in optical fibers". *Optics Letters* 9 (7) (1984), pp. 288–290 (cit. on p. 2).

[20] J. Hansryd, P. Andrekson, M. Westlund, J. Li, and P. Hedekvist. "Fiber-based optical parametric amplifiers and their applications". *IEEE Journal of Selected Topics in Quantum Electronics* 8 (3) (2002), pp. 506–520 (cit. on pp. 2, 27).

[21] M. E. Marhic. *Fiber optical parametric amplifiers, oscillators and related devices*. OCLC: ocn154682254. Cambridge, UK ; New York: Cambridge University Press, 2008 (cit. on pp. 2, 27).

[22] D. R. Solli, C. Ropers, P. Koonath, and B. Jalali. "Optical rogue waves". *Nature* 450 (7172) (Dec. 2007), pp. 1054–1057 (cit. on p. 2).

[23] J. M. Dudley, F. Dias, M. Erkintalo, and G. Genty. "Instabilities, breathers and rogue waves in optics". *Nature Photonics* 8 (10) (Oct. 2014), pp. 755–764 (cit. on p. 2).

[24] N. Akhmediev, B. Kibler, F. Baronio, M. Belić, W.-P. Zhong, Y. Zhang, Wonkeun Chang, J. M. Soto-Crespo, P. Vouzas, P. Grelu, C. Lecaplain, K. Hammani, S. Rica, A Picozzi, M. Tlidi, K. Panajotov, A. Mussot, A. Bendahmane, Pascal Szriftgiser, G. Genty, J. Dudley, A. Kudlinski, A. Demircan, U. Morgner, Shalva Amiraranashvili, C. Bree, G. Steinmeyer, C. Masoller, N. G. R. Broderick, A. F. J. Runge, Miro Erkintalo, S. Residori, U. Bortolozzo, F. T. Arecchi, S. Wabnitz, C. G. Tiofack, S. Coulibaly, and M. Taki. "Roadmap on optical rogue waves and extreme events". *Journal of Optics* 18 (6) (2016), p. 063001 (cit. on p. 2).

[25] J. M. Dudley, G. Genty, and S. Coen. "Supercontinuum generation in photonic crystal fiber". *Reviews of Modern Physics* 78 (4) (2006), pp. 1135–1184 (cit. on pp. 2, 27).

[26] J. M. Dudley and J. R. Taylor, eds. *Supercontinuum generation in optical fibers*. OCLC: ocn456838616. Cambridge ; New York: Cambridge University Press, 2010 (cit. on pp. 2, 27).

[27] K. Tajima. "Compensation of soliton broadening in nonlinear optical fibers with loss". *Optics Letters* 12 (1) (1987), pp. 54–56 (cit. on p. 2).

[28] S. V. Chernikov and P. V. Mamyshev. "Femtosecond soliton propagation in fibers with slowly decreasing dispersion". *JOSA B* 8 (8) (1991), pp. 1633–1641 (cit. on p. 2).

[29] A. Kudlinski, A. K. George, J. C. Knight, J. C. Travers, A. B. Rulkov, S. V. Popov, and J. R. Taylor. "Zero-dispersion wavelength decreasing photonic crystal fibers for ultraviolet-extended supercontinuum generation". *Optics Express* 14 (12) (2006), pp. 5715–5722 (cit. on p. 2).

[30] A. Kudlinski, M. Lelek, B. Barviau, L. Audry, and A. Mussot. "Efficient blue conversion from a 1064 nm microchip laser in long photonic crystal fiber tapers for fluorescence microscopy". *Optics Express* 18 (16) (2010), pp. 16640–16645 (cit. on p. 2).

[31] F. Matera, A. Mecozzi, M. Romagnoli, and M. Settembre. "Sideband instability induced by periodic power variation in long-distance fiber links". *Optics Letters* 18 (18) (Sept. 1993), pp. 1499–1501 (cit. on p. 2).

[32] F. K. Abdullaev, S. A. Darmanyan, S. Bischoff, and M. P. Sørensen. "Modulational instability of electromagnetic waves in media with varying nonlinearity". *JOSA B* 14 (1) (1997), pp. 27–33 (cit. on p. 2).

[33] S. G. Murdoch, R. Leonhardt, J. D. Harvey, and T. a. B. Kennedy. "Quasi-phase matching in an optical fiber with periodic birefringence". *JOSA B* 14 (7) (1997), pp. 1816–1822 (cit. on p. 2).

[34] K. Kikuchi, C. Lorattanasane, F. Futami, and S. Kaneko. "Observation of quasi-phase matched four-wave mixing assisted by periodic power variation in a long-distance optical amplifier chain". *IEEE Photonics Technology Letters* 7 (11) (1995), pp. 1378–1380 (cit. on p. 2).

[35] F. K. Abdullaev, S. A. Darmanyan, A. Kobyakov, and F. Lederer. "Modulational instability in optical fibers with variable dispersion". *Physics Letters A* 220 (4–5) (1996), pp. 213–218 (cit. on p. 2).

[36] N. J. Smith and N. J. Doran. "Modulational instabilities in fibers with periodic dispersion management". *Optics Letters* 21 (8) (Apr. 1996), p. 570 (cit. on p. 2).

[37] J. C. Bronski and J. N. Kutz. "Modulational stability of plane waves in nonreturn-to-zero communications systems with dispersion management". *Optics Letters* 21 (13) (1996), pp. 937–939 (cit. on pp. 2, 38).

[38] S. Ambomo, C. M. Ngabireng, P. T. Dinda, A. Labruyère, K. Porsezian, and B. Kalithasan. "Critical behavior with dramatic enhancement of modulational instability gain in fiber systems with periodic variation dispersion". *Journal of the Optical Society of America B* 25 (3) (2008), pp. 425–433 (cit. on p. 2).

[39] A. Armaroli and F. Biancalana. "Tunable modulational instability sidebands via parametric resonance in periodically tapered optical fibers". *Optics Express* 20 (22) (Oct. 2012), pp. 25096–25110 (cit. on p. 2).

[40] A. Armaroli and F. Biancalana. "Suppression and splitting of modulational instability sidebands in periodically tapered optical fibers because of fourth-order dispersion". *Optics Letters* 39 (16) (2014), pp. 4804–4807 (cit. on pp. 2, 108).

[41] M. Droques, A. Kudlinski, G. Bouwmans, G. Martinelli, and A. Mussot. "Experimental demonstration of modulation instability in an optical fiber with a periodic dispersion landscape". *Optics Letters* 37 (23) (2012), pp. 4832–4834 (cit. on pp. 2, 3, 44, 51).

[42] M. Droques, A. Kudlinski, G. Bouwmans, G. Martinelli, and A. Mussot. "Dynamics of the modulation instability spectrum in optical fibers with oscillating dispersion". *Physical Review A* 87 (1) (2013), p. 013813 (cit. on pp. 2, 44, 51).

[43] M. Droques, A. Kudlinski, G. Bouwmans, G. Martinelli, A. Mussot, A. Armaroli, and F. Biancalana. "Fourth-order dispersion mediated modulation instability in dispersion oscillating fibers". *Optics Letters* 38 (17) (2013), pp. 3464–3467 (cit. on pp. 2, 108).

[44] X. Wang, D. Bigourd, A. Kudlinski, K. K. Y. Wong, M. Douay, L. Bigot, A. Lerouge, Y. Quiquempois, and A. Mussot. "Correlation between multiple modulation instability side lobes in dispersion oscillating fiber". *Optics Letters* 39 (7) (2014), pp. 1881–1884 (cit. on pp. 2, 66).

[45] F. Copie, A. Kudlinski, M. Conforti, G. Martinelli, and A. Mussot. "Modulation instability in amplitude modulated dispersion oscillating fibers". *Optics Express* 23 (4) (2015), pp. 3869–3875 (cit. on p. 2).

[46] S. R. Nodari, M. Conforti, G. Dujardin, A. Kudlinski, A. Mussot, S. Trillo, and S. De Bièvre. "Modulational instability in dispersion-kicked optical fibers". *Physical Review A* 92 (1) (2015), p. 013810 (cit. on pp. 2, 44).

[47] C. Finot, J. Fatome, A. Sysoliatin, A. Kosolapov, and S. Wabnitz. "Competing four-wave mixing processes in dispersion oscillating telecom fiber". *Optics Letters* 38 (24) (2013), pp. 5361–5364 (cit. on p. 2).

[48] C. Finot, F. Feng, Y. Chembo, and S. Wabnitz. "Gain sideband splitting in dispersion oscillating fibers". *Optical Fiber Technology* 20 (5) (2014), pp. 513–519 (cit. on p. 2).

[49] F. Feng, P. Morin, Y. K. Chembo, A. Sysoliatin, S. Wabnitz, and C. Finot. "Experimental demonstration of spectral sideband splitting in strongly dispersion oscillating fibers". *Optics Letters* 40 (4) (2015), pp. 455–458 (cit. on p. 2).

[50] C. Finot, A. Sysoliatin, and S. Wabnitz. "Nonlinear parametric resonances in quasiperiodic dispersion oscillating fibers". *Optics Communications* (2015) (cit. on p. 2).

[51] C. Finot and S. Wabnitz. "Influence of the pump shape on the modulation instability process induced in a dispersion-oscillating fiber". *JOSA B* 32 (5) (2015), pp. 892–899 (cit. on p. 2).

[52] A. Mussot, M. Conforti, S. Trillo, F. Copie, and A. Kudlinski. "Modulation instability in dispersion oscillating fibers". *Advances in Optics and Photonics* 10 (1) (Mar. 2018), pp. 1–42 (cit. on pp. 3, 44).

[53] K. Ikeda. "Multiple-valued stationary state and its instability of the transmitted light by a ring cavity system". *Optics Communications* 30 (2) (1979), pp. 257–261 (cit. on pp. 3, 15).

[54] K. Ikeda, H. Daido, and O. Akimoto. "Optical Turbulence: Chaotic Behavior of Transmitted Light from a Ring Cavity". *Physical Review Letters* 45 (9) (1980), pp. 709–712 (cit. on pp. 3, 47).

[55] K. Ikeda and O. Akimoto. "Instability Leading to Periodic and Chaotic Self-Pulsations in a Bistable Optical Cavity". *Physical Review Letters* 48 (9) (1982), pp. 617–620 (cit. on pp. 3, 47).

[56] H. M. Gibbs, F. A. Hopf, D. L. Kaplan, and R. L. Shoemaker. "Observation of Chaos in Optical Bistability". *Physical Review Letters* 46 (7) (1981), pp. 474–477 (cit. on pp. 3, 65).

[57] J. Goldstone and E. Garmire. "On the dynamic response of nonlinear Fabry-Perot interferometers". *IEEE Journal of Quantum Electronics* 17 (3) (1981), pp. 366–374 (cit. on pp. 3, 65).

[58] J. L. Jewell, H. M. Gibbs, S. S. Tarng, A. C. Gossard, and W. Wiegmann. "Regenerative pulsations from an intrinsic bistable optical device". *Applied Physics Letters* 40 (4) (1982), pp. 291–293 (cit. on pp. 3, 65).

[59] B. Wedding, A. Gasch, and D. Jäger. "Self-pulsing and transients of a Fabry–Perot interferometer with quadratic nonlinear medium". *Journal of Applied Physics* 54 (9) (1983), pp. 4826–4831 (cit. on pp. 3, 65).

[60] R. M. Shelby, M. D. Levenson, and S. H. Perlmutter. "Bistability and other effects in a nonlinear fiber-optic ring resonator". *JOSA B* 5 (2) (1988), pp. 347–357 (cit. on pp. 3, 59).

[61] R. Vallée. "Temporal instabilities in the output of an all-fiber ring cavity". *Optics Communications* 81 (6) (1991), pp. 419–426 (cit. on pp. 3, 16).

[62] M. Nakazawa, K. Suzuki, and H. A. Haus. "Modulational instability oscillation in nonlinear dispersive ring cavity". *Physical Review A* 38 (10) (1988), pp. 5193–5196 (cit. on pp. 3, 28, 37, 68).

[63] M. Haelterman, S. Trillo, and S. Wabnitz. "Dissipative modulation instability in a nonlinear dispersive ring cavity". *Optics Communications* 91 (5–6) (1992), pp. 401–407 (cit. on pp. 3, 18, 20, 21, 23, 28, 30, 79).

[64] M. Haelterman, S. Trillo, and S. Wabnitz. "Additive-modulation-instability ring laser in the normal dispersion regime of a fiber". *Optics Letters* 17 (10) (1992), pp. 745–747 (cit. on pp. 3, 18, 23, 28, 30, 35, 92).

[65] M. Haelterman, S. Trillo, and S. Wabnitz. "Low dimensional modulational chaos in diffractive nonlinear cavities". *Optics Communications* 93 (5) (1992), pp. 343–349 (cit. on pp. 3, 129).

[66] M. Haelterman, S. Trillo, and S. Wabnitz. "Polarization multistability and instability in a nonlinear dispersive ring cavity". *Journal of the Optical Society of America B* 11 (3) (1994), pp. 446–456 (cit. on pp. 3, 36).

[67] S. Coen and M. Haelterman. "Modulational Instability Induced by Cavity Boundary Conditions in a Normally Dispersive Optical Fiber". *Physical Review Letters* 79 (21) (1997), pp. 4139–4142 (cit. on pp. 3, 47, 57, 89).

[68] S. Coen, M. Haelterman, P. Emplit, L. Delage, L. M. Simohamed, and F. Reynaud. "Bistable switching induced by modulational instability in a normally dispersive all-fibre ring cavity". *Journal of Optics B: Quantum and Semiclassical Optics* 1 (1) (1999), p. 36 (cit. on pp. 3, 33, 34, 57, 79, 84, 89, 94, 115).

[69] S. Coen and M. Haelterman. "Competition between modulational instability and switching in optical bistability". *Optics Letters* 24 (2) (1999), pp. 80–82 (cit. on pp. 3, 16, 57, 79, 89).

[70] S. Coen and M. Haelterman. "Continuous-wave ultrahigh-repetition-rate pulse-train generation through modulational instability in a passive fiber cavity". *Optics Letters* 26 (1) (2001), pp. 39–41 (cit. on pp. 3, 68).

[71] F. Leo, S. Coen, P. Kockaert, S.-P. Gorza, P. Emplit, and M. Haelterman. "Temporal cavity solitons in one-dimensional Kerr media as bits in an all-optical buffer". *Nature Photonics* 4 (7) (2010), pp. 471–476 (cit. on pp. 3, 16, 56, 129).

[72] T. Herr, V. Brasch, J. D. Jost, C. Y. Wang, N. M. Kondratiev, M. L. Gorodetsky, and T. J. Kippenberg. "Temporal solitons in optical microresonators". *Nature Photonics* 8 (2) (2014), pp. 145–152 (cit. on pp. 3, 56, 129).

[73] E. Obrzud, S. Lecomte, and T. Herr. "Temporal solitons in microresonators driven by optical pulses". *Nature Photonics* advance online publication (2017) (cit. on pp. 3, 129).

[74] A. M. Weiner. "Frequency combs: Cavity solitons come of age". *Nature Photonics* 11 (9) (2017), pp. 533–535 (cit. on pp. 3, 129).

[75] P. Del'Haye, A. Schliesser, O. Arcizet, T. Wilken, R. Holzwarth, and T. J. Kippenberg. "Optical frequency comb generation from a monolithic microresonator". *Nature* 450 (7173) (2007), pp. 1214–1217 (cit. on pp. 3, 129).

[76] T. J. Kippenberg, R. Holzwarth, and S. A. Diddams. "Microresonator-Based Optical Frequency Combs". *Science* 332 (6029) (2011), pp. 555–559 (cit. on pp. 3, 4, 129).

[77] Y. K. Chembo. "Kerr optical frequency combs: theory, applications and perspectives". *Nanophotonics* 5 (2) (2016) (cit. on pp. 3, 129).

[78] M. Conforti, A. Mussot, A. Kudlinski, and S. Trillo. "Modulational instability in dispersion oscillating fiber ring cavities". *Optics Letters* 39 (14) (2014), pp. 4200–4203 (cit. on pp. 4, 37, 127).

[79] F. Copie, M. Conforti, A. Kudlinski, A. Mussot, and S. Trillo. "Competing Turing and Faraday Instabilities in Longitudinally Modulated Passive Resonators". *Physical Review Letters* 116 (14) (2016), p. 143901 (cit. on pp. 4, 37, 128).

[80] F. Copie, M. Conforti, A. Kudlinski, S. Trillo, and A. Mussot. "Dynamics of Turing and Faraday instabilities in a longitudinally modulated fiber-ring cavity". *Optics Letters* 42 (3) (2017), p. 435 (cit. on pp. 4, 128).

[81] F. Copie, M. Conforti, A. Kudlinski, S. Trillo, and A. Mussot. "Modulation instability in the weak dispersion regime of a dispersion modulated passive fiber-ring cavity". *Optics Express* 25 (10) (2017), pp. 11283–11296 (cit. on pp. 5, 128).

[82] A. W. Snyder and J. D. Love. *Optical Waveguide Theory*. OCLC: 852789587. Boston, MA: Springer US, 1984 (cit. on p. 10).

[83] Y. Tamura, H. Sakuma, K. Morita, M. Suzuki, Y. Yamamoto, K. Shimada, Y. Honma, K. Sohma, T. Fujii, and T. Hasegawa. "Lowest-Ever 0.1419-dB/km Loss Optical Fiber". *Optical Fiber Communication Conference Postdeadline Papers*. OSA, 2017, Th5D.1 (cit. on p. 10).

[84] G. P. Agrawal. *Nonlinear fiber optics*. Fifth edition. Amsterdam: Elsevier/Academic Press, 2013 (cit. on pp. 12, 59).

[85] K. J. Blow and D. Wood. "Theoretical description of transient stimulated Raman scattering in optical fibers". *IEEE Journal of Quantum Electronics* 25 (12) (1989), pp. 2665–2673 (cit. on p. 13).

[86] P. V. Mamyshev and S. V. Chernikov. "Ultrashort-pulse propagation in optical fibers". *Optics Letters* 15 (19) (1990), pp. 1076–1078 (cit. on p. 13).

[87] P. L. François. "Nonlinear propagation of ultrashort pulses in optical fibers: total field formulation in the frequency domain". *JOSA B* 8 (2) (1991), pp. 276–293 (cit. on p. 13).

[88] S. Coen, M. Tlidi, P. Emplit, and M. Haelterman. "Convection versus Dispersion in Optical Bistability". *Physical Review Letters* 83 (12) (1999), pp. 2328–2331 (cit. on pp. 14, 59, 89, 133).

[89] L. F. Stokes, M. Chodorow, and H. J. Shaw. "All-single-mode fiber resonator". *Optics Letters* 7 (6) (1982), pp. 288–290 (cit. on pp. 15, 17).

[90] J. K. Jang, M. Erkintalo, S. G. Murdoch, and S. Coen. "Ultraweak long-range interactions of solitons observed over astronomical distances". *Nature Photonics* 7 (8) (2013), pp. 657–663 (cit. on pp. 16, 17).

[91] M. Anderson, Y. Wang, F. Leo, S. Coen, M. Erkintalo, and S. G. Murdoch. "Coexistence of Multiple Nonlinear States in a Tristable Passive Kerr Resonator". *Physical Review X* 7 (3) (2017), p. 031031 (cit. on pp. 16, 20–22).

[92] C. Y. Yue, J. D. Peng, Y. B. Liao, and B. K. Zhou. "Fibre ring resonator with finesse of 1260". *Electronics Letters* 24 (10) (1988), pp. 622–623 (cit. on pp. 16, 56).

[93] S. Coen, M. Haelterman, P. Emplit, L. Delage, L. M. Simohamed, and F. Reynaud. "Experimental investigation of the dynamics of a stabilized nonlinear fiber ring resonator". *Journal of the Optical Society of America B* 15 (8) (1998), pp. 2283–2293 (cit. on pp. 17, 47, 57, 58, 60, 62, 99).

[94] Y. Wang, F. Leo, J. Fatome, M. Erkintalo, S. G. Murdoch, and S. Coen. "Universal mechanism for the binding of temporal cavity solitons". *Optica* 4 (8) (2017), pp. 855–863 (cit. on pp. 17, 66).

[95] A. Bendahmane, J. Fatome, C. Finot, G. Millot, and B. Kibler. "Coherent and incoherent seeding of dissipative modulation instability in a nonlinear fiber ring cavity". *Optics Letters* 42 (2) (2017), pp. 251–254 (cit. on pp. 17, 36).

[96] L. A. Lugiato and R. Lefever. "Spatial Dissipative Structures in Passive Optical Systems". *Physical Review Letters* 58 (21) (1987), pp. 2209–2211 (cit. on pp. 18, 20, 33).

[97] F. Copie, M. Conforti, A. Kudlinski, A. Mussot, F. Biancalana, and S. Trillo. "Instabilities in passive dispersion oscillating fiber ring cavities". *The European Physical Journal D* 71 (5) (2017), p. 133 (cit. on p. 18).

[98] T. Hansson and S. Wabnitz. "Frequency comb generation beyond the Lugiato–Lefever equation: multi-stability and super cavity solitons". *Journal of the Optical Society of America B* 32 (7) (2015), p. 1259 (cit. on pp. 20–22).

[99] Y. V. Kartashov, O. Alexander, and D. V. Skryabin. "Multistability and coexisting soliton combs in ring resonators: the Lugiato-Lefever approach". *Optics Express* 25 (10) (2017), pp. 11550–11555 (cit. on pp. 20–22).

[100] M. Conforti and F. Biancalana. "Multi-resonant Lugiato–Lefever model". *Optics Letters* 42 (18) (2017), pp. 3666–3669 (cit. on pp. 20–22).

[101] S. Coen. "Passive Nonlinear Optical Fiber Resonators Fundamentals and Applications". PhD thesis. Université Libre de Bruxelles, 1999 (cit. on pp. 21–23, 57, 58).

[102] V. E. Zakharov and L. A. Ostrovsky. "Modulation instability: The beginning". *Physica D: Nonlinear Phenomena* 238 (5) (2009), pp. 540–548 (cit. on p. 27).

[103] P. J. Everitt, M. A. Sooriyabandara, M. Guasoni, P. B. Wigley, C. H. Wei, G. D. McDonald, K. S. Hardman, P. Manju, J. D. Close, C. C. N. Kuhn, S. S. Szigeti, Y. S. Kivshar, and N. P. Robins. "Observation of a modulational instability in Bose-Einstein condensates". *Physical Review A* 96 (4) (2017), p. 041601 (cit. on p. 27).

[104] A. M. Turing. "The Chemical Basis of Morphogenesis". *Philosophical Transactions of the Royal Society of London B: Biological Sciences* 237 (641) (1952), pp. 37–72 (cit. on p. 28).

[105] G.-L. Oppo. "Formation and control of Turing patterns and phase fronts in photonics and chemistry". *Journal of Mathematical Chemistry* 45 (1) (2008), p. 95 (cit. on pp. 28, 37).

[106] G. Van Simaeys, P. Emplit, and M. Haelterman. "Experimental study of the reversible behavior of modulational instability in optical fibers". *Journal of the Optical Society of America B* 19 (3) (2002), pp. 477–486 (cit. on p. 35).

[107] A. Mussot, A. Kudlinski, M. Droques, P. Szriftgiser, and N. Akhmediev. "Fermi-Pasta-Ulam Recurrence in Nonlinear Fiber Optics: The Role of Reversible and Irreversible Losses". *Physical Review X* 4 (1) (2014), p. 011054 (cit. on p. 35).

[108] Z. Liu, S. Coulibaly, M. Taki, and N. Akhmediev. "Kerr frequency combs and triangular spectra". *Optics Letters* 42 (11) (2017), pp. 2126–2129 (cit. on pp. 36, 64).

[109] M. Tlidi, K. Staliunas, K. Panajotov, A. G. Vladimirov, and M. G. Clerc. "Localized structures in dissipative media: from optics to plant ecology". *Phil. Trans. R. Soc. A* 372 (2027) (2014), p. 20140101 (cit. on p. 37).

[110] K. Staliunas, C. Hang, and V. V. Konotop. "Parametric patterns in optical fiber ring nonlinear resonators". *Physical Review A* 88 (2) (2013), p. 023846 (cit. on pp. 37, 41, 78).

[111] N. Tarasov, A. M. Perego, D. V. Churkin, K. Staliunas, and S. K. Turitsyn. "Mode-locking via dissipative Faraday instability". *Nature Communications* 7 (2016), p. 12441 (cit. on pp. 37, 78).

[112] A. M. Perego, N. Tarasov, D. V. Churkin, S. K. Turitsyn, and K. Staliunas. "Pattern Generation by Dissipative Parametric Instability". *Physical Review Letters* 116 (2) (2016) (cit. on pp. 37, 78).

[113] I. Chavel. *Riemannian geometry: a modern introduction*. OCLC: 247562074. Cambridge University Press, 1996 (cit. on p. 39).

[114] M. Faraday. "On a Peculiar Class of Acoustical Figures; and on Certain Forms Assumed by Groups of Particles upon Vibrating Elastic Surfaces". *Phil. Trans. R. Soc. A* 121 (1831), pp. 299–340 (cit. on pp. 41, 127).

[115] K. Staliunas, S. Longhi, and G. J. de Valcárcel. "Faraday Patterns in Bose-Einstein Condensates". *Physical Review Letters* 89 (21) (2002), p. 210406 (cit. on p. 41).

[116] P. Engels, C. Atherton, and M. A. Hoefer. "Observation of Faraday Waves in a Bose-Einstein Condensate". *Physical Review Letters* 98 (9) (2007), p. 095301 (cit. on p. 41).

[117] C. Szwaj, S. Bielawski, D. Derozier, and T. Erneux. "Faraday Instability in a Multimode Laser". *Physical Review Letters* 80 (18) (1998), pp. 3968–3971 (cit. on p. 41).

[118] A. L. Lin, M. Bertram, K. Martinez, H. L. Swinney, A. Ardelea, and G. F. Carey. "Resonant Phase Patterns in a Reaction-Diffusion System". *Physical Review Letters* 84 (18) (2000), pp. 4240–4243 (cit. on p. 42).

[119] A. Kobyakov, M. Sauer, and D. Chowdhury. "Stimulated Brillouin scattering in optical fibers". *Advances in Optics and Photonics* 2 (1) (2010), pp. 1–59 (cit. on pp. 58, 59).

[120] S. Coen and M. Haelterman. "Impedance-matched modulational instability laser for background-free pulse train generation in the THz range". *Optics Communications* 146 (1–6) (1998), pp. 339–346 (cit. on p. 59).

[121] J. K. Jang and S. G. Murdoch. "Strong Brillouin suppression in a passive fiber ring resonator". *Optics Letters* 37 (7) (2012), p. 1256 (cit. on p. 59).

[122] L. F. Stokes, M. Chodorow, and H. J. Shaw. "All-fiber stimulated Brillouin ring laser with submilliwatt pump threshold". *Optics Letters* 7 (10) (1982), pp. 509–511 (cit. on p. 59).

[123] M. van Deventer and A. Boot. "Polarization properties of stimulated Brillouin scattering in single-mode fibers". *Journal of Lightwave Technology* 12 (4) (1994), pp. 585–590 (cit. on p. 59).

[124] L. B. Jeunhomme. *Single-mode fiber optics: principles and applications*. Optical engineering v. 4. New York: M. Dekker, 1983 (cit. on p. 60).

[125] S. L. McCall. "Instability and regenerative pulsation phenomena in Fabry-Perot nonlinear optic media devices". *Applied Physics Letters* 32 (5) (1978), pp. 284–286 (cit. on p. 65).

[126] F. Leo, L. Gelens, P. Emplit, M. Haelterman, and S. Coen. "Dynamics of one-dimensional Kerr cavity solitons". *Optics Express* 21 (7) (2013), pp. 9180–9191 (cit. on p. 65).

[127] K. Goda, D. R. Solli, K. K. Tsia, and B. Jalali. "Theory of amplified dispersive Fourier transformation". *Physical Review A* 80 (4) (2009), p. 043821 (cit. on pp. 66, 90).

[128] D. R. Solli, G. Herink, B. Jalali, and C. Ropers. "Fluctuations and correlations in modulation instability". *Nature Photonics* 6 (7) (2012), pp. 463–468 (cit. on pp. 66, 119, 129).

[129] B. Wetzel, A. Stefani, L. Larger, P. A. Lacourt, J. M. Merolla, T. Sylvestre, A. Kudlinski, A. Mussot, G. Genty, F. Dias, and J. M. Dudley. "Real-time full bandwidth measurement of spectral noise in supercontinuum generation". *Scientific Reports* 2 (2012) (cit. on pp. 66, 119).

[130] D. R. Solli, J. Chou, and B. Jalali. "Amplified wavelength–time transformation for real-time spectroscopy". *Nature Photonics* 2 (1) (2008), pp. 48–51 (cit. on p. 66).

[131] M. J. Schmidberger, P. Hosseini, D. Novoa, A. Stefani, P. S. Russell, and N. Joly. "Spectrally resolved shot-to-shot nonlinear dynamics of a passive PCF ring cavity". Munich: OSA, 2014, SW1I.2 (cit. on p. 66).

[132] A. F. J. Runge, N. G. R. Broderick, and M. Erkintalo. "Observation of soliton explosions in a passively mode-locked fiber laser". *Optica* 2 (1) (2015), p. 36 (cit. on p. 66).

[133] A. F. J. Runge, N. G. R. Broderick, and M. Erkintalo. "Dynamics of soliton explosions in passively mode-locked fiber lasers". *Journal of the Optical Society of America B* 33 (1) (2016), p. 46 (cit. on p. 66).

[134] J. Hammer, P. Hosseini, C. R. Menyuk, P. St.J. Russell, and N. Y. Joly. "Single-shot reconstruction of spectral amplitude and phase in a fiber ring cavity at a 80 MHz repetition rate". *Optics Letters* 41 (20) (2016), p. 4641 (cit. on p. 66).

[135] G. Herink, B. Jalali, C. Ropers, and D. R. Solli. "Resolving the build-up of femtosecond mode-locking with single-shot spectroscopy at 90 MHz frame rate". *Nature Photonics* (2016) (cit. on p. 66).

[136] Y. Tong, L. Chan, and H. Tsang. "Fibre dispersion or pulse spectrum measurement using a sampling oscilloscope". *Electronics Letters* 33 (11) (1997), p. 983 (cit. on p. 66).

[137] K. Goda and B. Jalali. "Dispersive Fourier transformation for fast continuous single-shot measurements". *Nature Photonics* 7 (2) (2013), pp. 102–112 (cit. on p. 66).

[138] F. Leo, P. Kockaert, P. Emplit, M. Haelterman, A. Mussot, E. Louvergneaux, and M. Taki. "Experimental Generation of 1.6-THz Repetition-Rate Pulse-Trains in a Passive Optical Fiber Resonator". *Conference on Lasers and Electro-Optics/International Quantum Electronics Conference (2009), paper JTuD111*. Optical Society of America, 2009, JTuD111 (cit. on p. 68).

[139] B. H. Kolner and M. Nazarathy. "Temporal imaging with a time lens". *Optics Letters* 14 (12) (1989), p. 630 (cit. on p. 68).

[140] B. Kolner. "Space-time duality and the theory of temporal imaging". *IEEE Journal of Quantum Electronics* 30 (8) (1994), pp. 1951–1963 (cit. on p. 68).

[141] R. Salem, M. A. Foster, A. C. Turner, D. F. Geraghty, M. Lipson, and A. L. Gaeta. "Optical time lens based on four-wave mixing on a silicon chip". *Optics Letters* 33 (10) (2008), pp. 1047–1049 (cit. on p. 68).

[142] M. Närhi, B. Wetzel, C. Billet, S. Toenger, T. Sylvestre, J.-M. Merolla, R. Morandotti, F. Dias, G. Genty, and J. M. Dudley. "Real-time measurements of spontaneous breathers and rogue wave events in optical fibre modulation instability". *Nature Communications* 7 (2016), ncomms13675 (cit. on p. 68).

[143] P. Suret, R. E. Koussaifi, A. Tikan, C. Evain, S. Randoux, C. Szwaj, and S. Bielawski. "Single-shot observation of optical rogue waves in integrable turbulence using time microscopy". *Nature Communications* 7 (2016), ncomms13136 (cit. on p. 68).

[144] R. Salem, M. A. Foster, and A. L. Gaeta. "Application of space–time duality to ultrahigh-speed optical signal processing". *Advances in Optics and Photonics* 5 (3) (2013), p. 274 (cit. on p. 68).

[145] F. Leo, A. Mussot, P. Kockaert, P. Emplit, M. Haelterman, and M. Taki. "Nonlinear Symmetry Breaking Induced by Third-Order Dispersion in Optical Fiber Cavities". *Physical Review Letters* 110 (10) (2013), p. 104103 (cit. on pp. 84, 108, 133).

[146] L. Yang, M. Dolnik, A. M. Zhabotinsky, and I. R. Epstein. "Spatial Resonances and Superposition Patterns in a Reaction-Diffusion Model with Interacting Turing Modes". *Physical Review Letters* 88 (20) (2002), p. 208303 (cit. on p. 88).

[147] N. N. Rozanov, V. E. Semenov, and G. V. Khodova. "Transverse structure of a field in nonlinear bistable interferometers. I. Switching waves and steady-state profiles". *Soviet Journal of Quantum Electronics* 12 (2) (1982), pp. 193–197 (cit. on p. 93).

[148] S. B. Cavalcanti, J. C. Cressoni, H. R. da Cruz, and A. S. Gouveia-Neto. "Modulation instability in the region of minimum group-velocity dispersion of single-mode optical fibers via an extended nonlinear Schrödinger equation". *Physical Review A* 43 (11) (1991), pp. 6162–6165 (cit. on p. 108).

[149] J. D. Harvey, R. Leonhardt, S. Coen, G. K. L. Wong, J. C. Knight, W. J. Wadsworth, and P. St.J. Russell. "Scalar modulation instability in the normal dispersion regime by use of a photonic crystal fiber". *Optics Letters* 28 (22) (2003), pp. 2225–2227 (cit. on p. 108).

[150] S. Pitois and G. Millot. "Experimental observation of a new modulational instability spectral window induced by fourth-order dispersion in a normally dispersive single-mode optical fiber". *Optics Communications* 226 (2003), pp. 415–422 (cit. on p. 108).

[151] A. Mussot, E. Louvergneaux, N. Akhmediev, F. Reynaud, L. Delage, and M. Taki. "Optical Fiber Systems Are Convectively Unstable". *Physical Review Letters* 101 (11) (2008), p. 113904 (cit. on pp. 108, 129, 133).

[152] Y. Xu and S. Coen. "Experimental observation of the spontaneous breaking of the time-reversal symmetry in a synchronously pumped passive Kerr resonator". *Optics Letters* 39 (12) (2014), p. 3492 (cit. on p. 108).

[153] P. Parra-Rivas, D. Gomila, F. Leo, S. Coen, and L. Gelens. "Third-order chromatic dispersion stabilizes Kerr frequency combs". *Optics Letters* 39 (10) (2014), p. 2971 (cit. on p. 108).

[154] M. Tlidi, A. Mussot, E. Louvergneaux, G. Kozyreff, A. G. Vladimirov, and M. Taki. "Control and removal of modulational instabilities in low-dispersion photonic crystal fiber cavities". *Optics Letters* 32 (6) (2007), pp. 662–664 (cit. on p. 108).

[155] F. Bessin, F. Copie, M. Conforti, A. Kudlinski, and A. Mussot. "Modulation instability in the weak normal dispersion region of passive fiber ring cavities". *Optics Letters* 42 (19) (2017), pp. 3730–3733 (cit. on pp. 108, 112, 129).

[156] M. J. Potasek. "Modulation instability in an extended nonlinear Schrödinger equation". *Optics Letters* 12 (11) (1987), p. 921 (cit. on p. 112).

[157] F. Vanholsbeeck, S. Martin-Lopez, M. González-Herráez, and S. Coen. "The role of pump incoherence in continuous-wave supercontinuum generation". *Optics Express* 13 (17) (2005), p. 6615 (cit. on p. 119).

[158] K. Luo, J. K. Jang, S. Coen, S. G. Murdoch, and M. Erkintalo. "Spontaneous creation and annihilation of temporal cavity solitons in a coherently driven passive fiber resonator". *Optics Letters* 40 (16) (2015), p. 3735 (cit. on p. 129).

[159] J. K. Jang, M. Erkintalo, S. G. Murdoch, and S. Coen. "Writing and erasing of temporal cavity solitons by direct phase modulation of the cavity driving field". *Optics Letters* 40 (20) (2015), p. 4755 (cit. on p. 129).

[160] C. Bao and C. Yang. "Stretched cavity soliton in dispersion-managed Kerr resonators". *Physical Review A* 92 (2) (2015), p. 023802 (cit. on p. 129).

[161] J. K. Jang, M. Erkintalo, S. G. Murdoch, and S. Coen. "Observation of dispersive wave emission by temporal cavity solitons". *Optics Letters* 39 (19) (2014), pp. 5503–5506 (cit. on p. 129).

[162] K. Luo, Y. Xu, M. Erkintalo, and S. G. Murdoch. "Resonant radiation in synchronously pumped passive Kerr cavities". *Optics Letters* 40 (3) (2015), pp. 427–430 (cit. on p. 129).

[163] S.-W. Huang, A. K. Vinod, J. Yang, M. Yu, D.-L. Kwong, and C. W. Wong. "Quasi-phase-matched multispectral Kerr frequency comb". *Optics Letters* 42 (11) (2017), pp. 2110–2113 (cit. on p. 129).

[164] S. Malaguti, G. Bellanca, and S. Trillo. "Dispersive wave-breaking in coherently driven passive cavities". *Optics Letters* 39 (8) (2014), p. 2475 (cit. on p. 129).

[165] B. Garbin, Y. Wang, S. G. Murdoch, G.-L. Oppo, S. Coen, and M. Erkintalo. "Experimental and numerical investigations of switching wave dynamics in a normally dispersive fibre ring resonator". *The European Physical Journal D* 71 (9) (Sept. 2017), p. 240 (cit. on p. 129).

[166] A. Mussot, P. Szriftgiser, C. Naveau, M. Conforti, A. Kudlinski, F. Copie, and S. Trillo. "Observation of broken symmetry in the modulation instability recurrence". *2017 European Conference on Lasers and Electro-Optics and European Quantum Electronics Conference (2017), paper PD_2_6*. Munich, Germany: Optical Society of America, 2017, PD_2_6 (cit. on p. 129).

[167] A. Mussot, C. Naveau, M. Conforti, A. Kudlinski, F. Copie, P. Szriftgiser, and S. Trillo. "Fibre multiwave-mixing combs reveal the broken symmetry of Fermi-Pasta-Ulam recurrence". *Submitted to Nature Photonics* () (cit. on p. 129).

[168] P. Parra-Rivas, D. Gomila, M. A. Matías, P. Colet, and L. Gelens. "Effects of inhomogeneities and drift on the dynamics of temporal solitons in fiber cavities and microresonators". *Optics Express* 22 (25) (2014), pp. 30943–30954 (cit. on p. 133).

Author's bibliography

Publications in peer-reviewed journals

• **F. Copie**, A. Kudlinski, M. Conforti, G. Martinelli, and A. Mussot. "Modulation instability in amplitude modulated dispersion oscillating fibers". *Optics Express* 23 (4) (2014), pp. 3869 - 3875

• **F. Copie**, M. Conforti, A. Kudlinski, S. Trillo, and A. Mussot. "Competing Turing and Faraday instabilities in longitudinally modulated passive resonators". *Physical Review Letters* 116 (14) (2016), p. 143901

• G. Xu, A. Mussot, A. Kudlinski, S. Trillo, **F. Copie**, and M. Conforti. "Shock wave generation triggered by a weak background in optical fibers". *Optics Letters* 41 (11) (2016), pp. 2656 - 2659

• M. Conforti, **F. Copie**, A. Mussot, A. Kudlinski, and S. Trillo. "Parametric instabilities in modulated fiber ring cavities". *Optics Letters* 41 (21) (2016), pp. 5027 - 5030

• **F. Copie**, M. Conforti, A. Kudlinski, S. Trillo, and A. Mussot. "Dynamics of Turing and Faraday instabilities in a longitudinally modulated fiber-ring cavity". *Optics Letters* 42 (3) (2017), pp. 435 - 438

• **F. Copie**, M. Conforti, A. Kudlinski, S. Trillo, and A. Mussot. "Modulation instability in the weak dispersion regime of a dispersion modulated passive fiber-ring cavity". *Optics Express* 25 (10) (2017), pp. 11283 - 11296

• F. Bessin, **F. Copie**, M. Conforti, A. Kudlinski, and A. Mussot. "Modulation instability in the weak normal dispersion region of passive fiber ring cavities". *Optics Letters* 42 (19) (2017), pp. 3730 - 3733

• A. Mussot, C. Naveau, M. Conforti, A. Kudlinski, **F. Copie**, P. Szriftgiser, and S. Trillo. "Observation of broken symmetry in the modulation instability recurrence". Submitted to *Nature Photonics*

Review articles in peer-reviewed journals

• **F. Copie**, M. Conforti, A. Kudlinski, A. Mussot, F. Biancalana, and S. Trillo. "Instabilities in passive dispersion oscillating fiber ring cavities". *The European Physical Journal D* 71 (5) (2017), p. 133

• A. Mussot, M. Conforti, S. Trillo, **F. Copie**, and A. Kudlinski. "Modulation instability in dispersion oscillating fibers". *Advances in Optics and Photonics* 10 (1) (2018), pp. 1 - 42.

Orals in peer-reviewed national conferences

• A. Mussot, **F. Copie**, M. Conforti, G. Martinelli, and A. Kudlinski. "Instabilité modulationnelle dans une fibre optique présentant un profil de dispersion oscillant complexe". *Journées Nationales de l'Optique Guidée*, Nice, France (2014)

• F. Bessin, **F. Copie**, M. Conforti, A. Kudlinski, and A. Mussot. "Instabilité de modulation dans une cavité fibrée monostable en régime de dispersion normale". *Journées Nationales de l'Optique Guidée*, Limoges, France (2017)

Orals in peer-reviewed international conferences

• **F. Copie**, M. Conforti, A. Kudlinski, S. Trillo, and A. Mussot. "Experimental demonstration of modulation instability in dispersion oscillating fiber ring cavity". *European Quantum Electronics Conference*, Munich, Germany (2015)

• **F. Copie**, M. Conforti, A. Kudlinski, S. Trillo, and A. Mussot. "Experimental Demonstration of New Modulational Instability Bands in a Dispersion Oscillating Fiber Cavity". *Asia Communications and Photonics Conference*, Hong Kong (2015)

• G. Xu, A. Mussot, A. Kudlinski, S. Trillo, **F. Copie**, and M. Conforti. "Observation of the breaking of a pulse on a weak background in optical fibers". *Conference on Lasers and Electro-Optics*, San Jose, USA (2016)

• **F. Copie**, M. Conforti, A. Kudlinski, S. Trillo, and A. Mussot. "Observation of Turing and Faraday instabilities in a bistable passive resonator". *Conference on Lasers and Electro-Optics*, San Jose, USA (2016)

• **F. Copie**, M. Conforti, A. Kudlinski, S. Trillo, and A. Mussot. "Roundtrip-to-roundtrip evolution of Faraday and Turing instabilities in dispersion oscillating fiber ring resonators". *Photonics and Fiber Technology: Nonlinear Photonics*, Sydney, Australia (2016)

• S. Trillo, M. Conforti, **F. Copie**, A. Kudlinski and A. Mussot. "Parametric resonances in modulated passive fiber cavities". *Nice Optics*, Nice, France (2016)

• A. Mussot, P. Szriftgiser, C. Naveau, M. Conforti, A. Kudlinski, **F. Copie**, and S. Trillo. "Observation of broken symmetry in the modulation instability recurrence". Post-deadline paper at *Conference on Lasers and Electro-Optics - Europe*, Munich, Germany (2017)

• F. Bessin, **F. Copie**, M. Conforti, A. Kudlinski, and A. Mussot. "Modulational instabilities in the weak normal dispersion region of uniform fiber ring cavities". *Conference on Lasers and Electro-Optics - Europe*, Munich, Germany (2017)

Invited orals in peer-reviewed international conferences

• A. Mussot, A. Kudlinski, M. Conforti, A. Bendahmane, F. Braud, **F. Copie**, S. Wang and S. Trillo. "Topographic Optical Fibers : New Perspectives in Nonlinear Guided Optics". *Frontiers in Optics*, San Jose, USA (2015)

• A. Mussot, A. Kudlinski, M. Conforti, A. Bendahmane, F. Braud, **F. Copie**, S. Wang and S. Trillo. "New prospects in nonlinear optics with topographic optical fibers". *Conference on Lasers and Electro-Optics*, San Jose, USA (2016)

Posters in peer-reviewed international conferences

• **F. Copie**, M. Conforti, A. Kudlinski, S. Trillo, and A. Mussot. "Modulation instability in the weak dispersion regime of dispersion oscillating fiber-ring cavities". *European Quantum Electronics Conference*, Munich, Germany (2017)

• **F. Copie**, M. Conforti, A. Kudlinski, S. Trillo, and A. Mussot. "Modulation instability in the weak dispersion regime of dispersion oscillating fiber-ring cavities". *Frontiers in Optics*, Washington DC, USA (2017)

Modulation instabilities in dispersion oscillating passive fiber-ring cavities

Abstract

This thesis work deals with the parametric instability occurring in passive optical fiber-ring cavities, which is induced by a longitudinal modulation of the chromatic dispersion. In optical cavities, the modulation instability process is known to potentially destabilize the stationary state and turn it into a stable train of pulses. We describe in this work how a longitudinal variation of the dispersion inside the cavity enriches the dynamics of this type of device by entailing a regime of parametric instability. We detail the theoretical study of this new mechanism, which allows us to identify its spectral and temporal signatures, among which, the generation of multiple resonance peaks in the optical spectrum and the appearance of a period doubling dynamics in the time domain. We have realized such resonators in order to confirm experimentally our predictions. The model we have chosen simply consists in building a ring by splicing together uniform fibers characterized by different dispersions. In terms of results, we first observed the emergence of both modulational and parametric instabilities in the same system, before investigating their dynamics. The latter is accessible thanks to real-time spectral and temporal detection methods. We thus observed with remarkable precision the emergence of the instabilities, the period doubling associated to the parametric regime and the appearance of a record number of parametric resonances in our system.

Keywords: nonlinear optics; optical fibers; passive fiber cavities; modulation instability; parametric instability

---

Instabilités modulationnelles dans les cavités fibrées passives à dispersion oscillante

Résumé

Ces travaux de thèse portent sur l'instabilité paramétrique survenant dans les cavités optiques fibrées passives en anneau, induite par une modulation longitudinale de la dispersion chromatique. Dans les cavités optiques, le processus d'instabilité modulationnelle est connu pour être susceptible de déstabiliser l'état stationnaire et de le transformer en un train stable d'impulsions. Nous décrivons dans ce travail comment une variation longitudinale de la dispersion à l'intérieur de la cavité enrichit la dynamique de ce type de dispositif en engendrant un régime d'instabilité paramétrique. Nous détaillons l'étude théorique de ce nouveau mécanisme ce qui nous permet d'en identifier les signatures spectrales et temporelles, parmi lesquelles, la génération de multiples pics de résonances dans le spectre optique et l'apparition d'une dynamique de doublement de période dans le domaine temporel. Nous avons réalisé de tels résonateurs afin de confirmer expérimentalement nos prédictions. Le modèle que nous avons retenu consiste à réaliser un anneau en soudant entre elles des fibres uniformes présentant des dispersions différentes. En terme de résultats, nous avons tout d'abord observé pour la première fois l'apparition des instabilités modulationnelle et paramétrique dans un même système, pour ensuite s'intéresser à leur dynamique. Cette dernière est accessible grâce à des méthodes de détection en temps réel à la fois spectrale et temporelle. Nous avons ainsi pu observer avec une précision remarquable l'émergence des instabilités, le doublement de période associé au régime paramétrique ainsi que l'apparition d'un nombre record de résonances paramétriques dans notre système.

Mots clés : optique non-linéaire ; fibres optiques ; cavités fibrées passives ; instabilité modulationnelle ; instabilité paramétrique

---

Laboratoire de Physique des Lasers, Atomes et Molécules (PhLAM)
Bât. P5 – 59655 Villeneuve d'Ascq Cedex – France